ABSTRACT

Title of Dissertation: THE SHADOWS OF WOULD-BE GODS: FINDING TRANSITING JOVIANS, TERRESTRIALS, AND EVERYTHING IN BETWEEN WITH TESS TO UNDERSTAND HOT JUPITER FORMATION AND THE BEST TARGETS FOR JWST

Benjamin Hord
Doctor of Philosophy, 2023

Dissertation Directed by: Professor Eliza Kempton
Department of Astronomy
Dr. Knicole Colón
NASA's Goddard Space Flight Center

NASA's Transiting Exoplanet Survey Satellite (TESS) mission launched in 2018 and has since observed more than 90% of the sky and discovered more than 6,000 planet candidates of many sizes, temperatures, and orbital periods. Hot Jupiters, in particular, have benefited from TESS since these planets are uniformly distributed throughout the sky and produce large transit signals. Many questions remain about this enigmatic class of large gas giants orbiting extremely close to their host stars regarding their formation and evolution. My dissertation leverages TESS to investigate the potential formation mechanisms of hot Jupiters and applies relevant planet discovery techniques to a collection of planet candidates that would be most amenable, or "best-in-class," for atmospheric characterization with JWST.

First, I performed a uniform search for nearby companion planets to hot Jupiters observed by TESS in its first year of operations. The lack of planets nearby hot Jupiters in their planetary

systems has long been thought to be a fingerprint of their dynamically active formation history, although a recent set of discoveries of nearby planets in three hot Jupiter systems has challenged this notion. I developed a custom-built search, vetting, and validation pipeline to detect additional transit signals in TESS light curves of hot Jupiter systems and evaluate the planetary nature of each. This study found a host of new transit-like signals but none were deemed to be caused by planets, reinforcing the idea that companion planets to hot Jupiters are rare. I also estimated the expected rate at which hot Jupiters should have companions and found it to be $7.3^{+15.2}_{-7.3}\%$.

Second, I continued the search for additional planets in hot Jupiter systems as TESS continued to observe the sky and discovered a new signal in the WASP-132 system. I vetted and statistically validated this signal to demonstrate that it is indeed from a new planet, dubbed WASP-132 c. This planet orbits interior to the hot Jupiter WASP-132 b and constitutes only the fourth such system discovered at the time. I performed some initial analysis on the limited sample of hot Jupiters with nearby companions and found evidence suggesting that systems with this architecture predominantly have an outer hot Jupiter beyond the $\sim$3 day orbital period pileup with an inner companion. This may be due to a number of factors, including physical and observational, such as formation mechanism or the bias towards short period planets of transit surveys.

Finally, I leveraged the planet discovery, vetting, and validation techniques I had applied to the search for companions to hot Jupiters to perform a large-scale validation of over 100 planet candidates discovered by TESS that were deemed “best-in-class” for atmospheric characterization with JWST. This included the synthesis and ranking of all planets and planet candidates by observability with JWST into a single sample and then performing vetting and validation analyses on those that were candidates. In total, I statistically validated 22 planet candidates and marginally validated a further 35. I present the final best-in-class sample as a community resource for future JWST observations.

The Shadows of Would-Be Gods: Finding Transiting Jovians, Terrestrials, and Everything In Between with TESS to Understand Hot Jupiter Formation and the Best JWST Targets

by

Benjamin Hord

Dissertation submitted to the Faculty of the Graduate School of the
University of Maryland, College Park in partial fulfillment
of the requirements for the degree of
Doctor of Philosophy
2023

Advisory Committee:
Professor Eliza Kempton, Chair/Advisor
Dr. Knicole Colón, Co-Advisor
Professor Tad Komacek
Professor Derek Richardson
Dr. Alan Boss
Professor Christine Hartzell

Preface

The research presented in Chapters 2 and 3 of this dissertation has been previously published. Chapter 4 of this dissertation is under review by the TESS collaboration and will be submitted shortly for publication.

Chapter 2 is presented with only minimal modifications since appearing in the Astronomical Journal (AJ) as "A Uniform Search for Nearby Planetary Companions to Hot Jupiters in TESS Data Reveals Hot Jupiters are Still Lonely" (Hord et al., 2021). I conducted the bulk of the analysis presented in this work. I assembled the target list and data set, developed the search pipeline, searched each light curve, vetted and validated each candidate signal, modeled the photometric time series data, and performed the occurrence rate analysis. Coauthors contributed feedback on the analysis methods and text.

Chapter 3 is presented with only minimal modifications since appearing in AJ as "The Discovery of a Planetary Companion Interior to Hot Jupiter WASP-132 b" (Hord et al., 2022). I conducted the bulk of the analysis presented in this work. I performed an independent search to recover the candidate signal, performed most of the vetting analysis, modeled the photometry, performed the statistical validation analysis, dynamically modeled the system, modeled and searched for signals in the radial velocity data, put the system in context with other systems of similar architecture, and drew the formation and population-level conclusions presented. Coauthors assisted with running DAVE– an automated vetting software – obtaining follow-up observations, performing stellar modeling, and contributing feedback on the analysis methods and text.

Chapter 4 is presented in its current pre-review form. Few, if any, major changes are expected from the review by the TESS collaboration. Therefore, I plan that a version very similar to that presented here will be submitted to the AAS journals in the coming weeks. I conducted the bulk of the analysis presented in this work. I assembled the target list and the data set, performed the vetting and validation analysis (including modifying requisite codes), made determinations as to the category each target belonged to, and organized all of the data and results for presentation. Coauthors contributed follow-up observations, and some feedback on final target disposition and text.

Foreword

No sooner had *Homo sapiens* diverged from their evolutionary ancestors than had humankind turned its eyes skyward, tracking the bodies that moved slowly and periodically across the heavens and ascribing to them divinity. Today, we know these objects as planets, not gods, although to our ancestors, these would be one and the same. We can now describe the motion of these bodies precisely using equations and see them with telescopes. We have visited them and investigated them. But this makes them no less fantastic, only better understood.

The forces and phenomena that were the stuff of myth and legend have not changed, but the way in which we describe them has. We continue to seek a greater knowledge of that which holds great power and, in this way, we are no different from those who preceded us. In our study of the Universe, we build upon the intellectual heritage of our ancestors, investigating the cosmos out of reverence for its ability to dwarf even the greatest of human feats. Nowhere is this better evidenced than with the planets, whose very names remain the names of deities who have long since lost their divine status and whose power and scale have captivated our imaginations as objects to be harnessed, explored, and understood.

While our contemporary definitions of divinity have shifted to no longer encompass that which we believe to be known, the discovery and investigation of the universe and its components remains no less all-consuming now than it was to our distant ancestors. Divinity lies not in wrathful deities or faceless clockmakers, but in the unknown, and by demystifying one part of the Universe, we push the definition of divinity to another part just beyond reach.

It is in this context that this work is performed; a demystification of would-be gods revolving around suns all their own as part of a persistent, all-too-human need to explore and understand, to assign meaning where there is yet none. The making of what was once divine into something known and mundane, something that can be comprehended through a means other than myth and legend; a morphing of awe from one of spirituality to one of sheer scale and magnitude.

Dedication

To those who didn’t think I could get this far, and to everyone who knew otherwise.

To everyone who was willing to take a chance on me.

Acknowledgments

As an Astronomer, I would think it trite to thank the Universe, but this is precisely what I intend to do here. What follows this section is almost two hundred pages summarizing my exploration of the Universe conducted over the course of five years. But this section is more important. This is where I get to thank *my* Universe, an arguably more real, more important, facet of my life spanning far beyond the past five years.

From the beginning, my Universe started with the very best family I could ask for. I have my Mom, Dad, Blake, and Will to thank for who I am, for shaping me through patience, love, and the occasional brotherly quarrel into the person I'm proud to be. You all instilled in me the self-confidence to know that I can accomplish anything and the humility to know when I've given it my best shot; the independence to forge my own path and the sentimentality to find my way home; kindness in the treatment of others and resolution in the defense of what I believe in.

Within this same orbit are my grandparents, Memaw, Bop, Grandaddy, and Memawmaw, whose only reaction to my high school report card Sophomore year was, ”Wow, only three absences.” I think she would be proud with my level of attendance these past few years. They've all given me people to look up to and qualities to emulate, whether it be the value of hard work or the value of wonder. And included in this group are my aunts, uncles, and cousins who were and continue to be the most fun.

Thank you, Universe.

I'm very fortunate to have had such great friends from growing up back home in Dobbs Ferry. I cannot understate the impact Gabe, Max, Will, Michael, Paul, Zakiya, Jill, Joli, Ian, Haley, Taylor, Sean, Ryan, and countless others have had on who I was, who I am, and who I will be. The friendships I have with those from back home are incredibly special, and the longer they last, the more I realize how rare they are. You only get to grow up once, and I'm honored that it was with you all. To the DI team, you allowed me to express a creative part of myself that I didn't often get a chance to express, and it turns out we were all looking to do the same.

Astronomy was not my first choice of career, and it most likely wasn't my second, but the people and friends that I made in my time at Columbia through Blueshift, Astronomy courses, and research experiences cemented my decision to pursue this as a career. People like Andy, Yasmeen, Doug, Jessica, Gabby, Marisa, Brian, Anna, Nick, and many others made the tough times easier, the easy times enjoyable, and the whole time special. Whether it was taping Starbites, building a radio telescope that almost blew off the roof of a 15 story building, or driving to the middle of nowhere Pennsylvania for stargazing, I can always count on you all as some of the kindest, most fun, and welcoming people I have ever known.

Simultaneously, everyone I met through clubs, outings, or from living on the same floor made those four years all the more precious. From Camilo, Gloriana, Adam, Liz, Ross, Mark, Liz, Julia, Ron, and Taimur whom I met in the band to Barrington, Sarah, Charlotte, Amy, Christian, Evan, Miguel, Anisha, Rex, and Josue whom I met in John Jay and plenty of others, you saw me through one of the most transformational times of my life and it was through your support and willingness to have fun or go on an adventure that I came out to be even half of who I am today.

Though I may not have known them as long, I count the individuals I met at UMD among my closest friends and I know that the bonds that have been forged in my time here will far outlast my time at this institution. Teal and Erica (and David!) have been the absolute best officemates, gaming pals, C.O.O.K.S., and all-around friends that I could've asked for in the program. This is not to mention the fantastic cohort that we had, the Hyattsville house, the D&D crew, and the whole Astronomy grad population in general, especially Joe, Ramsey, Milena, Julian, and Vicente.

Thank you, Universe.

I would be remiss if I did not mention the slice of my Universe occupied by all of the individuals and educators that have shepherded and mentored me throughout my academic career. Teachers like Mrs. Borenstein, Mrs. Palladino, Mr. Cottingham, Mr. Fischbeck, Mr. Falconetti, and Mr. Meagh went above and beyond to encourage me to excel and seek out my interests. Dr. Tom Callahan in sophomore year of high school really kickstarted my path that has ultimately led to the research position I hold today. It was through him that I found my first real research opportunity at the American Museum of Natural History in New York studying quasars with Dr. Matt O'Dowd, to whom I'm incredibly grateful. I'm also eternally thankful to Professor Chuck Hailey and Dr. Kaya Mori at Columbia for taking a chance on me and giving me one of the most educational, rigorous research experiences I think I'll ever have. Given that the first thing Chuck asked me was "What's your defect?" I hope I surpassed his expectations. I'm also exceptionally appreciative to my current advisors, Dr. Knicole Colón and Professor Eliza Kempton. I knew nothing about exoplanets when I first reached out to Knicole asking to work with her on an interesting hot Jupiter project, and I cannot adequately express my gratitude to her that she took a chance on me.

Thank you, Universe.

And to Caitlyn and Touhy, who have been there right by my side throughout all of the stresses, excitement, and changes of plan that it takes to pull together a PhD, your support and enthusiasm means the world (dare I say, multiple worlds) to me. I love you both more than I can find the words to describe.

So once again, thank you, Universe.

Just as stars and galaxies have no more claim to comprising the Universe than that of dust and atoms, so, too, do all those with whom my interactions have been brief or fleeting have a claim to their own part of my Universe and how it has shaped me. So thank you to all those who have not been named, who I have no memory of, and those who I may never speak to again for your existence in my Universe. As the Universe shapes us, so too has my Universe shaped me, and for that, I will be forever grateful.

Table of Contents

List of Tables

List of Figures

List of Abbreviations

2MASS	Two Micron All-Sky Survey
AU	Astronomical Unit
BEB	Blended Eclipsing Binary
BLS	Box Least Squares
CCD	Charge Coupled Device
CDPP	Combined Differential Photometric Precision
DACE	Data and Analysis Center for Exoplanets
DAVE	Discovery and Vetting of Exoplanets
DR2	Data Release 2
DR3	Data Release 3
DV	Data Validation
EB	Eclipsing Binary
EDR3	Early Data Release 3
ExoFOP	Exoplanet Follow-up Observation Program
FAP	False Alarm Probability
FFI	Full Frame Image
FPP	False Positive Probability
HEB	Hierarchical Eclipsing Binary
HEM	High-Eccentricity Migration
HJ	Hot Jupiter
JWST	James Webb Space Telescope
LCOGT	Las Cumbres Observatory Global Telescope
MAST	Mikulski Archive for Space Telescopes
MCMC	Markov Chain Monte Carlo
NASA	National Aeronautics and Space Administration
NEB	Nearby Eclipsing Binary
NFPP	Nearby False Positive Probability
NUTS	No U-Turn Sampler
PCA	Principal Component Analysis
PDC	Pre-search Data Conditioning
PDC_SAP	Pre-search Data Conditioning Simple Aperture Photometry
PSF	Point Spread Function
QLP	Quick-Look Pipeline
SAP	Simple Aperture Photometry
SDE	Signal Detection Efficiency
SED	Spectral Energy Distribution

SOAR	Southern Astrophysical Research Telescope
SOPC	Science Processing Operations Center
TESS	Transiting Exoplanet Survey Satellite
TFOP	TESS Follow-up Observation Program
TIC	TESS Input Catalog
TLS	Transit Least Squares
TOI	TESS Object of Interest
TPF	Target Pixel File
TRAPPIST	Transiting Planets and Planetesimals Small Telescope
TRICERATOPS	Tool for Rating Interesting Candidate Exoplanets and Reliability Analysis of Transits Originating from Proximate Stars
TTV	Transit Timing Variation
UT	Universal Time
VESPA	Validation of Exoplanet Signals using a Probabilistic Algorithm
WASP	Wide Angle Search for Planets
WISE	Wide-field Infrared Survey Explorer
WJ	Warm Jupiter

Chapter 1: Introduction

The idea of planets orbiting stars other than the Sun has garnered public fascination for decades, if not longer, with science fiction literature, television, and films glorifying the discovery and understanding of alien worlds both similar and dissimilar to ours. This captivation became reality with the discovery of the first planets around another star – or "exoplanets" – by Aleksander Wolszczan and Dale Frail in 1992 (Wolszczan & Frail, 1992a). Although these planets orbited around a pulsar – the remnants of a dead star emitting extreme levels of high-energy radiation – this discovery blew open the door for further discoveries and the field of exoplanet science itself. It was only a few years later that Michel Mayor and Didier Queloz would discover a giant gaseous planet zipping around its host star of 51 Pegasi on an orbit of only 4.23 days (Mayor & Queloz, 1995), eventually earning them the 2019 Nobel Prize in Physics for their discovery. This marked the first planet discovery around a main-sequence star similar in many ways to our own Sun.

Since then, over 5,000 exoplanets have been confirmed according to the NASA Exoplanet Archive[1] with a huge variety in planet size, mass, temperature, composition, orbital period, and more. New categories of planets in portions of parameter space previously thought impossible for planets to inhabit have been discovered, raising new questions about planetary formation and

[1] https://exoplanetarchive.ipac.caltech.edu/

evolution and challenging long-held theories developed based on our Solar System. Among these new categories are the hot Jupiters – large gaseous planets larger than 8 Earth radii orbiting their stars on exceptionally close orbits with periods of less than 10 days (See Figure 1.1 Winn et al., 2010). It was thought that such planets could not exist and certainly could not form so close to their host stars but we now see them in abundance around main-sequence stars. Indeed, even the aforementioned 51 Pegasi b falls into this category.

Central to the process of studying the formation, evolution, and composition of hot Jupiters and other classes of planets is the discovery of additional planets and the observation of each through multiple methods. By building the sample of planets through new discovery – or conversely determining which portions of parameter space do not contain planets – we can better understand the similarities between planets of each class while disentangling these properties from the nuances of individual systems. Additionally, it is imperative to observe each of these planets via as many methods as possible, since each observation method provides different information regarding the planet and can often be used to break degeneracies in inferring planetary and orbital properties. These not only include discovery methods such as radial velocity observations or transit detections, but follow-up such as transmission or emission spectroscopy to study a planet's atmosphere.

In this dissertation, I present three scientific studies I have led that employ planet discovery and validation tools towards the ultimate goals of understanding the formation of hot Jupiters and observing the planets most amenable to atmospheric characterization with our current capabilities. This first introductory chapter presents the scientific and historical background necessary for each of these studies and provides the context within which these studies were performed. Section 1.1 outlines the process of planet discovery, including the transit method that my work heavily uses. Section 1.2 discusses the vetting and validation as well as many of the methods, techniques, and facilities engaged in determining whether a signal is due to an exoplanet or a false positive. Section 1.3 provides an overview of hot Jupiter formation, evolution, and current knowledge regarding this unique class of planets. Section 1.4 outlines the study of exoplanet atmospheres including the motivations behind studying exoplanet atmospheres as well as the state of the field and methods for characterizing an exoplanet's atmosphere.

Chapter 2 of this dissertation presents a uniform search for nearby companion planets to hot Jupiters in order to constrain the formation pathways of hot gas giants as well as estimate the expected occurrence rate of transiting planets nearby hot Jupiters. In a similar vein, Chapter 3 presents the discovery of one such system, WASP-132, containing a hot Jupiter with a nearby transiting companion planet and discusses the formation implications for the growing population of systems with this architecture. Chapter 4 presents a synthesis of what we consider the "best-in-class" planets and planet candidates for atmospheric characterization with JWST, including a vetting and validation analysis of each unconfirmed planet candidate contained within the sample. This dissertation concludes with a summary and discussion of future work contained in Chapter 5.

1.1 Exoplanet Discovery

Perhaps the most obviously important part of studying exoplanets is actually detecting them. What is less obvious, however, are the variety of methods through which they are detected and discovered and the biases inherent within each.

When Wolszczan and Frail discovered the first exoplanets in 1992, they took advantage of the host pulsar's regular and precisely-timed radio pulses. They noted that, as they observed the central pulsar, the timing of the pulsar's pulses varied in a regular, sinusoidal pattern and deduced that this was being caused by the gravitational pull of the orbiting planets pulling the pulsar around the system's center of mass. This causes slight variations in the distance that the light from the pulsar must cross to reach observers on Earth in a regular, repeating pattern (Phillips & Thorsett, 1994; Kramer, 2018). This discovery method has come to be known as pulsar timing and has been used to discover seven exoplanets (via the NASA Exoplanet Archive). This method allows for the mass and periods of the planets to be measured, although not the radius or the inclination of the planetary orbits. This method can measure planetary masses with precision down to a small fraction of Earth's mass (Thorsett & Phillips, 1992; Niţu et al., 2022) but as pulsars are fairly rare and don't provide hospitable environments for planets, this is not a very common method of exoplanet discovery. Certain variable stars can be used in the place of pulsars in this discovery method, but these are also very rare.

Similar to pulsar timing in its main principles is the radial velocity method. This technique was used to discover 51 Pegasi b by Mayor and Queloz in 1995 and also relies upon the subtle gravitational pulls of the orbiting planets on the host star around the system's center of mass. However, unlike pulsar timing, the periodic variations in the motion of the host star are measured via Doppler shifted features in the star's spectrum (Wright, 2018; Hara & Ford, 2023). As the star moves away from the observer, the features are shifted to longer wavelengths compared to the rest frame, while the opposite is true when the star moves closer to the observer as a result of gravitational interaction with the planet. This method extends the general principles of pulsar timing to all stars and allows for masses and periods of the planets to be measured, albeit less precisely, and has been used to find 1044 planets thus far (via the NASA Exoplanet Archive).

Still, this method alone does not provide information on a planet's radius or inclination.

It wouldn't be until 1999 when the first transits of an exoplanet across the disk of the star HD 209458 would be observed (Charbonneau et al., 1999a; Henry et al., 1999). This opened up a new detection method wholly distinct at its core from pulsar timing and radial velocity in that it did not rely on the gravitational interactions between the star and its planets, but rather the planet interacting with the light from the host star. This method provides the period, radius, and orbital inclination of the planet, rather than the mass, and is easily scaled to large photometric searches whereas some other detection methods are much more targeted.

Further techniques such as direct imaging, gravitational microlensing, and astrometry have also been employed in the detection of extrasolar bodies in conjunction with transits. Each of these detection methods carries observational biases and probes different portions of parameter space. Figure 1.1 illustrates the different slices of parameter space that each detection method is able to investigate. Furthermore, one detection method alone cannot discern all of the properties of a planet and in order to truly understand a planet, it is necessary to observe the planet with more than one of these detection techniques. In this manner, these detection techniques are complementary with one another and each have advantages and disadvantages when searching for planets.

In this dissertation, each planet and planet candidate was observed using the transit method, which will be discussed in Section 1.1.1, although additional observations using some of the other techniques were employed in determining whether a planet candidate can be considered a true planet or not.

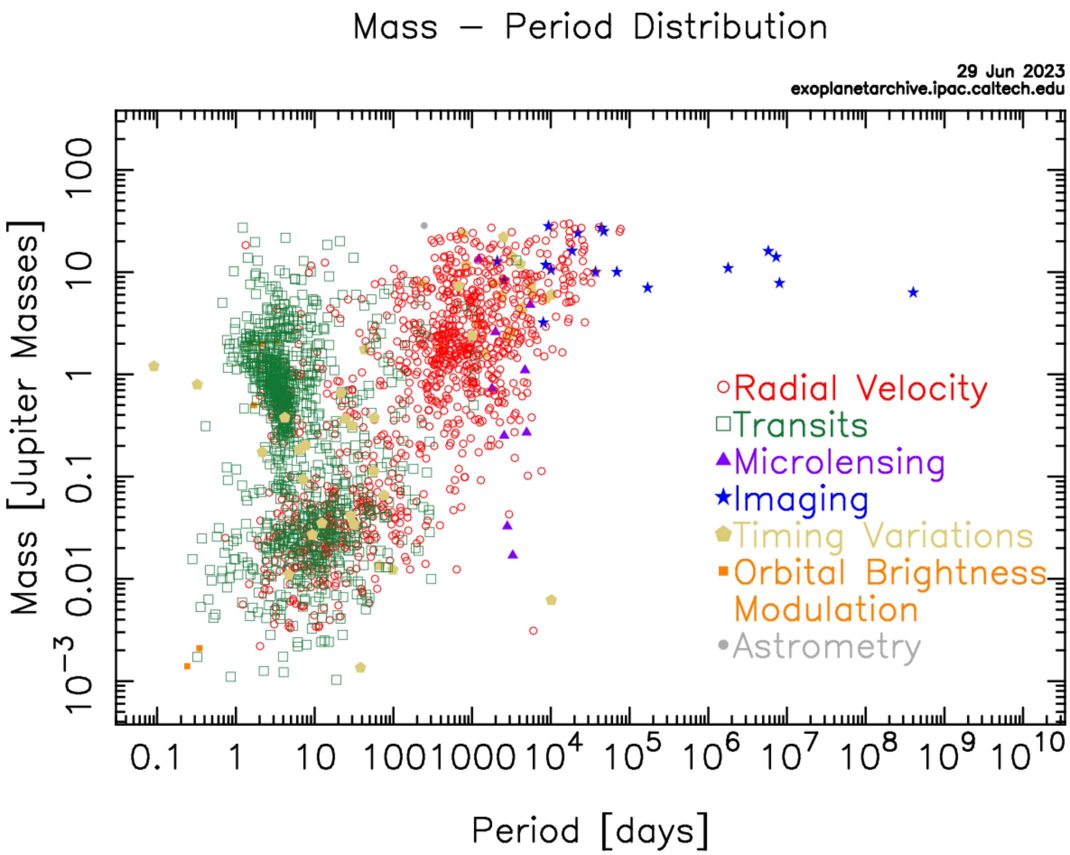

Figure 1.1: The mass-period distribution of all known exoplanets as of June 29, 2023 as generated on the NASA Exoplanet Archive. The color and marker of each planet on the plot denotes its discovery method. As you can see, different exoplanet detection techniques capture different parts of the mass-period parameter space with some overlap in the regions between groupings of planets. Some methods, such as timing variations, are spread throughout but are sparsely populated due to their observational difficulty. Figure from the NASA Exoplanet Archive: https://exoplanetarchive.ipac.caltech.edu/

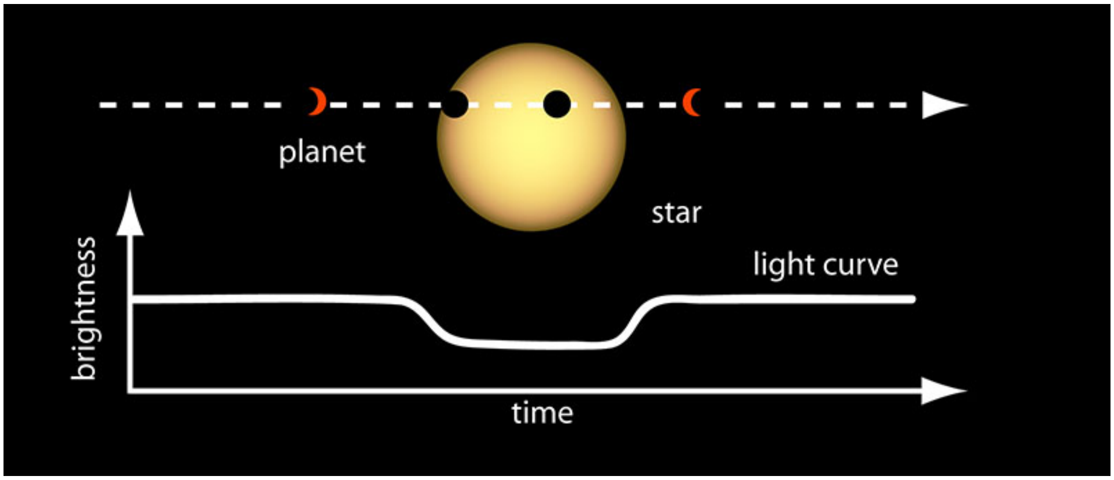

Figure 1.2: A schematic illustration of an exoplanet transiting across the disk of its host star. On the top of the image, a representation of a planet traveling through the path of its orbit in front of a star is shown with a dotted arrow. Below this, the brightness of the observed star is shown over time correlating to the position of the planet in its orbit, referred to as a "light curve". As the planet passes in front of the host star, some flux from the host star is blocked and a dip in the overall brightness can be seen in the light curve at the bottom. Figure from NASA Ames.

1.1.1 The Transit Method

The transit method exploits a very specific orbital alignment geometry in which the exoplanet passes directly between the observer and the planet's host star. In this manner, some of the flux from the host star is blocked by the opaque body of the planet as it passes in between the observer and the star and the overall stellar brightness measured by the observer is diminished. As the planet passes across the stellar disk, the diminished brightness remains relatively constant before the planet passes past the edge of the stellar disk and the observed brightness of the host star returns to normal. This dimming event is referred to as the transit of the planet. This effect repeats at the cadence of the orbital period of the exoplanet, producing a regularly detectable signal indicative of an orbiting body (Deeg & Alonso, 2018). A schematic illustration of what this effect looks like to the observer can be found in Figure 1.2.

From a transit, it is possible to ascertain the radius of the planet as the amount of light blocked by the planet in transit is directly proportional to its size according to the square of the ratio of the planet's radius to the radius of the host star – $(R_p/R_*)^2$. Additionally, the inclination of the planet's orbit relative to the observer can be determined via the projected distance between the planet and star centers. This is known as the impact parameter, b, which is normalized to the stellar radius such that it carries a value between 0 and 1 and can be obtained through the measurement of time between beginning of ingress and end of egress, t_T, and the duration of the full planetary disk occluding the stellar disk, t_F. Furthermore, information can be inferred about the host star based on these parameters. These parameters can be combined with Kepler's third law to provide the stellar density, ρ_*, and the transit shape can be used to measure the limb darkening of the host star. Stellar disks are not uniform and display limb darkening, where the outer parts of the stellar disk are dimmer than the middle part due to changing optical depth and effective temperature at the limbs compared to the center. Thus, as the planet crosses over portions of the stellar disk of varying brightness, it is possible to determine how the brightness of a star's limbs compare to its center.

Since this method relies on a specific alignment geometry, the probability of observing such a transit for any given star from a random direction is quite small as the inclination of a planet's orbital plane must be seen edge-on by the observer (~90°). The probability for a randomly-oriented planet on a circular orbit to be aligned correctly for a transit is

$$p \approx \frac{R_* + R_p}{a} \simeq 0.005 \left(\frac{R_* + R_p}{R_\odot}\right) \left(\frac{a}{1\mathrm{AU}}\right)^{-1} \tag{1.1}$$

where R_* is the radius of the host star in solar radii and a is the semi-major axis in astronomical units (Borucki & Summers, 1984). Due to the dependence of transit probability on a planet's semi-major axis, this method is heavily biased towards finding planets that orbit close to their stars, although even planets orbiting at the periods of the inner planets of our Solar System have no more than a $\sim$1% chance at transiting when observed from a random direction. In contrast, many hot Jupiters have transit probabilities of $\sim$10% or more because they have orbits of $<$10 days compared to the 88 day orbit of Mercury. This makes hot Jupiters ideal targets for transit observations. It is also worth noting that transit probability is agnostic to the distance of a star from an observer, although other factors such as photometric accuracy suffer from the attenuation of a star's brightness with distance.

Not only is the probability of transit small, but the change in brightness produced by the transiting exoplanet is quite small as well. For a planet the size of Jupiter, this is often on the order of a 1% dip in brightness of the host star, whereas for smaller planets orbiting Sun-like stars, such as the Earth or Venus, the change in brightness can be on the order of hundredths or even thousandths of a percent (Seager & Mallén-Ornelas, 2003). This means that observing terrestrial planets around Sun-like or larger stars becomes exceedingly difficult, even under ideal conditions. The best prospects for planet discovery using the transit method are therefore large planets or planets orbiting small stars, such as M dwarfs (Haghighipour et al., 2010) or even white dwarfs (Drake et al., 2010; Agol, 2011; Faedi et al., 2011).

Despite the challenge of detecting small signals from planets with very specific alignments, the transit method is by far the largest contributor to planet discoveries of any method to date, far surpassing the number of discoveries of all other methods combined. Figure 1.3 illustrates the cumulative number of exoplanet discoveries per method broken down by year and the huge volume of transiting planet discoveries is apparent. And even though the transit method is the most common detection technique, we are still only observing a fraction of all planets expected

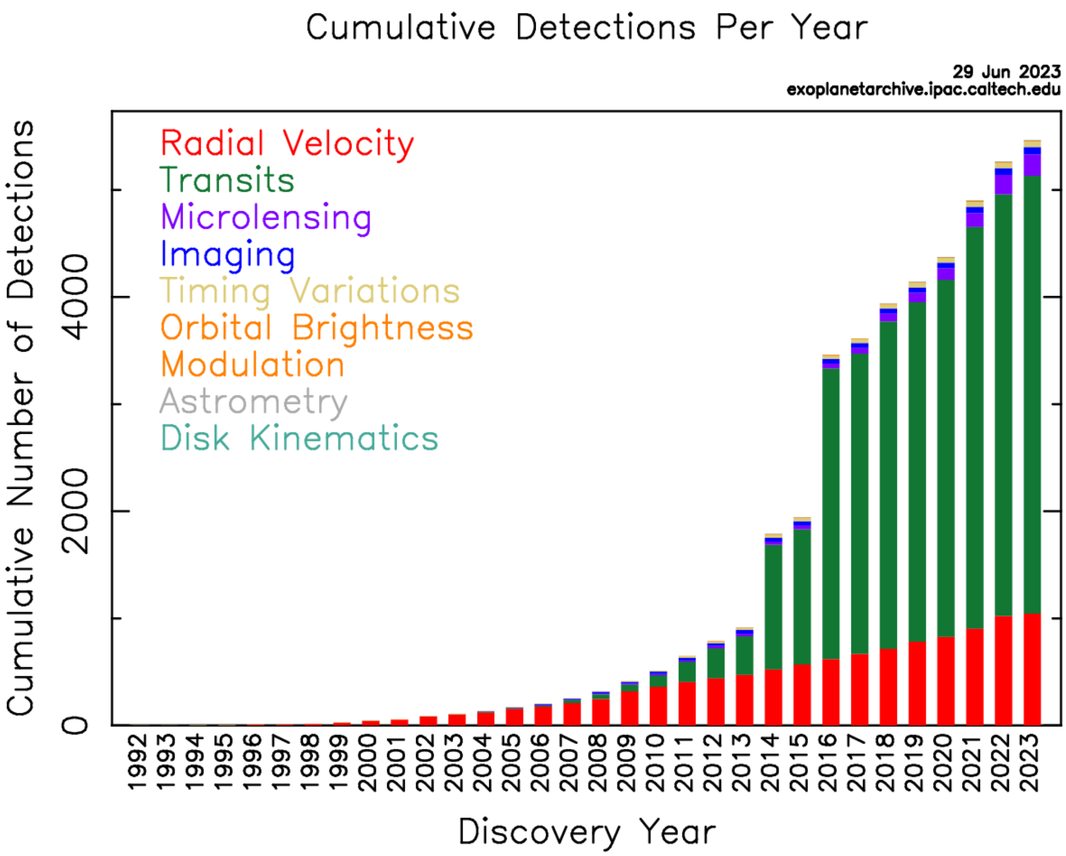

Figure 1.3: The cumulative distribution of planet discoveries by detection method over time. Not only are the total number of exoplanet discoveries increasing with time, but ever since around 2014, the transit method (green) has come to dominate exoplanet discovery. Figure from the NASA Exoplanet Archive: https://exoplanetarchive.ipac.caltech.edu/

to be in the galaxy since this method is insensitive to planets without edge-on orbits that may be present around stars with no currently known planets and transit surveys are magnitude-limited.

This prevalence of transiting exoplanet discoveries is partially due to the ease with which large numbers of stars can be searched for transits. It is fairly straightforward for one or more telescopes to perform a photometric survey of the sky at a short cadence in a sort of shotgun approach to picking out transit signals from individual stars contained within the survey field of view. Such a survey was described as early as 1971 by Rosenblatt (1971) and later refined by Borucki & Summers (1984) to outline a ground-based, wide-field planet survey. It was not until the early 2000s with the Optical Gravitational Lensing Experiment (OGLE, Udalski et al., 2002a,b) that a concerted ground-based observing campaign was established. This was later followed by searches with the Hungarian-made Automated Telescope Network (HATNET, Bakos, 2018), the Wide-Angle Search for Planets (WASP, Pollacco et al., 2006; Collier Cameron et al., 2009), and many others.

These ground-based surveys, while prolific, often suffered precision loss due to atmospheric effects and temporal limitations due to Earth's day-night cycle. Thus, space-based searches were required to make leaps in progress in transit surveys. The first of these was the COnvection, ROtation and planetary Transits satellite (CoRoT, Auvergne et al., 2009; Moutou et al., 2013) that detected the first super-Earth size planet CoRoT-7b with a radius of $1.68R_{\oplus}$ (Léger et al., 2009), which introduced an entirely new class of planets. CoRoT was followed up by the Kepler (Borucki et al., 2010) and K2 (Howell et al., 2014) missions as well as the currently-operating TESS mission (Ricker, 2015). TESS is already well into its second mission extension, having surveyed over 90% of the sky (see Figure 1.4) with potential plans to survey 99% of the sky by the end of its third extended mission. TESS is responsible for identifying over 6,000 planet can-

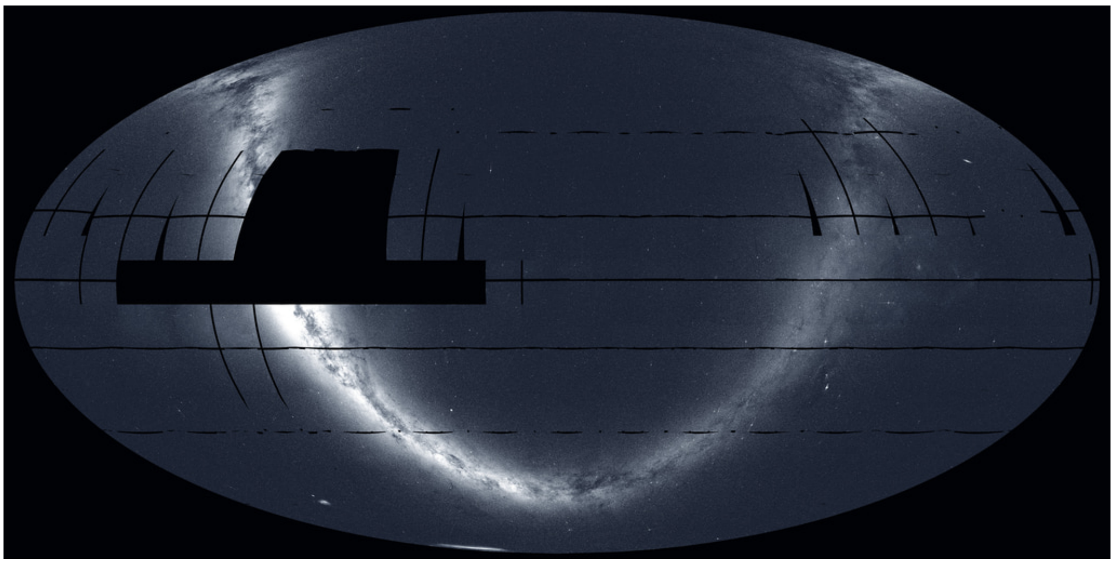

Figure 1.4: A mosaic image of all TESS data taken as of December, 2022. Most of the sky has been observed by TESS, save for a large hole in the left side of the image. This is due to contamination from the Sun and the Moon precluding the observation of that region of sky without risking damage to the onboard instruments and high photometric noise. Future TESS observations may fill this gap in the data. Other gaps can be seen sporadically throughout the sky map. This is due to the TESS observing strategy which observes the sky in strips called sectors. The edges of these sectors are not always flush with one another and result in slivers of unobserved sky. Additional gaps are due to the space between CCDs. Figure from Ethan Kruse.

didates to date and its almost full-sky coverage coupled with space-based photometric precision has produced an explosion of new potential planets. These planet candidates continue to provide exciting new discoveries that enrich our understanding of planet formation, evolution, and demographics.

1.2 Determining the Planetary Nature of a Transit

Although there has been an explosion of transit discoveries as outlined in Section 1.1.1, there has also been an explosion of false positive scenarios that mimic the transit durations, depths, and periods of a planet but are caused by some other astrophysical configuration (Brown, 2003; Charbonneau et al., 2004). Therefore, it is necessary to demonstrate that transit-like signals are definitely not or at least highly unlikely to be caused by these false positive scenarios in order for a signal to be referred to as a planet rather than a planet candidate. This is accomplished through a series of analysis procedures, each imparting different levels of confidence that the signal is indeed caused by a planet.

1.2.1 False Positive Scenarios

Almost all false positive scenarios are centered on the idea that it is a star rather than a planet causing the signal. In these cases, the configuration of the system is the same as if it were a planet causing the transit, but instead of a planet passing between the observer and the host star, it is another star. These types of stellar systems are termed "eclipsing binaries" since they exist in a binary stellar configuration and happen to eclipse one another from our point of view. An illustration of the various types of false-positive scenarios is shown in Figure 1.5.

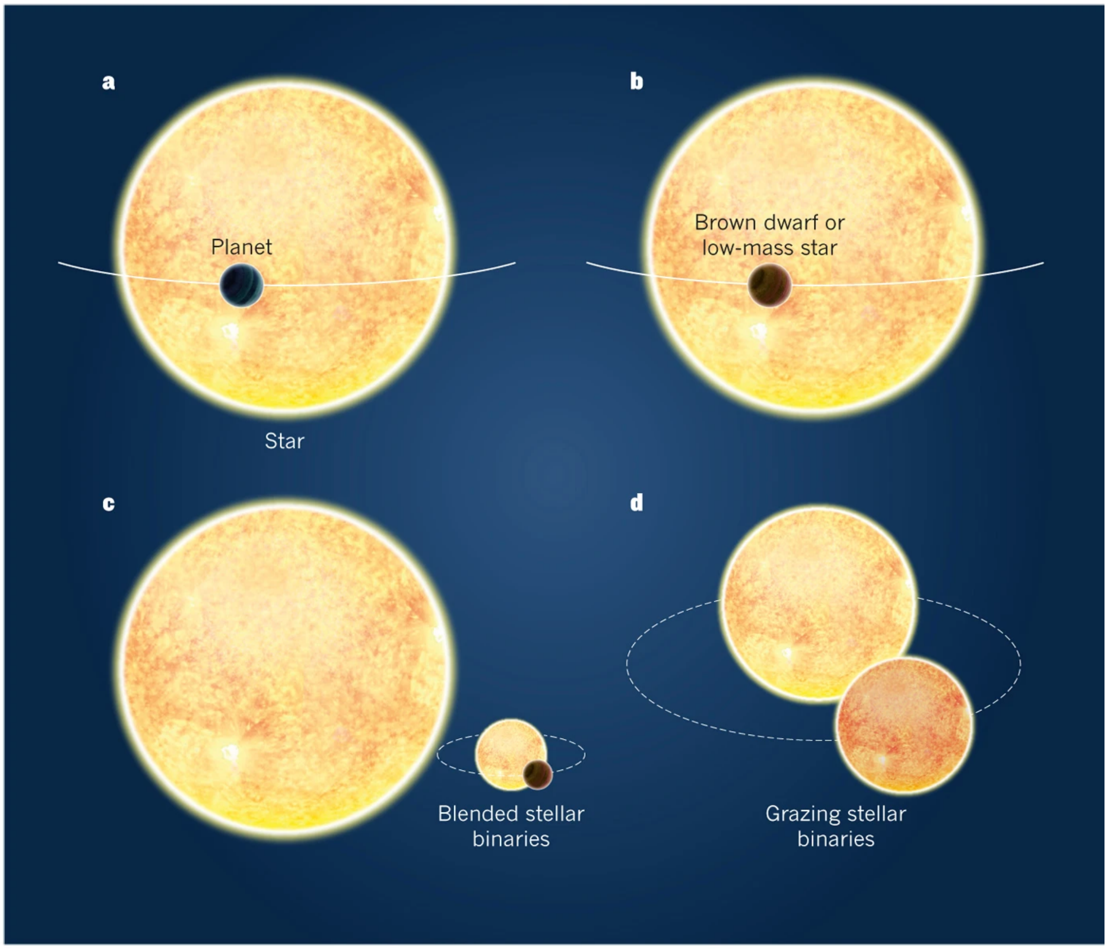

Figure 1.5: An illustration of the main astrophysical scenarios causing a transit-like event. (a) a planet orbiting its host star; (b) an orbiting brown dwarf or low-mass star with similar radius to a planet; (c) a blended stellar binary in a triple-star system with deep eclipses that are strongly diluted by a bright neighboring star, mimicking the much shallower transits of a planet; (d) grazing binary stars in which the disks of each star only overlap by a small amount at each eclipse, preventing the full radius of the orbiting object from being determined and mimicking a shallower planet transit. Starspots are not shown in this figure as they produce signals that are sinusoidal rather than transit-like, although the signals may appear transit-like in rare edge cases such as data with a low signal-to-noise ratio. Figure from Cameron (2012).

One of the most common astrophysical false positive scenarios is that of the blended eclipsing binary (BEB; Evans & Sackett, 2010; Haswell, 2010). This occurs when an eclipsing binary is located along the same line of sight as the target and the periodic signal from the BEB is mixed with the light from the target star, thereby creating the illusion that the background signal is originating from the target star. BEBs are also sometimes referred to as nearby eclipsing binaries (NEBs).

In many BEB scenarios, two stars of equal mass produce grazing eclipses at half their orbital period. Although normally the large radius of a star would produce deep eclipses, the grazing nature of the eclipses is caused by only part of the stellar disks passing in front of one another, therefore producing shallower eclipses that can mimic the depths of a planet transit (Cameron, 2012). If the stars are not of equal mass, then the differing temperatures, brightnesses, and radii of the stars would produce transit depths that vary with every-other eclipse (called odd-even transit variation).

On the other hand, the eclipsing binary could consist of a main sequence primary star that is eclipsed by a brown dwarf or a white dwarf, both of which have smaller radii that are closer to that of hot Jupiters or even Earth-size planets and can masquerade as such. This allows for a wider range of orbital inclinations and is difficult to disentangle from a planetary scenario with photometry alone (Brown, 2003). Both the grazing binaries of similar masses and the brown dwarf/white dwarf BEB scenarios can be complicated by the line of sight. It's possible that these BEB scenarios exist in the same line of sight as the target, but due to the pixel size of the photometric detector or a large point spread function (PSF) for a given instrument, it is often difficult to determine which star the signal is originating from (Bryson et al., 2013; Coughlin et al., 2014a).

In fact, it's also possible for a BEB to be diluted by the flux from the target or another nearby star, thus making the eclipse shallower and even closer to that of an exoplanet transit. This line of sight issue becomes more prevalent for instruments with larger pixel sizes (Collins et al., 2018), such as TESS, which has a pixel width of 21 arcsec. This is why instruments with larger pixel sizes often require more intensive vetting and validation procedures to rule out false positives.

It is also worth noting that any of the configurations illustrated in Figure 1.5 could also represent the target itself and not all false positives are due to a background or nearby system. Starspots can also, in rare cases, result in a false positive transit, although this the signal produced by starspots is often sinusoidal in nature and distinct enough from transit-like features such as to be easily identified. Starspots are primarily an issue in low signal-to-noise data.

1.2.2 Vetting, Validation, and Confirmation

Exoplanet "vetting" consists of a suite of diagnostic analyses that can be applied to each planet candidate in order to identify transit-like signals that are caused by BEBs. Torres et al. (2011) outlined four diagnostic vetting tests applicable to photometric data which were implemented by Sullivan et al. (2015) for use with TESS data. These are (1) the search for ellipsoidal variations which are gradual sinusoidal changes in brightness in the out-of-transit portions of the light curve over the course of an orbital period due to the ellipsoidal shape of the stars in the eclipsing binary caused by the gravitational distortion of each into ellipsoids (Mazeh, 2008); (2) the existence of secondary eclipses – the blocking of light emitted by the planet or star when it passes behind the primary star – with depths consistent with objects at the temperature of a star; (3) V-shaped transit shapes that are caused by lengthy ingresses and egresses due to eclipsing objects that are similar in size; and (4) a so-called "centroid shift" where the centroid of the difference between the in-transit and out-of-transit portions of the light curve shift from the centroid of the baseline flux, indicative of a background object as the source of the transit-like signal. Chromaticity can also be used to identify transits due to BEBs since stars of differing effective temperatures will exhibit blackbody spectral energy distributions centered at different peak wavelengths, causing the transit depth to vary as a function of bandpass.

There are other vetting procedures, such as the comparison of the odd and even transit depths to determine if the transits are being caused by two stars at half the observed period as well as the collection of reconnaissance follow-up observations (e.g. Kostov et al., 2019a). These observations can include additional photometry at higher spatial resolution to check nearby targets for obvious eclipsing binaries or determine if a transit is chromatic, spectroscopy to constrain the maximum amplitude of a radial velocity signal, or high-resolution imaging to rule out or constrain the presence of additional unresolved stars in the target system. Not all targets are required to undergo all forms of vetting, however, more rigorous vetting of each target increases the likelihood that the signal is caused by a planet rather than a false positive (Torres et al., 2011). It is important to note that transit-like signals that pass through vetting without being ruled a false positive are still considered planet candidates rather than planets (Alonso et al., 2004; Charbonneau et al., 2004).

The next level of confidence in the planetary nature of a transit-like signal comes through a process termed "validation". There are two means through which a planet candidate can become validated: statistical validation and photometric validation (Brown, 2003; Morton, 2012a).

Statistical validation involves the use of statistics to rule out portions of parameter space where it is possible that the signal is due to a false positive. More often than not, this process employs the use of specially-created statistical validation software such as vespa (Morton, 2012a, 2015a) and TRICERATOPS (Giacalone et al., 2021a). Based on the planetary and orbital parameters of the potential planet as well as its position on the sky and sometimes even the observatory or extraction aperture used to discover the signal, these software packages generate a set of priors for a host of astrophysical false positive scenarios, incorporating any follow-up observations as constraints. They then run a Markov Chain Monte Carlo (MCMC) simulation to determine in which portions of parameter space a false positive scenario can and cannot reproduce the user-provided transit. This is often heavily based on the shape of the transit. Each statistical validation software compares against a set of astrophysical false positive scenarios involving an additional stellar companion as the source of the transit-like signal. After calculating the posterior probabilities of each false positive scenario, statistical validation provides a final false positive probability (FPP) for the target, which, if below a certain threshold (often $\sim$1%), indicates that the signal is almost certainly caused by a planet. The primary difference between vespa and TRICERATOPS is that the latter incorporates the actual background stellar field in its FPP calculation and was developed specifically for use with TESS data.

Alternatively, a signal can be validated photometrically, which involves observing the transit-like signal in multiple wavelengths (e.g. O'Donovan et al., 2007; Colón & Ford, 2011; Parviainen et al., 2020). Stars are self-luminous, meaning that if a star were to eclipse another star, the depth of the eclipse would not be the same as if the eclipsing body were opaque – such as a planet would be – since the observed flux is the sum of the primary star as well as the eclipsing star. Additionally, since stars can be approximated as blackbodies, the flux emitted by each star varies with wavelength. Therefore, if an eclipsing binary is the cause of a transit-like feature, then the depth will vary with wavelength since the summed relative flux would change based on the bandpass used to observe the system (Mandushev et al., 2005; O'Donovan et al., 2006). Since a planet is opaque and has a small wavelength dependence on the proportion of a star's light that it occludes, the broadband transit depth should not change significantly with wavelength if a planet is causing the transit[2]. Transits that do not change significantly between broadband multiwavelength observations can also be considered validated. Validated planets are no longer considered candidates, but are at this point deemed planets.

Although validated signals are considered planets, they are still only highly likely to be planets rather than definitely planets. The process of "confirming" a planet is the only way to be sure that a planet is indeed 100% a planet. To confirm a planet, it is necessary to measure the planet's mass (e.g. Hellier et al., 2017; Cañas et al., 2022; Silverstein et al., 2022). This is most often accomplished through radial velocity measurements since most false positive scenarios produce radial velocity signatures that are inconsistent with a planet-mass body orbiting the host star. Additionally, radial velocity data provide the means to uncover truly pathological false positive scenarios such as multi-star configurations. Brown dwarfs are small enough to masquerade as planets, but have masses far larger than a planet would. Thus, multiple detection methods are required in order to turn a transiting planet candidate into a confirmed planet and radial velocities in particular constitute the "gold standard" for planet confirmation.

[2]There is a potential for transit depth dependence on wavelength in the case that the planet possesses an atmosphere with absorping chemical species that are not shrouded by opaque cloud layers. This effect exhibits different wavelength dependence than an eclipsing binary would, however.

1.3 Hot Jupiters

Before the first exoplanets were discovered, our ideas of what extrasolar planetary systems would look like were largely based on our own Solar System, with inner terrestrial planets and outer gas giants. This conceptualization informed our theories on planet formation and evolution, where planets formed from a cloud of gas and dust that collapsed into a disk. In this disk, beyond the snow line where the surface density and mass of the disk are higher, rocky cores grew quick and massive enough to accrete lighter elements directly from the protoplanetary nebula, producing planets with gaseous atmospheres. Interior to these large gaseous planets, rocky cores were too small to accrete a thick gaseous envelope and instead gained thinner atmospheres after the dissipation of the gas disk, creating rocky planets on coplanar orbits (Pfalzner et al., 2015).

Immediately with the discovery of the first exoplanets, this conception of planetary systems was challenged. As the first exoplanet discovered around a main sequence star, 51 Pegasi b upended the model of inner rocky planets and outer gas giants as it zipped around its host star on a 4.23 day orbit with a mass of almost half that of Jupiter (Mayor & Queloz, 1995). This discovery defined an entirely new category of planets, the "hot Jupiters", which would dominate the first decade of planet discoveries in both the radial velocity and transit searches. This category of planets was so striking since not only do we not possess any sort of analogue in our Solar System, but the existence of these gaseous planets so close to their host stars contradicts much of what we thought possible from the planetary evolution theories we had developed (Lin et al., 1996; Rasio & Ford, 1996; Weidenschilling & Marzari, 1996). The effort to understand hot Jupiters and how they arrived at their current positions has already yielded a treasure trove of information on how planets form and evolve, but there are still many unanswered questions waiting to be addressed.

1.3.1 Population Features

As stated at the beginning of this chapter, hot Jupiters are defined as planets with radii $>$ 8 $R_\oplus$ orbiting their host stars on short orbits with periods $<$ 10 days (Winn et al., 2010; Wang et al., 2015; Garhart et al., 2020). Various subclasses of hot Jupiters exist, such as "ultra-hot Jupiters" that have dayside temperatures $\geq$ 2,200 K and have distinct atmospheric characteristics (Parmentier et al., 2018). The definitionof what constitutes a hot Jupiter is, for the most part, based on arbitrary distinctions with little physical motivation separating giant planets on orbits with periods $<$ 10 days from those on orbits with periods $>$ 10 days, called "warm Jupiters". Distinctions such as when the characteristic tidal locking timescale becomes longer than the age of the system and distance at which a hot Jupiter experiences radius inflation are highly dependent on stellar and system parameters and cannot be cleanly defined by a 10 day orbital period cutoff.

As of writing, the NASA Exoplanet Archive currently lists more than 550 confirmed hot Jupiters. This fraction represents approximately 10$\%$ of all currently known confirmed planets that it lists. Although this prevalence of hot Jupiters in the observed exoplanetary sample indicates that these objects constitute a distinct class of planets rather than a handful of outliers, the 10$\%$ statistic overstates their occurrence around observed stars. Hot Jupiters are relatively rare in the Galaxy with only $\sim$1$\%$ of all sun-like stars possessing a hot Jupiter (Howard et al., 2012; Wright et al., 2012). This occurrence rate drops off even lower for low-mass stars starting at M dwarfs and for high mass stars as well starting around A dwarfs (Johnson et al., 2010). This is not to say that hot Jupiters do not or cannot exist around the lowest and highest mass main sequence stars, they simply occur at far lower rates. In fact, almost all hot Jupiters tend to orbit around F, G, and K dwarfs, exhibiting a strong positive correlation between host star metallicity and hot

Jupiter occurrence (Beleznay & Kunimoto, 2022) but the search for hot Jupiters around the lowest and highest masses of stars is an active field of research as it can inform hot Jupiter formation pathways in these systems (e.g. Gan et al., 2022).

The reason that hot Jupiters comprise so much of the currently known exoplanet sample despite being relatively rare is that most exoplanet detection methods are biased towards finding them. In the initial radial velocity searches of the 1990s and early 2000s, multiple orbits of a planet were required in order to confidently claim a detection as observing multiple periods of a sinusoidal variation more confidently rules out false positives or instrumental noise. Furthermore, larger masses result in larger Doppler shifts of the host star, resulting in larger signals that are easier to detect. Hot Jupiters are not only very massive, but they orbit on short periods, allowing for more full orbits of a hot Jupiter to be captured by radial velocity searches in a shorter period of time. Likewise, when looking for transits in photometric data, the same biases exist towards large planets that create deeper transits and short orbits that allow for a higher signal-to-noise ratio from the ability to stack more transits on one another. The short orbital periods are also able to be identified and constrained more readily as there are more opportunities to observe a transit, removing ambiguity in the orbital period much more easily. Additionally, as discussed in Section 1.1.1, the probability of transits scale proportionally with both proximity to the host star and planet size. As large planets close to their host stars, hot Jupiters occupy the portion of parameter space that most planet searches are biased towards. This has led to hot Jupiters playing an outsized role in our understanding of the internal structure, atmospheric composition, and orbital architecture of planets outside of our Solar System.

Because of the relatively large sample of hot Jupiters that we have to draw from, we have been able to probe some of the most baffling questions about the formation and evolution of this class of planets based on the population-wide trends observed. A significant fraction of the hot Jupiters that have been discovered orbit on periods centered around ∼3-4 days. This is referred to as the "three-day pileup" (Dawson & Johnson, 2018). It is possible that part of this trend is due to selection effects stemming from ground-based transit surveys (Gaudi et al., 2005), but it is likely also due to the evolution of the hot Jupiters over time. Although an orbital period of ∼3 days is well beyond twice the Roche limit for most present-day hot Jupiters, it may have been much closer or even within the Roche limit during the high-eccentricity migration of hot Jupiters prior to their cooling and subsequent contraction. This would have caused the tidal disruption of some hot Jupiters with an orbital period less than ∼3 days, resulting in a dearth of remaining planets interior to this period (Dawson & Johnson, 2018). This observed pile-up may also be due to disk migration which is expected to bring hot Jupiters to half the corotation period of less than ∼5 days. Additional tidal effects also sculpt the hot Jupiter semimajor axis distribution after formation, causing the observed semimajor axes to deviate from a distribution purely due to formation mechanism.

Additionally, many hot Jupiters exhibit high obliquity in their orbits, meaning that the plane of the planet's orbit is misaligned with the rotational plane of the host star. This is in stark contrast to the results of the formation theories developed from studying our Solar System which hold that planets form in neatly aligned orbits. The diversity of obliquities observed in the hot Jupiter population suggests that a variety of these systems underwent dynamically active evolution at some point in their histories (Wang et al., 2021; Rice et al., 2022).

Another population-wide facet of hot Jupiters is that they are almost always the only planet in a given star system within a factor of 2 or 3 in orbital distance (Steffen et al., 2012; Knutson et al., 2014; Endl et al., 2014; Hord et al., 2021). This has led hot Jupiters to being labeled

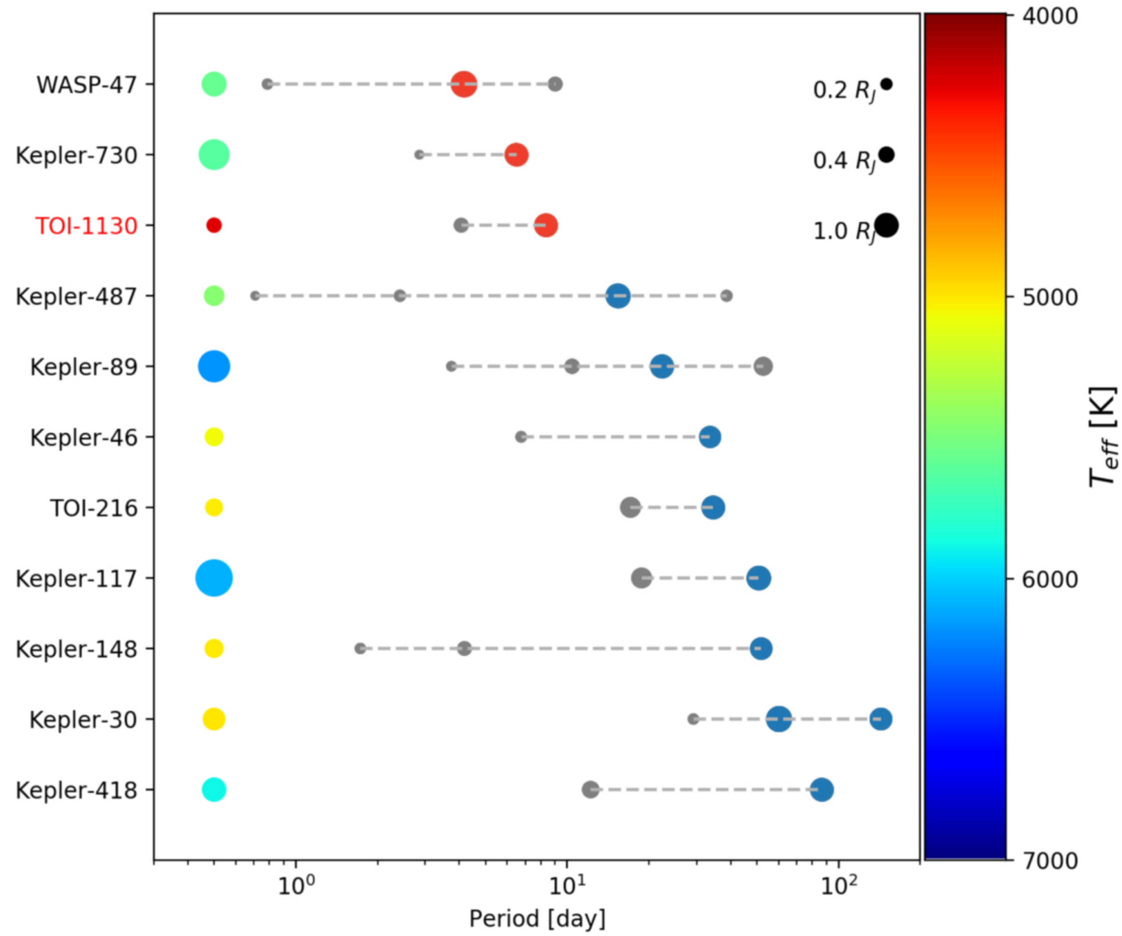

Figure 1.6: Pictogram of the distribution of hot and warm Jupiters with nearby companion planets as a function of orbital period. Hot Jupiters are shown in red and warm Jupiters are shown in blue. The other nearby planets in their systems are shown in gray and connected to them by a dashed line. The size of the planets corresponds to their radius. The host stars of each system are depicted by the circle on the left side of each row, scaled by their radii and colored by their effective temperature. Only a selection of hot and warm Jupiters are displayed. Warm Jupiters are far more likely to possess nearby companion planets than hot Jupiters, with $\sim$50% of warm Jupiters orbiting nearby companion planets. Figure from Huang et al. (2020a).

as "lonely" Jupiters due to the lack of other nearby planets in their systems. This holds true across the population with only a few exceptions (WASP-47, Kepler-730, TOI-1130, WASP-132; Becker et al., 2015; Cañas et al., 2019; Huang et al., 2020a; Hord et al., 2022, respectively). This is in stark contrast to the warm Jupiters – gas giants on orbits with periods of 10-200 days – of which 50% have nearby companion planets in their systems (Huang et al., 2016), but as noted above, the distinction between warm Jupiters and hot Jupiters is not physically-motivated and the populations may have many similarities that transcend the defined boundary. Figure 1.6 illustrates this continuity of hot and warm gas giants with nearby companion planets in their systems.

Section 1.3.2 explores the potential causes of these observed trends among the hot Jupiter population and the various formation pathways through which hot Jupiters form.

1.3.2 Formation Pathways

Many of the unique population-level characteristics displayed by hot Jupiters can be tied back to the pathways through which they form. Indeed, the formation of hot Jupiters has been an active field of study ever since they were first discovered by Mayor & Queloz (1995). Oftentimes, the observed population characteristics can be studied in order to deduce how a hot Jupiter or set of hot Jupiters formed and the two go hand-in-hand.

One of the competing hypotheses for hot Jupiter formation was that they formed at or near their current orbits, which was informed heavily by planet formation theories developed through study of the Solar System. Lin et al. (1996) demonstrated that 51 Pegasi b could not have formed at its current distance from its host star because the temperatures at that distance are too great to allow small solid particles to build up a sufficiently large core to accrete gas and

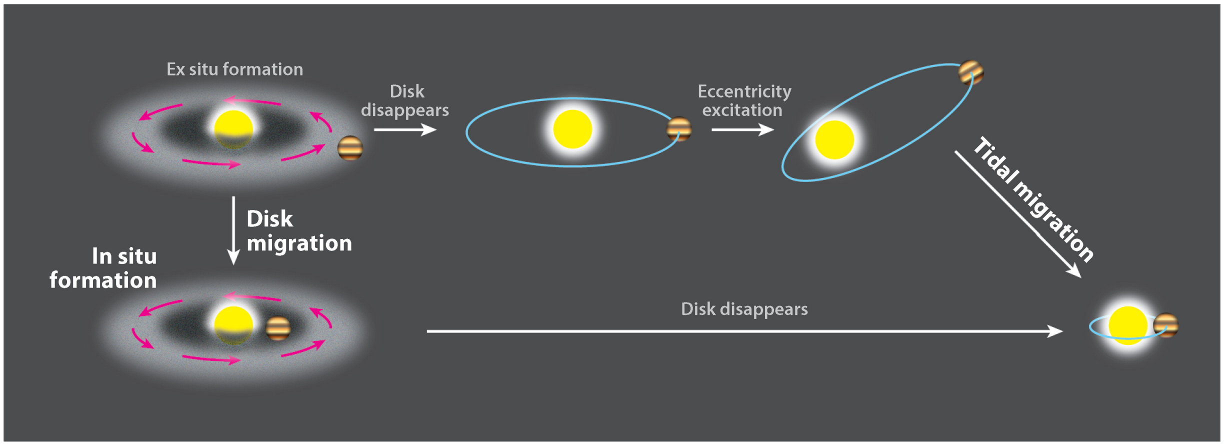

Dawson RI, Johnson JA. 2018.
Annu. Rev. Astron. Astrophys. 56:175–221

Figure 1.7: An illustration outlining the three main pathways of hot Jupiter formation. Both of the formation pathways that invoke planetary migration begin in the upper left corner with the stage labeled "Ex situ formation" while the in-situ formation pathway begins in the lower left corner. The arrows are meant to denote the order of each formation mechanism through time. Figure from Dawson & Johnson (2018).

that the temperature of the star would have evaporated the proto-hot Jupiter. They instead invoked planetary migration as a probable cause for hot Jupiter formation, where the gaseous planet forms in the outer part of the stellar system beyond the ice line and migrates inwards.

There are currently three main pathways through which it may be possible for a hot Jupiter to form: in-situ formation, disk migration, and high-eccentricity migration (Dawson & Johnson, 2018). These formation pathways are illustrated in Figure 1.7. It is likely that a combination of multiple formation pathways is required to accurately describe the observed hot Jupiter population.

In-situ formation: As the name implies, in-situ formation occurs when the hot Jupiter forms at or near its current position. In order for in-situ formation to be a viable formation pathway for hot Jupiters, one of two mechanisms of giant planet formation must hold true at such close distances to the host star: gravitational instability, in which portions of the protoplanetary disk fragment into bound clumps that then collapse (Boss, 1997; Durisen et al., 2007), or core accretion, in which a rocky protoplanet core forms and accretes a gas envelope many times its mass from the surrounding protoplanetary disk (Perri & Cameron, 1974; Mizuno, 1980; Stevenson, 1982; Pollack et al., 1996). It is highly unlikely that either gravitational instability or core accretion could operate at the location of hot Jupiters' current orbits (Rafikov, 2005, 2006).

In the gravitational stability scenario, planets form when the freefall time of a portion of the protoplanetary disk is high enough to overcome Keplerian sheer. This is parameterized by Toomre (1964) in the form of the parameter Q:

$$Q = \frac{2\sqrt{kT/\mu}}{GP\Sigma_{gas}} \tag{1.2}$$

where T is the temperature, μ is the mean molecular weight, k is the Boltzmann constant, P is the orbital period, G is the universal gravitational constant, and Σ_{gas} is the gas surface density. In cases where $Q \lesssim 1$, the gas disk is unstable and may collapse to form protoplanets. At the short orbital periods of present-day hot Jupiters, the rapid rotation of the protoplanetary disk and the high temperatures from stellar irradiation support the local gas against gravitational collapse. Although the surface density of the protoplanetary disk is higher closer to the star, it is not enough to overcome the rapid rotation and high temperatures of the region to collapse and form gas giants (Rafikov, 2005, 2006).

In the core accretion scenario, gas giant planets form when a core of $\sim$10 $M_\oplus$ forms and accretes gas from the protoplanetary disk (Pollack et al., 1996; Rafikov, 2006). To do this, the area of the protoplanetary disk where hot Jupiters are currently observed must not only have enough refractory material to grow a $\sim 10 M_\oplus$ core, but must grow it before the gas disk dissipates. This is not expected to be the case as the portions of the protoplanetary disk at the short periods of a hot Jupiter do not have enough solids to build such a massive core, and thus the accretion of a gaseous envelope never begins.

Work performed by Batygin et al. (2016) reasserts the viability of in-situ formation as a hot Jupiter formation pathway, although large cores are still required and are difficult to produce at the requisite orbital periods. In-situ formation remains a highly unlikely formation pathway for hot Jupiters, therefore implying that hot Jupiters most likely formed elsewhere and migrated to their currently observed positions.

Disk migration: In the process of disk migration, a gas giant first forms in the outer parts of the stellar system, akin to how the gas giants in the Solar System presumably formed. Prior to the dissipation of the protoplanetary disk, however, gravitational interactions between the disk and the gas giant can produce torques on the planet's orbit and cause a migration of the planet within the disk (e.g. Goldreich & Tremaine, 1980; Lin & Papaloizou, 1986; Lin et al., 1996; Ida & Lin, 2008).

There are two main types of torques that act upon the planet's orbit due to interaction with the protoplanetary disk: Lindblad torques and corotation torques. Lindblad torques arise from the interaction between the planet and the spiral density waves raised by the planet within the disk. These spiral density waves carry away angular momentum from the planet's orbit, resulting in a negative torque that causes the planet's orbit to shrink. The amplitude of this effect is based on the mass of the planet, with more massive planets raising larger spiral density waves on the disk and enhancing the effect of Lindblad torques (Ward, 1997). Conversely, corotation torques are caused by the exchange of angular momentum between the planet's orbit and the disk material within its co-orbital region. These torques are most often positive and result in an outward migration

(Paardekooper & Mellema, 2006; Duffell & Chiang, 2015). They are highly dependent on the surface density of the material in the planet's co-orbital region, so in the case of a large planet that is able to cut a deep channel in its disk, corotation torques will be smaller. In the case of gas giants that eventually become hot Jupiters, the magnitude of the Lindblad torques is larger than that of corotation torques, resulting in a net inward migration (Tanaka et al., 2002). This is referred to as Type II migration (where Type I migration is when corotation torques are larger than Lindblad torques).

To prevent runaway migration, this process must be halted at some point prior to the engulfment of the planet by the host star. While the specific processes may be very case-by-case dependent, a planet's migration can be halted in a number of different ways. One potentially dominant halting process is that the protoplanetary disk can dissipate, removing the source of both Lindblad and corotation torques entirely, leaving the gas giant at the orbital period it was on at the time of disk dissipation (Trilling et al., 1998, 2002; Lecar & Sasselov, 2003). Another family of halting processes involves an inner truncation of the protoplanetary disk, beyond which a planet could not migrate as the disk ends prior to reaching the planet's Roche limit. This can be due to something such as the host star's magnetosphere or perturbations from another stellar companion (Rice et al., 2008; Chang et al., 2009).

Disk migration is a dynamically quiet process, oftentimes allowing for multiple planets to migrate inwards together and preserve the initial relative architecture of the system. It is often possible for planets in a system that has undergone disk migration to get trapped in orbital resonance with one another (Malhotra, 1993; Lee & Peale, 2002; Raymond et al., 2006) – when the orbital periods of two planets are low integer ratios of one another (e.g. 2:1, 3:2, or 3:1 resonance). These resonances can excite the planets into high mutual inclinations, resulting in planets that are not all orbiting within the same orbital plane (e.g. Thies et al., 2011; Batygin, 2012; Rogers et al., 2012; Lai, 2015). A lack of observed inner companions in resonant orbits with the hot Jupiter has historically been interpreted as evidence against disk migration as the dominant hot Jupiter formation mechanism, although it likely still plays a role in a subset of the hot Jupiter population.

High-eccentricity migration: Unlike disk migration, high-eccentricity migration occurs after the protoplanetary disk has dissipated and does not rely on the disk-planet interactions to drive the gas giant's migration. Instead, the gas giant gravitationally interacts with other orbiting bodies or a stellar flyby to extract the planet's angular momentum and place it onto a high eccentricity orbit that brings it to the inner regions of the stellar system. Once the gas giant is on a highly eccentric orbit, the tidal interactions between the planet and the star at times of close approach dissipate the gas giant's orbital energy, causing its orbit to circularize at a semi-major axis close to the star. At periapse, the gas giant undergoes close passages to the host star, raising tides on the planet, and dissipating energy as its shape deforms in accordance with the rapidly changing tidal potential (Fortney et al., 2021).

There are multiple mechanisms that are thought to be able to reduce the gas giant's initial orbital angular momentum to place the planet on a highly eccentric orbit, all of which involve interaction with one or more additional bodies. The first is planet-planet scattering, which converts differences in angular velocity between planets with different semi-major axes into angular momentum that is transferred from the gas giant to an outer planet, increasing the semi-major axis of the outer planet while simultaneously decreasing the semi-major axis of the inner one (Rasio & Ford, 1996; Weidenschilling & Marzari, 1996; Ford & Rasio, 2006; Chatterjee et al., 2008). This most often occurs in systems that are tightly packed when they form or systems that form with highly eccentric planets (Jurić & Tremaine, 2008; Shara et al., 2016). In planet-planet scattering, the gas giant's eccentricity grows over the course of multiple encounters with an outer planet. More massive planets closer in semi-major axis to the gas giant produce larger eccentricity changes in the gas giant's orbit, so a planet that will eventually become a hot Jupiter may need to eject one or multiple planets to achieve the eccentricity necessary for the tidal dissipation to lead to a hot Jupiter (Goldreich et al., 2004; Ida et al., 2013; Petrovich et al., 2014).

Other mechanisms for perturbing a hot Jupiter onto an eccentric orbit are secular, meaning they are slow exchanges of angular momentum between planets that are often widely separated, rather than the shorter timescale of planet-planet scattering (Petrovich, 2015). Although the main principle of secular interactions is the deposition of the gas giant's angular momentum into outer planets, the exact mechanism can differ based on the exact architecture of the system. For instance, in the case of three or more planets, secular chaos can occur, when this angular momentum transfer occurs chaotically (Wu & Lithwick, 2011). Alternatively, the transfer can occur periodically through Kozai-Lidov oscillations (Kozai, 1962; Lidov, 1962; Naoz, 2016). This effect occurs when the orbit of a two-body system (in this case, the gas giant and the star) is perturbed by a distant third body with either a nonzero mutual inclination or high eccentricity. This causes the orbital plane of the gas giant to precess and periodically exchange mutual inclination and eccentricity, eventually providing the gas giant with enough eccentricity to circularize through tidal interactions with the host star and settle in its orbit as a hot Jupiter. This outer third body can be either a star or a massive planet (e.g. Wu & Murray, 2003; Naoz et al., 2011; Teyssandier et al., 2013).

One further mechanism for reducing the gas giant's initial orbital angular momentum is a stellar flyby. In this scenario, a nearby star passes close to the outer edge of the planetary system and perturbs the orbit of the gas giant in its initial orbit, thus sapping its orbital angular momentum and placing it on a highly eccentric orbit. This is likely most common in dense stellar clusters (Shara et al., 2016).

All of these high-eccentricity migration mechanisms are dynamically active and oftentimes result in the scattering or ejection of one or more planets from the system. Additionally, in scenarios such as Kozai-Lidov oscillations, the orientation of the gas giant's orbit changes periodically and so it is not uncommon for hot Jupiter systems that have formed via high-eccentricity migration to exhibit high obliquities (Fabrycky & Tremaine, 2007; Chatterjee et al., 2008). That said, it is often possible for the tidal interactions between a gas giant and the host star during the process of orbital circularization to realign the star's spin axis with the hot Jupiter's orbital momentum vector, decreasing the obliquity of the planet (Winn, 2010; Albrecht et al., 2012).

Regarding the observed population features of hot Jupiters outlined at the end of Section 1.3.1, it is possible to tie many of them to the various formation mechanisms introduced here. The hot Jupiter population exhibits a $\sim$3 day orbital period pileup, a mixture of high obliquity and alignment, and a marked dearth of nearby planets in their systems. Were most hot Jupiters to form via in-situ formation, it is expected that their orbits would be located at or beyond the edge of the protoplanetary disk at $\sim$10 days (Lee & Chiang, 2017), which is not the case, although post formation migration could have occurred. Hot Jupiters that form via disk migration are expected to arrive at periods consistent with the observed pileup (Heller, 2019), while high eccentricity migration predominantly places hot Jupiter systems at or beyond twice the Roche limit (Nelson et al., 2017), which is beyond the observed pileup, although the orbits can shrink post-migration due to tidal interaction with the host star (Jackson et al., 2008; Valsecchi et al., 2014). In the case of obliquity, all formation scenarios are able to produce both aligned and misaligned systems. In terms of the dearth of nearby companion planets, high-eccentricity migration is the only mechanism that is expected to produce such a low occurrence of nearby planets in the system, matching what has been observed (Steffen et al., 2012; Knutson et al., 2014; Endl et al., 2014). However, given that high-eccentricity alone cannot explain the period distribution, nor can disk migration explain the dearth of companion planets, it is clear that multiple formation mechanisms are required to explain the observed hot Jupiter population (Dawson et al., 2014).

Additional observables such as eccentricity, hot Jupiter radius inflation, semi-major axis distribution, the age of hot Jupiter host stars, and the atmospheric properties of hot Jupiters, to name a few, are also critical in understanding the nature and evolutionary history of this unique population of planets (Dawson & Johnson, 2018). The study of hot Jupiter formation and evolution is still very active and has yet to reveal all of its secrets.

1.4 Observing Exoplanet Atmospheres

As we have seen through studying our own Solar System, the composition, physical processes, and evolution of a planet are not dependent on the dynamics of the orbit or its formation process alone. Rather, a planet's atmosphere plays an important role in the chemical and physical processes that define an individual planet (Madhusudhan, 2019; Wordsworth & Kreidberg, 2022). Indeed, the atmosphere of a planet is intrinsically tied to a planet's features and evolution and is as much a part of the planet as its size or orbit (Mollière et al., 2022). But, unlike planets in our Solar System that can be resolved or even explored in-situ, exoplanets are primarily detected through indirect methods, making study of their atmospheres difficult. However, there are two main methods through which we are able to measure and probe the atmospheres of exoplanets:

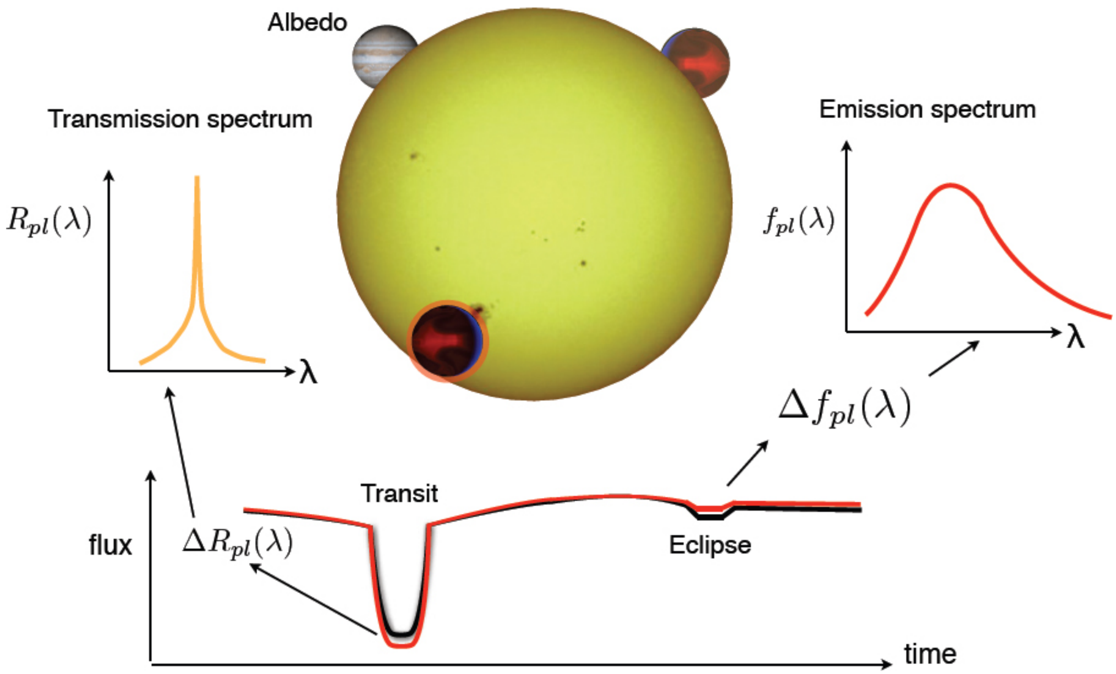

Figure 1.8: An illustration depicting the process of transmission and emission spectroscopy. At the top middle, a star is depicted with an exoplanet in both transit and eclipse. The bottom shows the broadband, wavelength-averaged light curve of the system in black and the same light curve at a specific resonant wavelength of a chemical species present in the planet's atmosphere in red. As the planet transits the star, the atmosphere of the planet is more opaque to the wavelength shown due to the presence of the chemical species in the atmosphere, resulting in a deeper transit depth that translates to an absorption feature in the spectrum (top left). Similarly, as the star eclipses the planet, the portion of the light from the thermal emission or reflectance from the planet to the total brightness of the system is removed, resulting in a measurable decrease. The magnitude of this decrease at different wavelengths depends on the presence of chemical species resonant with that frequency in the planet's atmosphere and can be used to create a spectrum of this thermal and reflected emission (top right). Figure from Sing (2018).

transmission and emission spectroscopy. These processes are described here and illustrated in Figure 1.8.

Transmission spectroscopy exploits the fact that a planet's atmosphere exists on the outer layers of the planet and that its opacity varies as a function of wavelength (e.g. Smith & Hunten, 1990; Eaton, 1993). As the planet transits in front of its host star, light from the star passes through the annulus around the edges of the planet's surface that is comprised of the planet's atmosphere. At different wavelengths of light, different chemical species present in the atmosphere will absorb this light more strongly, causing the opacity of the atmosphere to vary with wavelength and thus make the planet's radius appear larger or smaller. This difference in apparent planet radius, in turn, affects the depth of the planet's transit as a function of wavelength, with deeper transits at wavelengths that are more heavily absorbed and vice versa (Seager & Sasselov, 2000; Brown et al., 2001; Hubbard et al., 2001). It is possible to assemble a "transmission spectrum" from measurements of transit depth across a range of wavelengths to determine which chemical species may be present in the atmosphere of the planet (e.g. Bean et al., 2010; Kreidberg, 2018; Lustig-Yaeger et al., 2023).

While transmission spectroscopy takes advantage of the proportion of light that the planet blocks, emission spectroscopy exploits the fact that the planet itself can often emit its own light or reflect that of the host star (Collier Cameron et al., 1999; Charbonneau et al., 1999b; Stevenson et al., 2014). When observing the system, it is actually the light of the host star plus the light of the planet that is being captured. In most cases, the light of the planet is insignificant compared to that of the star with our current detection capabilities. However, for many of the largest and/or hottest planets, this emitted light is non-negligible and as the planet passes behind the star, this light is blocked and a decrease in the overall brightness of the system is observed, called a "secondary eclipse" (e.g. Deming et al., 2005; Knutson et al., 2007; Agol et al., 2010). The depth of this eclipse is wavelength-dependent and varies based on the proportional contribution of emitted and reflected light as well as the presence of chemical species in the atmosphere of the planet that alter the amount of light emitted or reflected at a specific wavelength. In a manner similar to transmission spectroscopy, it is possible to assemble an "emission spectrum" from measurements of the secondary eclipse depth as a function of wavelength to study the physical processes and chemical composition of the planet's atmosphere (e.g. Stevenson et al., 2010; Arcangeli et al., 2018; Greene et al., 2023).

Using transmission spectroscopy, emission spectroscopy, or both in conjunction provides a wealth of information about a planet's atmosphere, not only in terms of chemical composition, but in terms of structure as well. One of the primary goals of atmospheric observations is to deduce the vertical structure of the atmosphere in terms of the pressure and temperature, referred to as the temperature-pressure (T-P) profile (e.g. Seager & Sasselov, 1998; Barman et al., 2001). The T-P profile is informed by a myriad of factors such as the internal and external heating sources of the planet, the presence of condensed material such as clouds and aerosols at different levels of the T-P profile, and circulation and transport of energy throughout the atmosphere (Madhusudhan, 2019). Investigation of these factors is chiefly accomplished through the process of modeling, where physically motivated models are fit to the observed transmission or emission spectra in order to constrain the presence of specific chemical species or the effects of various physical processes such as the C/O ratio and atmospheric heat redistribution (e.g. Showman et al., 2009; Line et al., 2013). The field of exoplanet atmospheric modeling is vast and active, and although it resides mostly outside the purview of this dissertation it is necessary to discuss due to its interconnectedness with planetary formation, observable properties, planet discovery, and the transit method itself.

The first instance of a successful measurement using these techniques to observe an exoplanet's atmosphere was performed by Charbonneau et al. (2002a). This team used the Hubble Space Telescope to observe transits of the planet HD 209458 b to detect the sodium resonance doublet in the atmosphere of the planet. Since then, over 100 exoplanets have had their atmospheres measured via either transmission or emission spectroscopy using a variety of both ground- and space-based observatories. The earliest observations of exoplanet atmospheres relied largely on broadband photometric filters or low-resolution spectroscopy to make inferences about atmospheric composition (e.g. Charbonneau et al., 2005; Deming et al., 2005; Knutson et al., 2008; Crossfield et al., 2010). Over time, however, the development of new observing facilities and instruments has widened our ability to probe exoplanet atmospheres at greater precision than ever before. With the launch of JWST, it is now possible to push the limits on the size of planets we can confidently expect to observe atmospheres around, but such a boundary has yet to be established (e.g. Tsai et al., 2023; Miles et al., 2023). Much excitement exists about the potential to detect atmospheres on terrestrial planets, but it has yet to be seen whether or not this is possible.

Indeed, JWST has already begun to revolutionize our understanding of exoplanet atmospheres with its superior precision and resolution. JWST is able to regularly achieve ∼20 ppm photometric precision or better on exoplanet targets when observing either in transmission or secondary eclipse (e.g. Fu et al., 2022; Tsai et al., 2023; Bean et al., 2023; JWST Transiting Exoplanet Community Early Release Science Team et al., 2023). Furthermore, JWST has a wide range of observable wavelengths, spanning from 0.6 to 12 μm for its transiting exoplanet spectroscopy modes and encompassing an unprecedented range of spectral features that are observable at a maximum spectral resolution of R $\sim$ 3600 (Gardner et al., 2006, 2023). This is in contrast to a previous workhorse of exoplanet atmospheric observations, the Hubble Space Telescope, which, although delivering a host of groundbreaking atmospheric observations (e.g. Charbonneau et al., 2002a; Vidal-Madjar et al., 2004; Kreidberg et al., 2014), can only reach a photometric precision of 20ppm in some cases under ideal conditions (Line et al., 2016), is limited to wavelengths below 1.7 μm, and typically only reaches spectral resolutions of R $\sim$ 130 for exoplanet atmospheres with its Wide Field Camera 3 instrument (e.g. Edwards et al., 2020).

Because of the improvement from previous facilities, JWST has detected traces of disequilibrium chemistry in the atmosphere of an exoplanet (Tsai et al., 2023), searched for signs of an atmosphere around rocky planets (Greene et al., 2023), observed definitive evidence for carbon dioxide in the atmosphere of WASP-39 b (JWST Transiting Exoplanet Community Early Release Science Team et al., 2023), and more that was not possible with observatories such as Hubble or Spitzer. Identifying interesting exoplanetary targets for observation with JWST is therefore crucial in probing and enriching our understanding of exoplanet atmospheres.

Hot Jupiters continue to play an outsized role in our understanding of exoplanet atmospheres (Dawson & Johnson, 2018; Fortney et al., 2021). Transmission spectroscopy is biased towards planets with transits that have high signal-to-noise ratios. This is due primarily to the sensitivity of transmission spectroscopy to how precisely the depth of a transit can be measured and a potential change in depth distinguished from wavelength to wavelength. Larger transits oftentimes provide higher signal-to-noise ratios, which are in turn caused by larger planets with many transit events that can be combined such as hot Jupiters. Furthermore, emission spectroscopy requires that the planet emit thermal emission or reflect light from the host star at levels detectable with current facilities. Hot Jupiters, as the name implies, are some of the hottest planets currently known and therefore emit large amounts of thermal radiation. Additionally, they also have large solid angles that allow them to reflect much more light from the host star than smaller planets. Thus, the depths of the secondary eclipses from hot Jupiters are much larger than other planets and are more easily detectable. This is all to say that a great deal of our observational knowledge of exoplanet atmospheres stems from our study of hot Jupiters and will continue to do so.

In the chapters that follow, I will employ each of the concepts described in the introduction in the form of original research to probe the hot Jupiter companion rate, hot Jupiter formation, and the capabilities and priorities of exoplanetary atmospheric characterization with JWST going forward. All projects are connected by the thread of vetting and validation of transiting exoplanet candidates but each uses these techniques to examine different core science concepts.

Chapter 2: A Uniform Search for Nearby Planetary Companions to Hot Jupiters in TESS Data Reveals Hot Jupiters are Still Lonely

2.1 Overview

We present the results of a uniform search for additional planets around all stars with confirmed hot Jupiters observed by the Transiting Exoplanet Survey Satellite (TESS) in its Cycle 1 survey of the southern ecliptic hemisphere. Our search comprises 184 total planetary systems with confirmed hot Jupiters with $R_p > 8\mathrm{R}_\oplus$ and orbital period <10 days. The Transit Least Squares (TLS) algorithm was utilized to search for periodic signals that may have been missed by other planet search pipelines. While we recovered 169 of these confirmed hot Jupiters, our search yielded no new statistically-validated planetary candidates in the parameter space searched ($P < 14$ days). A lack of planet candidates nearby hot Jupiters in the TESS data supports results from previous transit searches of each individual system, now down to the photometric precision of TESS. This is consistent with expectations from a high eccentricity migration formation scenario, but additional formation indicators are needed for definitive confirmation. We injected transit signals into the light curves of the hot Jupiter sample to probe the pipeline's sensitivity to the target parameter space, finding a dependence proportional to $R_p^{2.32}P^{-0.88}$ for planets within $0.3 \leq R_p \leq 4$ $\mathrm{R}_\oplus$ and $1 \leq P \leq 14$ days. A statistical analysis accounting for this sensitivity provides a median and 90% confidence interval of $7.3^{+15.2}_{-7.3}\%$ for the rate of hot Jupiters with nearby companions in this target parameter space. This study demonstrates how TESS uniquely enables comprehensive searches for nearby planetary companions to nearly all the known hot Jupiters.

2.2 Introduction

Hot Jupiters (HJs) were among the most surprising class of planets discovered by the first exoplanet surveys. Both the first exoplanet discovered around a main sequence star (Mayor & Queloz, 1995) and the first known transiting exoplanet (Charbonneau et al., 1999a; Henry et al., 1999) were HJs. With radii of $R_p > 8$ $R_\oplus$ and orbital periods of $P < 10$ days (Wang et al., 2015; Winn et al., 2010; Garhart et al., 2020; Huang et al., 2016), HJs are unlike any planet in the Solar System. Many scenarios have been put forth to explain the existence of HJs, such as disk migration (Lin et al., 1996), high-eccentricity migration (HEM; Rasio & Ford, 1996), *in situ* formation (Mayor & Queloz, 1995), and many others; however, none of these formation mechanisms can explain the observed properties of every HJ system (Dawson & Johnson, 2018).

Notably, HJs are often the only detected planet in their systems out to an orbital period of ∼200 days (Knutson et al., 2014; Endl et al., 2014; Steffen et al., 2012). Previous searches for companions to HJs using ground- or space-based data have returned only three known systems (WASP-47, Kepler-730, and TOI-1130) with a HJ and nearby companion planets, out of the many hundreds of currently confirmed HJ systems (Becker et al., 2015; Zhu et al., 2018; Cañas et al., 2019; Huang et al., 2020a). The radii of these companions are 3.58 $R_\oplus$, 1.80 $R_\oplus$, 1.57 $R_\oplus$, and 3.65 $R_\oplus$ for WASP-47 d, WASP-47 e, Kepler-730 c, and TOI-1130 b, respectively, making them all smaller than Neptune. Combined with their short (≤10 days) orbital periods, the transit signals from this class of small planets could be easily missed by planet search pipelines or in noisy data.

The apparent lack of nearby companions in the vast majority of HJ systems supports the idea that HJs form beyond the ice line and migrate inwards via HEM, which would destabilize the orbits of any shorter-period planets in the system (Mustill et al., 2015). This may not be the full story however, since not only are some systems known to have companion planets, but statistical work based on photometric observations suggests that some fraction of HJ systems could have formed via methods other than HEM based on the lack of eccentric proto-HJs observed (Dawson et al., 2014), although it is difficult to rule out HEM entirely for these systems.

This leaves the formation mechanism for many HJs largely a mystery with multiple possibilities for a given individual system. It is possible that the three unique HJs with companion planets named above formed via a different mechanism from many of the other HJs or that they may simply be rare variants of HJs. Comprehensive searches for companion planets to HJs could reveal additional nearby companions to HJs or support previous findings as to the "loneliness" of HJs.

All-sky transit surveys conducted with ground-based telescopes typically do not reach the photometric precision needed to identify shallow transit signals of small, nearby companions to hot Jupiters (Pollacco et al., 2006; Bakos et al., 2004; Pepper et al., 2007). The Kepler and K2 missions led to the discovery of two of three known HJ systems with nearby companion planets (Becker et al., 2015; Cañas et al., 2019), but both missions surveyed only a small fraction of the sky (Borucki et al., 2010; Howell et al., 2014). TESS has enabled nearly-full-sky coverage observations with space-based photometric precision optimized for the discovery of exoplanets around bright stars and presents an excellent opportunity to finally conduct a uniform search for these additional, closely-orbiting planets. In fact, TESS has already begun to demonstrate its usefulness in the search for HJs with companions since the most recent of the systems with companions near an HJ (TOI-1130) was discovered by TESS (Huang et al., 2020a).

Much of the TESS data, including most of the HJ systems, are searched by the TESS Science Processing Operations Center (SPOC) pipeline (Jenkins et al., 2016) and/or the MIT Quicklook Pipeline (QLP; Huang et al., 2020b,c) prior to each data release to the general public. After extracting simple aperture photometric light curves from the calibrated pixel data, the SPOC pipeline identifies and corrects instrumental systematic errors and flags bad data with the Presearch Data Conditioning (PDC) module (Smith et al., 2012; Stumpe et al., 2012, 2014). The SPOC then searches through the resulting PDC_SAP light curves using a wavelet-based, adaptive matched filter algorithm to detect signatures of potential transiting planets (Jenkins, 2002; Jenkins et al., 2010; Jenkins et al., 2017). Limb-darkened transit models are fitted to each of these "threshold crossing events" (Li et al., 2019a), and are then subjected to a suite of diagnostic tests by the Data Validation (DV) module to help adjudicate the planetary nature of each signal (Twicken et al., 2018a). The TESS Science Office reviews the DV reports and diagnostics and promotes and releases compelling cases as TESS Objects of Interest (TOI) for follow up and characterization. Parallel to the SPOC, the QLP extracts its own light curves from the TESS data and searches all targets down to a $Tmag$ of 13.5 using a Box Least Squares (BLS) search algorithm (Guerrero et al., 2021; Huang et al., 2020b,c).

Here, we implement in our pipeline the recently published Transit Least Squares (TLS) algorithm (Hippke & Heller, 2019). Unlike BLS, TLS utilizes a realistic transit model derived from fitting 2,346 known exoplanet light curves that takes into account many of the physical parameters of the system, such as host star mass, radius, and limb darkening parameters. Most notably, TLS provides a 17% increase in detection efficiency for the signals produced by smaller planets over BLS (Hippke & Heller, 2019), although some work has shown that realistic transit shapes only provide as low as a $\sim$3% sensitivity increase if BLS is sufficiently well-sampled (e.g., Jenkins et al., 1996). This higher detection efficiency provides the opportunity to recover a greater proportion of planets with smaller radii than BLS. It also opens up a parameter search space complementary to the QLP and SPOC pipeline and increases the significance of signals considered marginal by BLS. It should also be noted that there has, as of yet, been no direct comparison between TLS and the search conducted by the SPOC pipeline in terms of sensitivity.

In this chapter, we present a uniform search for nearby transiting companions to all confirmed HJs observed in the southern ecliptic hemisphere by TESS during its Cycle 1 observations that is meant to be independent of the SPOC and MIT pipelines. It is well-documented that different search pipelines often have different recovery rates and result in transit detections in different parts of the planetary parameter space (e.g., Kostov et al., 2019a; Kruse et al., 2019). Therefore, we searched for transit signals assuming no prior knowledge of SPOC pipeline or QLP detections with the aim of providing a separate search that utilized different search methods. Our search is uniform for signals with periods $<$ 14 days ($\sim$half the duration of a TESS sector) and potential planets with $R_p \leq 4$ $R_\oplus$ around HJ-bearing systems with host stars of $7.3 \leq Tmag \leq 19.9$ in the TESS Cycle 1 data.

2.3 Target Selection and Data Acquisition

For the purposes of this study and in order to encompass a wide data set, a planet was considered a hot Jupiter if it had an orbital period of $P < 10$ days and a radius of $R_p > 8R_\oplus$

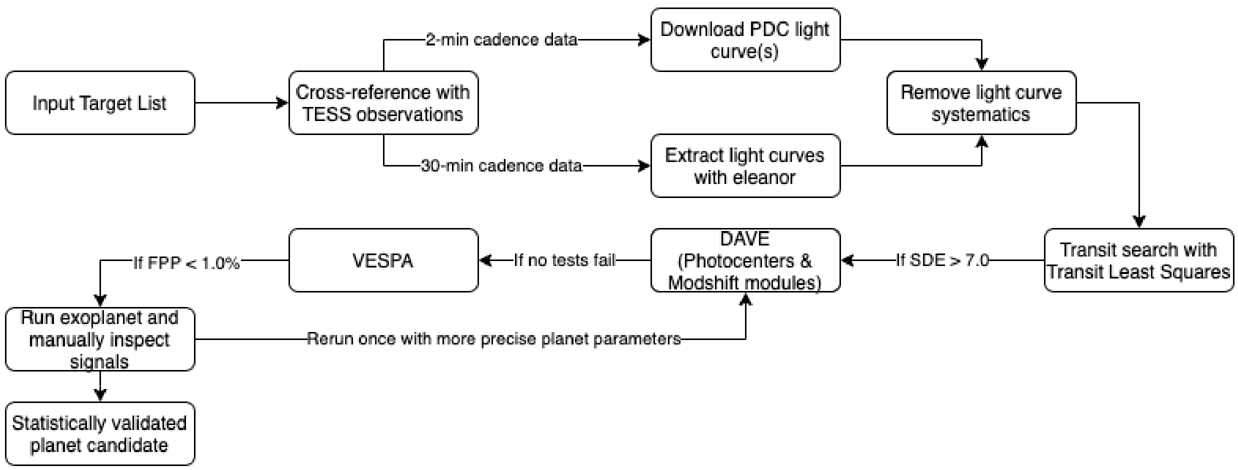

Figure 2.1: A schematic outline of the processing pipeline used in this study. Illustrated are the major steps in the search for additional transit signals in each TESS light curve as well as conditions which, if met, caused a target to advance to the next stage of analysis. In the final loop of the pipeline after the transit search, signals underwent an initial round of vetting and validation with `DAVE` (Discovery and Validation of Exoplanets) and `vespa` before being modeled by `exoplanet`. After the signals were modeled and more precise transit parameters were acquired, the signals were run through `DAVE` and `vespa` once more for a final round of vetting and validation using these more precise parameters.

$\approx 0.71\ R_J$ (Wang et al., 2015; Winn et al., 2010; Garhart et al., 2020; Huang et al., 2016). The NASA Exoplanet Archive[1] was queried on January 6, 2020 with these parameters, resulting in a dataset comprised of 437 confirmed HJs. The R.A., decl., Common Name, Orbital Period, and Radius of each planet were downloaded for use in our analysis pipeline, which is shown in Figure 2.1.

This study was restricted to the first year of the TESS prime mission, which covered the southern ecliptic hemisphere and corresponds to TESS Sectors 1-13. This complements observations being collected currently in the TESS extended mission, where TESS is revisiting the southern ecliptic hemisphere between July 2020 and June 2021. We used the `Tesscut` module of the `astroquery.mast` Python package (Brasseur et al., 2019a) to determine that 183 of the total 437 HJs in the dataset were observed in the first 13 sectors of the TESS prime mission.

[1] https://exoplanetarchive.ipac.caltech.edu/

The TOI-1130 system was added in after the creation of this HJ data set due to the discovery of a nearby companion to the HJ in the system. This brought the total data set up to 184 HJs spanning 0.77 days to 9.62 days in orbital period and 9.41 $R_\oplus$ to 21.41 $R_\oplus$ in radius.

The host stars for these systems have effective temperatures ranging from 3749 K to 9364 K and 97% of the targets fall within the main sequence F, G, and K type stellar classifications. The 5 targets that do not fall within the F, G, and K stellar classifications are all classified as main sequence A type stars. There is only one young star in the sample - DS Tuc. Additional information on each of these targets can be found in the TESS Input Catalog Version 8 (TIC; Stassun et al., 2019a) and all subsequent analysis uses stellar values gathered from the TIC.

In the prime mission, the four TESS cameras captured a Full Frame Image (FFI) of each ∼27-long day observation sector every 30 minutes while ∼200,000 pre-determined targets had a smaller image captured at a cadence of 2 minutes, providing superior data quality for determining transit parameters. All TESS data are calibrated by the SPOC at NASA Ames Research Center. The targets observed at 2-minute cadence also have Pre-search Data Conditioning (PDC) light curves which are systematic error-corrected using an optimal photometric aperture (Smith et al., 2012; Stumpe et al., 2014; Jenkins et al., 2016). These light curves have also been corrected for instrumental signals and contaminating light from nearby stars. There were 126 of the 184 HJs observed in the first 13 sectors of the TESS mission that were observed at 2-minute cadence and had PDC light curves generated in addition to the longer 30-minute cadence data extracted from the TESS FFIs. Both cadences for each target were used in this analysis.

The 2-minute PDC light curves were downloaded from the Mikulski Archive for Space Telescopes (MAST) while the 30-minute light curves were extracted from the TESS FFIs using the `eleanor` Python package, an open-source tool to produce light curves for objects (Feinstein et al., 2019). In short, `eleanor` generates light curves for various combinations of pre-set apertures to determine which aperture minimizes the combined differential photometric precision (CDPP) for data binned to a cadence of 1 hour.

2.4 Transit Search, Vetting, and Validation

After each light curve is extracted, Transit Least Squares (TLS) is used to search for periodic, transit-like signals. Significant signals are then passed through `DAVE` (Discovery and Validation of Exoplanets) for vetting and `vespa` for validation.

2.4.1 Periodic Signal Search

We used the methods presented in Heller et al. (2019) as a guide to prepare the TESS light curves for our planet search and for implementing the TLS algorithm. The light curves were iteratively clipped of outliers $>3\sigma$ and detrended using `lightkurve`'s built-in `flatten` method (Lightkurve Collaboration et al., 2018a) which applies a Savitzky-Golay filter to remove low frequency trends in the light curve by fitting successive sub-sets of adjacent data points with a low-degree polynomial. A window length of $\sim$0.5 days was selected as it compromises between a short enough window to remove stellar variability while still keeping transits intact since the transit duration for all HJs in the sample are $\leq$9 hours. Known HJ transits were masked during this filtering using the orbital periods and transit epoch queried from the MAST. TLS was then run on each processed light curve using the default settings and input stellar parameters from the TIC. We considered a periodic signal to be significant if its signal detection efficiency (SDE) $>$7.0, which corresponds to a false alarm probability (FAP) that the signal is a result of statistical fluctuations of $<1\%$ based on 10000 transit injection simulations performed by Hippke & Heller (2019) using the TLS algorithm on simulated Kepler data with a time baseline of 3 years.

Both the 30-minute cadence and 2-minute cadence light curves were run separately through the transit search as two independent searches of all available data using identical methods for both. Additionally, if a target had more than one sector of data, a transit search was run on each sector individually as well as on the full, combined light curve. This was done to mitigate sector-dependent systematic effects (e.g., impacts of scattered light). For each target, only signals with a period of up to half the total observation length were considered to ensure at least two transits were contained within the observation. Because many targets were only observed for a single TESS sector ($\sim$28 days), we cannot rule out the existence of transiting planets beyond a period of 14 days and are most confident for signals with $P < 14$ days.

Each target was searched with both the TLS "default" shape (more U-shaped) as well as the "grazing" shape (more V-shaped) to maximize the SDE of any possible signals found. TLS was run iteratively for each shape and sector/cadence combination until the signal recovered did not meet the SDE $>$7.0 criterion. For each iteration, previous significant signals were masked out of the light curve for subsequent runs. No more than 2 significant signals in addition to the HJ were found for any target.

For each TLS iteration, key diagnostic parameters were output to a "vetting sheet" which allowed for quick visual vetting of signals to identify any as obvious noise. The vetting sheet contains information such as best-fit orbital parameters, the phase-folded light curve, an odd-even transit comparison, the periodogram, a half-period check, and other items that are useful in determining whether a signal could be real or spurious. See Figure 2.2 for an example of the vetting sheet used.

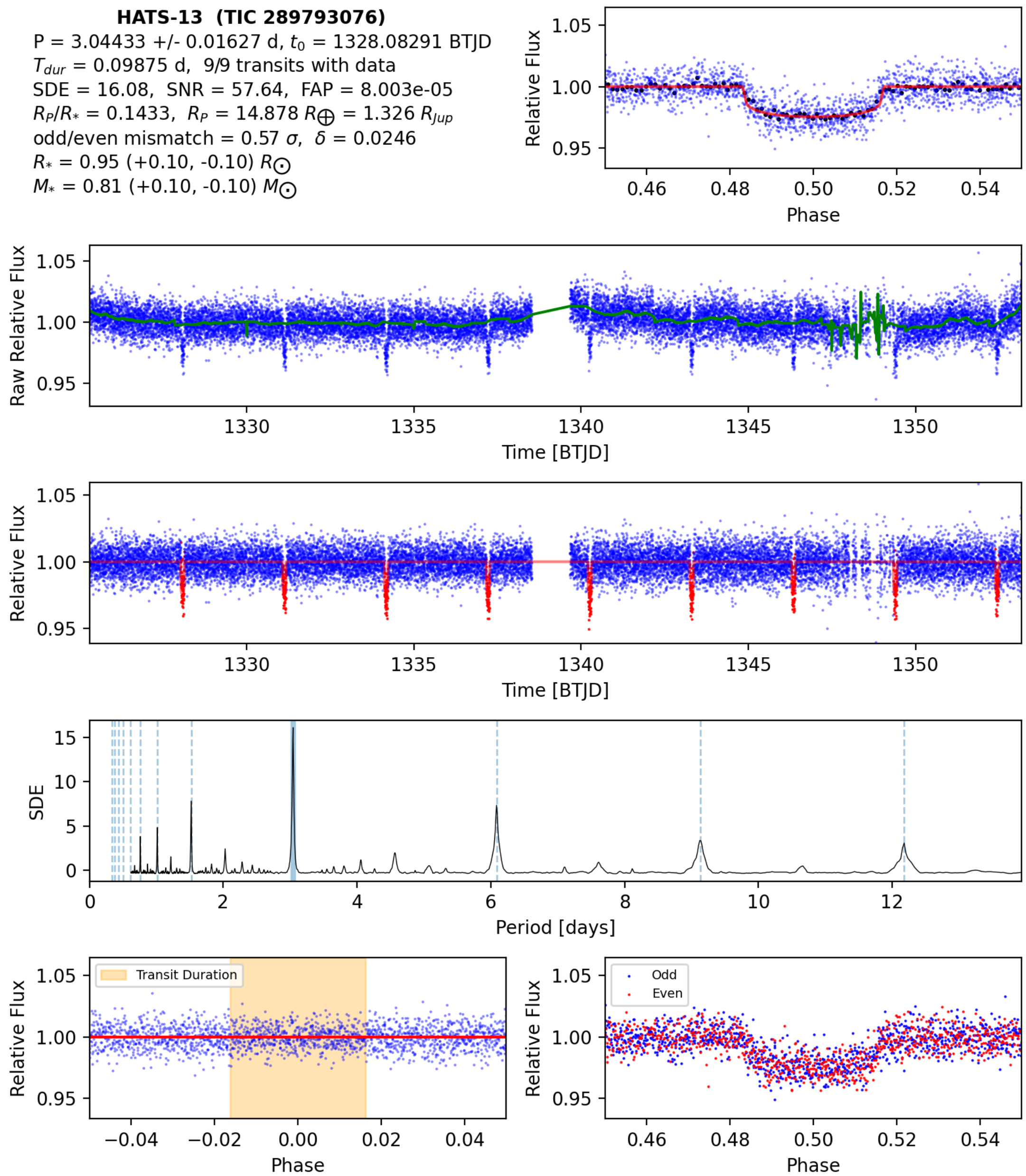

Figure 2.2: Example of the information printed on the vetting sheet for a single TLS iteration (i.e. detection of a single periodic signal). From top to bottom: orbital and system information for the signal, light curve phase-folded to period of the detected signal, raw light curve with removed trend overlaid, flattened light curve with transit model from TLS overlaid and in-transit points highlighted, TLS periodogram with strongest signal and integer multiples highlighted, light curve phase folded viewed a half phase apart from the transit with transit duration highlighted to search for secondary eclipses, odd/even transit comparison.

The TLS search of the 126 HJ systems in the 2-minute cadence data yielded 242 non-HJ signals with SDE $>$ 7.0. There were zero new, non-HJ signals in the 30-minute FFI light curves after initial vetting removed all detected significant signals. This lack of signals in the FFI light curves is likely due to imperfect background subtraction or correction, the sparser sampling of the longer cadence, or instrumental effects that would otherwise be removed by the SPOC pipeline for 2 minute cadence data. It is worth noting that there were some marginal (5.0 $<$ SDE $<$ 7.0) detections of periodic signals in both cadences. Due to the lack of signals recovered in the FFI data, subsequent data, methods, and results will pertain to 2-minute cadence data only. All signals with a SDE $>$ 7.0 were passed along for further vetting and validation as described in the following sections.

To ensure that the search did not miss signals that may have been inadvertently diluted by the flattening procedure, we also searched the PDC and `eleanor`-corrected light curves without flattening as well as the Simple Aperture Photometry (SAP), `eleanor` PSF, and `eleanor` PCA light curves, with and without flattening. We found 2,434 non-HJ significant signals, 43 of which could not be immediately thrown out as noise. Nine of the signals that could not be ruled out as noise were also found in the search of the flattened PDC light curves. The remaining 34 signals were heavily scrutinized prior to any further analysis and all of them were rejected as potential candidates on the basis of transits overlapping with unsubtracted in-transit points from the HJs, unrealistic planet parameters, or $>$50$\%$ of transit events on the edge of the observation window or in observation gaps.

Nine of the 126 HJs with 2 minute cadence data were not recovered by the TLS search with a SDE $>$ 7.0. Of these 9 HJs that were not recovered, 7 HJs were around host stars with $Tmag$ $\gtrsim$ 13.1, 1 HJ was located near the galactic disk with a high degree of crowding, and 1 HJ orbits a host star with extreme stellar variability. Six of the 58 HJs with only 30 minute FFI cadence were not recovered. Four of these HJs were around host stars with $Tmag \gtrsim 13.8$, 1 HJ was around a host star with large stellar variability, and 1 HJ was located near the galactic plane and suffered from a high degree of crowding.

2.4.2 `DAVE` Analysis

The `DAVE` tool is an open-source Python package that wraps many common exoplanet vetting tools (Coughlin et al., 2014a, e.g. *Robovetter*) into one streamlined pipeline. This software has been extensively used to vet planet candidates from the *Kepler* mission (Hedges et al., 2019; Kostov et al., 2019a; Kostov et al., 2019b) and the TESS mission (Crossfield et al., 2019; Kostov et al., 2019b). `DAVE` performs light-curve based vetting tests (odd-even transit comparison, a search for transit-like features due to light curve modulations, secondary eclipse checks) and image-based vetting tests (photocenter shift during transit).

Each significant periodic signal recovered with TLS was passed through `DAVE` and those that failed any of its modules were flagged for further inspection and removed from the analysis pipeline. If `DAVE` analysis flagged a signal in error, the signal was returned to the general pool of vetted signals. In total, 50 out of the initial 242 recovered signals passed DAVE vetting, although not all DAVE modules were able to run successfully for each signal. This is because in many cases, the transits of potential new signals overlapped with or were too close to those of the HJs, causing `DAVE` to run each module for the HJ multiple times instead of once for each of the signals in the light curve. This issue mostly affected the light-curve vetting tests and the image-based centroid vetting tests ran successfully for the majority of the target systems.

2.4.3 VESPA Validation

To complement DAVE analysis, we used vespa (Morton, 2012a, 2015a) to calculate the false-positive probabilities of each signal. When provided stellar parameters, celestial coordinates, and orbital parameters, this package compares transit-like signals to a variety of astrophysical false-positive scenarios including an unblended eclipsing binary (EB), a blended background EB, a hierarchical companion EB, and the 'double-period' scenarios for each of these EB possibilities. All stellar parameters used in the vespa analysis were queried from the TIC for each individual target system (Stassun et al., 2019a). Orbital and planetary parameters from the TLS search output were used as inputs for the first round of vespa validation for each signal. If signals were successfully validated by vespa and proceeded to the exoplanet modeling step outlined in Figure 2.1, the orbital and planetary parameters from this modeling were used for a secondary round of vespa validation. The light curves used in the TLS search outlined in Section 2.4.1 were folded according to the best-fit orbital period and mid-transit time (t0). These phase-folded light curves were used in the vespa analysis, oftentimes binned to reduce the scatter in the light curve and prevent an invalid fit of the transit shape or unreasonable posterior values.

A vespa input parameter of particular sensitivity is the maximum aperture radius (*maxrad*) interior to which the signal must originate. This parameter strongly affects the likelihoods of the background eclipsing binary scenarios that vespa considers and is very dependent on sky position and the instrument used. We queried the *Gaia* DR2 catalog within the SPOC pipeline extraction aperture to identify nearby background sources that are within 6 magnitudes of the target in the G_{RP} band (630 - 1050 nm Brown et al., 2018). This band was chosen for its large overlap with the TESS band (600 - 1000 nm Vanderspek et al., 2018). The *maxrad* parameter was then set to the outermost background source meeting this criterion within the extraction aperture. If no background sources within the extraction aperture met this criterion, the *maxrad* parameter was conservatively set to 2" to account for possible target position offset and the resolution of *Gaia*. We note that, given the high resolution of *Gaia*, this *maxrad* parameter could be reduced to an even lower value in more thorough treatments of individual sources.

The maximum depth for a possible secondary eclipse (`vespa`'s *secthresh* parameter) was used from the secondary eclipse depth output from `DAVE` if *modshift* successfully ran a given target. Otherwise, a quick TLS search was performed for secondary transit-like features and that depth was used for the *secthresh* parameter.

This `vespa` routine was repeated up to 25 times for each signal binned with values between 1 and 25 data points per bin. This was done to mitigate any variations between individual `vespa` simulations and because oftentimes `vespa` was unable to correctly fit a transit shape to the light curve or there was an error with calculating the posterior distributions of one or more astrophysical scenarios. The `vespa` simulation with the lowest binning value that did not produce an error was kept for each signal.

If the false positive probability (FPP) from the kept `vespa` simulation $<1\%$, we considered the signal to be statistically validated and the transit signal classified as a bona fide planet candidate. These FPP values calculated are likely upper limits since `vespa` analysis does not account for any likelihood increase due to a multiplicity boost from the confirmed HJ in each system. A multiplicity boost is the decrease in the FPP that a planet candidate gets from having other confirmed planets in the system since statistical work has demonstrated that systems containing multiple transit signals are more likely to be true planets than systems with only a single periodic signal (Lissauer et al., 2012a). The exact multiplicity boost has not yet been calculated for TESS, therefore we elected to keep signals with a FPP value $<10\%$ in the analysis as possible "marginal" signals in case any of them could pass below the 1% threshold when the multiplicity boost is calculated[2]. This could very well be the case if the TESS multiplicity boost is at all similar to that calculated for *Kepler* in Lissauer et al. (2012a).

Of the 50 signals that passed DAVE vetting, 14 produced an FPP value of $<10\%$ for at least one of its `vespa` iterations with 3 of these 14 signals producing an FPP value $<1\%$. These 14 signals were passed to `exoplanet` for more detailed modeling.

It is worth noting that `vespa` only tests against the six astrophysical false positive scenarios and does not take into account potential contamination from instrumental effects. While the instrumental false alarm rate for TESS has yet to be calculated, the TESS detectors exhibit fewer electronic noise artifacts than *Kepler*[3], which this software was developed on and where the FPP $< 1\%$ validation threshold was established (Coughlin et al., 2014a; Krishnamurthy et al., 2019; Vanderspek et al., 2018). Therefore, we believe it is safe to assume that the 1% FPP threshold still holds here for TESS. However, as we discuss in Section 2.5, the 14 signals that we identified as passing the `vespa` validation were subsequently determined to be instrumental effects after detailed light curve modeling and further manual inspection. Since `vespa` only tests for astrophysical false positives, these instrumental effects would not necessarily have been caught by `vespa` as non-planetary signals.

[2]We note that the multiplicity boost for TESS planets in general may be different from that of HJ systems specifically since there is strong evidence that HJ systems exhibit different planet clustering behavior than other planetary systems. Such a calculation is outside the scope of this work and marginal signals are included in this study to be as thorough as possible in light of an unknown multiplicity boost.

[3]`https://archive.stsci.edu/kepler/manuals/KSCI-19033-001.pdf` and `https://archive.stsci.edu/files/live/sites/mast/files/home/missions-and-data/active-missions/tess/_documents/TESS_Instrument_Handbook_v0.1.pdf`

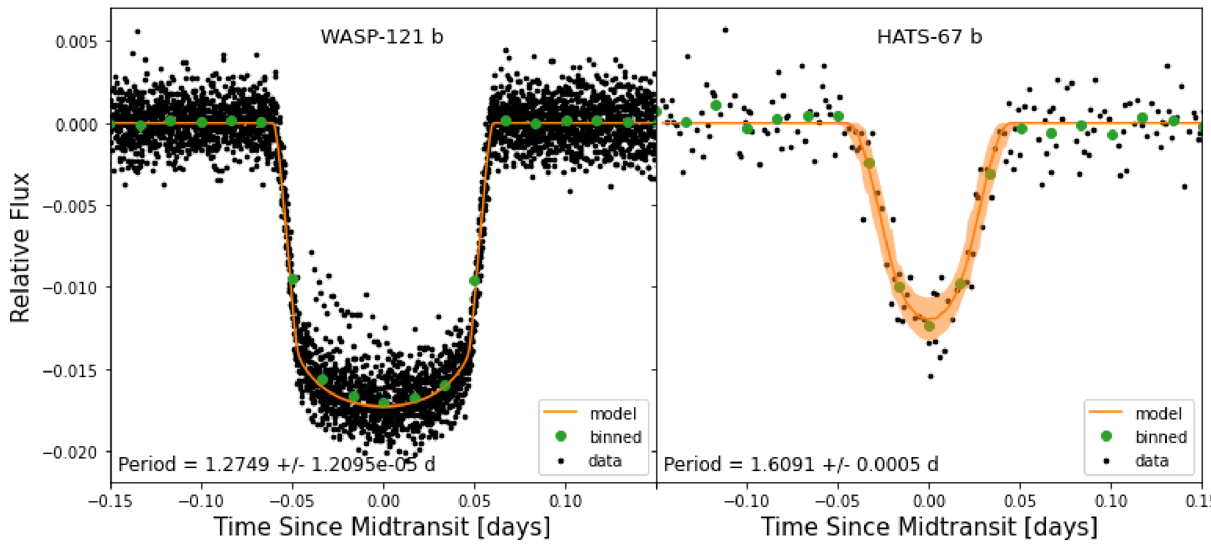

Figure 2.3: Examples of best-fit models with `exoplanet` for 2 minute cadence data (left, WASP-121 b) and 30 minute cadence data (right, HATS-67 b). Green points correspond to binning such that 19 points appear within the bounds of each axis. The transit model based on best-fit sampled posterior values is plotted in orange with light orange shading to represent the extent of 1σ errors.

2.5 Determination of Precise Planet Parameters

TLS uses a period and transit duration search grid calculated upon initialization based on stellar properties and light curve length that is used to find periodic transit-like signals in a light curve (Hippke & Heller, 2019). This grid can be oversampled for greater precision in period and duration of a transit-like feature, however this can quickly become computationally expensive and may still not produce the most precise orbital parameters. To remedy this, we used the software `exoplanet` (Foreman-Mackey et al., 2019) on only the periodic signals that passed through `DAVE` and `vespa`. `exoplanet` is a toolkit for probabilistic modeling of transit and radial velocity observations of exoplanets using PyMC3. This is a powerful and flexible program that can be used to build high-performance transit models and then sample them through Markov Chain Monte Carlo (MCMC) simulations to provide precise transit and orbital parameters.

Table 2.1: Table listing the number of new signals that passed each stage of the pipeline.

Pipeline Stage	# of Signals Passed
TLS Search	242
`DAVE` Vetting	50
`vespa` Validation	14
`exoplanet` Modeling	0

Examples of `exoplanet`-sampled HJ transits from our analysis is shown in Figure 2.3 with both 2 minute and 30 minute cadence data. `exoplanet` was run to determine planet parameters for each of the 169 recovered HJs and the 14 new signals statistically validated to a FPP $<10\%$ by `vespa`. Through these detailed light curve model fits, we concluded that none of these signals arise from planets. Instead, they are noise, systematics, or integer multiples of improperly-subtracted HJ transits based on the best-fit transit parameters. These signals likely passed through the initial light curve detrending since they were variable on the same timescale as a typical transit duration and were sector- or CCD-specific features in the TESS data that were missed by the SPOC pipeline's detrending and our subsequent detrending with `lightkurve`. Furthermore, TLS may not have accurately determined the duration of the HJ transits in the system due to its more sloping ingress and egress model rather than the sharp edges of BLS, causing the wings of the transit to be left behind after HJ transit subtraction.

Although no new promising planet candidates were found, we use the `exoplanet` models for these systems to provide a uniform set of updated orbital and planet parameters derived from TESS data for each of the HJs. These values can be found in a machine-readable file as part of the online version of this work (Hord et al., 2021).

2.6 Companion Rate Estimation

Although no new planet candidates were discovered through our search, it is still possible to place an upper limit on the rate of companion planets per HJ in the sample of systems used here. To do this, we need to know the efficiency at which our pipeline can recover transit signals so that we can correct our non-detection of additional companion planets for completeness of the search. In order to determine this efficiency, we performed a series of transit injections into light curves with known HJs that were then run through our implementation of TLS to probe the recovery rate of this method within different parameter spaces. For our detection efficiency calculation and subsequent estimation of the rate of companion planets per HJ, we only consider the 168 HJs that we are able to recover with our search pipeline after removing TOI-1130 since it was added after the target list was generated and would bias the statistical analysis. Furthermore, transit injection and successful recovery serves as an independent check and validation of our transit search algorithm implementation.

To perform these simulations, we used the `Batman` Python package (Kreidberg, 2015) to generate artificial transits that were injected directly into the TESS PDC light curves of all 117 HJs that were recovered in the 2 minute cadence TESS data. The 9 PDC light curves in which the HJ was not recovered were not included in these simulations. By injecting simulated transits into real TESS data, we were able to obtain more realistic transit recovery scenarios than if synthetic light curves were used.

We simulated $\sim$57,000 planet transits with randomly and uniformly sampled orbital period, planet radius, orbital inclination (i), injected into one of the 117 HJ light curves, randomly selected for each iteration. These HJ light curves orbit around host stars with 7.3 $\leq$ TESS mag-

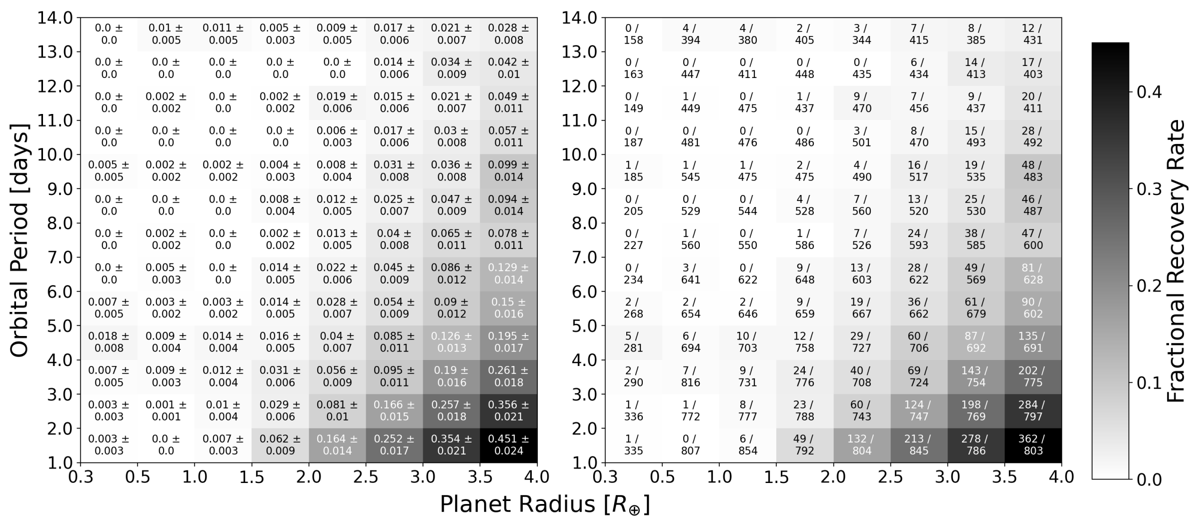

Figure 2.4: Grids displaying the recovery rates for each bin in the entire period and radius space simulated. The color in each cell denotes the fraction of injected planets recovered, averaged over all host star magnitudes and simulated inclinations in that slice of period-radius parameter space. Values of <5e-4 were rounded to 0 for clarity. Simulated transiting planets of all S/N are included. See Section 2.6 for further details. *Left:* Values in the cells denote the recovery rates of that slice of parameter space. Errors represent the square root of the number of successfully recovered injections divided by the total number of injections in each cell. *Right:* Values in the cells denote the number of recovered injections over the total number of injections in each slice of parameter space.

nitudes ($Tmag$) $\leq$ 17.8. The quadratic limb-darkening parameters and semi-major axis for each simulated planet were derived from the stellar parameters of the host star of the light curve that each transit was injected into. The orbital period was sampled between 1 day and 14 days to ensure that there were at least 2 transits in each ∼27-day TESS sector. The planetary radius was sampled between 0.3 $R_\oplus$ and 4 $R_\oplus$, the radius of one of the smallest exoplanets discovered (Barclay et al., 2013) and slightly larger than the largest HJ companion discovered (TOI-1130 b), respectively. The inclination was sampled from within the 1σ uncertainties of the host HJ's inclination so that the planets could be considered coplanar. A circular orbit was assumed. Each of the simulations was run through our implementation of TLS using the same procedure outlined in 2.4.1 and compared with the simulated parameters. Any simulation where the strongest

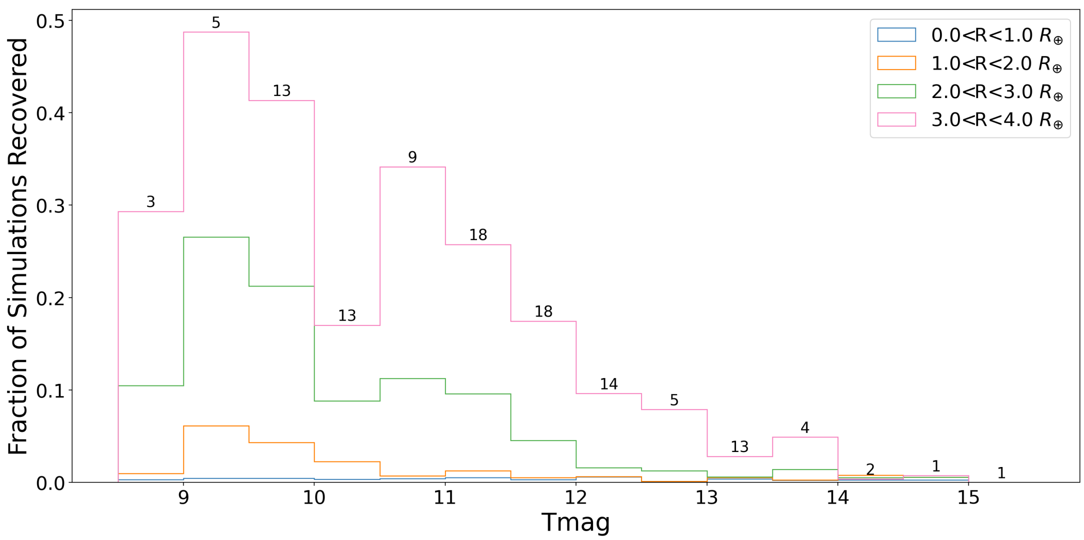

Figure 2.5: A histogram illustrating the recovery rates of simulated planets of different radii as it depends on the $Tmag$ of the host star. Each line represents a different slice of the planetary radii simulated, binned into corresponding bins in magnitude space of width $Tmag$=0.5. The histogram values are averaged over all inclinations and periods and contain signals of all S/N. The numbers above the highest histogram value in each bin represent the number of HJ light curves that were injected into in that $Tmag$ bin. This is included to illustrate how variability, artifacts, or quirks of individual light curves in $Tmag$ bins with few HJ light curves can affect the overall recovery rates. These numbers are also included to highlight the aim of these simulations to probe the sensitivity of this search in this particular data set rather than HJ light curves as a whole. The geometric transit probability is not applied here in order to more clearly illustrate the effect of $Tmag$ and individual stars on the detection efficiency. See Section 2.6 for further explanation.

non-HJ signal with a SDE $>$7.0 matched the simulated period within its 1σ errors was considered "recovered."

It is important to note that only combinations of parameters that produced transits of nonzero depth were considered. All of the simulations that were included in further analysis exhibited a transit of nonzero depth and none of the recovery rates include non-transiting cases.

Figure 2.4 displays the recovery rates for each segment of the orbital period and planet radius parameter space simulated across all inclinations and host star Tmag values. The highest recovery rate of $\sim$45.1$\%$ corresponds to the largest planets that transit the most frequently, with that of Earth-sized planets reaching no higher than 1.4$\%$. This sensitivity grid, in essence, represents the total fraction of planets within the R_p and P space that our pipeline was able to recover, regardless of signal strength.

To quantify the dependence of the recovery rate on P and R_p, we fit a double power law of the form $kP^{-\alpha}R_p^{-\beta}$ where k is a constant, and α and β are the power law indices of P and R_p. Using the `scipy.optimize` package to fit the function to the recovery rate grid, we found best fit values of α=0.88 $\pm$ 0.03 and β=-2.32 $\pm$ 0.12, or a $P^{-0.88}R_p^{2.32}$ dependence for the recovery rates presented in Figure 2.4.

The recovery rates are not uniform within each R_p and P cell as there is some dependence on parameters other than R_p and P. TESS magnitude of the host star, in particular, strongly affects the recovery rate of the simulated planet transits. Figure 2.5 is included to illustrate how the recovery rates of various planet radii ranges vary in the host star TESS magnitude parameter space. Generally, brighter host stars correspond to higher recovery rates, although some TESS magnitude bins do not exhibit this due to the artifacts or mild stellar variability of individual light curves included within them that initial light curve flattening does not remove. Figure 2.5

includes the number of HJ light curves contained in each Tmag bin to illustrate how individual effects influenced Tmag bins with fewer light curves.

Comparing these recovery rates to that of the original TLS validation paper (Hippke & Heller, 2019), we observe lower recovery rates. However, this is likely due to a combination of factors. TLS was originally designed and implemented for use with *Kepler* data, which typically have greater photometric precision and longer time baselines than TESS data (Borucki et al., 2010; Ricker, 2015), arguably making it easier to recover small planets in *Kepler* data since these factors cause small signals to have higher S/N than in TESS data. Additionally, TLS was validated on 1 $R_{\oplus}$ planet signals injected into artificial light curves with purely Gaussian noise and long baselines of 3 years. Therefore, it is logical that the shorter observation baseline of each TESS sector combined with non-Gaussian noise terms and lower photometric precision would produce recovery rates lower than the 93$\%$ stated by Hippke & Heller (2019). Furthermore, as described in Kruse et al. (2019), mutual recovery rates of planet candidates of $\sim$60$\%$ are not uncommon from survey to survey. This again highlights the importance of multiple, independent searches of the same data set using separate methods so as to maximize the number of planet discoveries.

In order to estimate the rate of nearby companions to HJs, we addressed the problem through a Bayesian binomial framework following the methodology described in Appendix A of Huang et al. (2016). The likelihood of observing N_{obs} companions to HJs from N_{tot} systems with a multiplicity rate of r_m can be expressed as B($N_{obs}|r_m$, N_{tot}). In our case, N_{obs} is observable, r_m is constrained given the data, and N_{tot} is the number of HJs recovered in our sample (N_{HJ}) multiplied by a detection efficiency averaged across the entire parameter space ($\langle d_{eff}\rangle$) to correct for possible missed transiting planets according to Equation 5 in Zhu & Dong (2021).

We can constrain r_m by sampling the posterior space, given by the likelihood described above multiplied by some prior function for r_m. In this case, we adopt a uniform prior between 0 and 1 for the rate of nearby companions to HJs (r_m).

We perform a MCMC simulation using emcee (Foreman-Mackey et al., 2013) to sample this posterior space and constrain the rate of HJ multiplicity. For our MCMC model, we assumed that the companions transit and are coplanar with the HJ in the system (within the uncertainties of the HJ's inclination). For potential companions in the parameter space sampled here of 0.3$\leq R_p \leq$4 R$_\oplus$ and 1$\leq P \leq$14 days, we calculate a $\langle d_{eff} \rangle$ of 4.8$\%$ and we obtain a HJ multiplicity rate of $7.3^{+15.2}_{-7.3}\%$. If we shrink this potential companion parameter space to exclude companions of R_p <2.0 R$_\oplus$ as in Huang et al. (2016), we obtain a HJ multiplicity rate of $4.2^{+9.1}_{-4.2}\%$. These values represent the median of the distribution and the 90$\%$ confidence interval. Table 2.2 summarizes the rate of nearby companions for these two slices of the companion parameter space at various confidence intervals.

The values reported here are consistent with the values reported by both Huang et al. (2016) and Zhu & Dong (2021). Both of these studies utilized the *Kepler* sample in their estimation of companion rate, which has a higher detection efficiency due to its greater photometric precision, but a smaller HJ sample size than the TESS HJ sample used in this study.

We note that the TOI-1130 system was not included in this part of the analysis. Including it would bias the result since the system was only added into the search sample after the original list had been generated on the basis that TOI-1130 is contained within the TESS field of view and exhibited the type of system structure that this study was searching for. For comparison's sake, the same statistical estimation of HJ companion rate was performed including TOI-1130, resulting in a rate of $17.7^{+18.6}_{-11.7}\%$ across the whole parameter space probed and a rate of $10.3^{+12.0}_{-6.9}\%$ when

Table 2.2: The rate of companions per HJ at various confidence intervals for both the full range of potential companions with 0.3≤R_p≤4 $R_\oplus$ and the narrower range 2.0≤R_p≤4 $R_\oplus$.

Percentile	0.3≤R_p≤4 $R_\oplus$	2.0≤R_p≤4 $R_\oplus$
50%	7.2%	4.2%
68%	11.8%	6.8%
90%	22.0%	13.3%
95%	27.8%	17.1%
99%	39.4%	25.0%

excluding companions with R_p <2.0 $R_\oplus$. The upper and lower limits on these values represent the 90% and 10% confidence intervals, respectively.

2.7 Discussion

2.7.1 Comparison to Other Searches

Both the SPOC pipeline (Jenkins et al., 2016) and the MIT Quicklook Pipeline (QLP Huang et al., 2020b,c) searched each of the HJ systems included in this study with their independent pipelines and also returned no new planet candidates in systems with confirmed HJs. Furthermore, smaller scale studies on subsets of the HJ population - such as that of Steffen et al. (2012) and Maciejewski (2020) - also find no nearby companions and sometimes complement the photometric analysis with radial velocity data. Our independent search of the HJ population in the southern ecliptic hemisphere provides compelling support for a lack of planetary companions nearby these HJs down to the photometric precision of TESS. Each pipeline searched using different search algorithms, ranges of orbital period, and light curve processing, thus maximizing the parameter space within which new signals can be detected in these target systems.

The QLP did discover an entirely new HJ system in the Cycle 1 TESS FFIs. This system - TOI-1130 - does indeed contain a HJ along with an inner companion (Huang et al., 2020a). This system was not originally included in our study since it was not confirmed prior to the initial target list but was included in subsequent companion searches in this study. However, TOI-1130 was not included in our statistical analysis of the HJ population since it was not discovered prior to the start of this study and its addition would bias the results. The pipeline presented here was able to recover both the HJ signal and the companion planet signal of this new TOI-1130 without need for any additional systematics or noise correction, despite the fact that no new significant signals were recovered from FFI data by our pipeline otherwise.

The agreement of the results from the QLP and SPOC pipeline with that presented here, although not necessarily expected, serves as an excellent check of our pipeline and the validity of the TOI-1130 system, especially since the other two systems harboring HJs with nearby companions (WASP-47 and Kepler-730) were not contained within the Cycle 1 TESS data. Additionally, since there has as of yet been no direct comparison between the sensitivity of TLS and the SPOC search pipeline, these results can serve as an indication that the sensitivities of this TLS search, the SPOC pipeline, and the QLP are comparable. This is of particular interest given the results from the validation of TLS suggesting that TLS has a $\sim$17% higher detection efficiency than BLS, which is used by the QLP (Hippke & Heller, 2019).

Although this study probes a slightly different parameter space of nearby companions to hot Jupiters than Huang et al. (2016), the calculated values for the rate of companions to HJs are consistent with Huang et al. (2016) who reported $1.1^{+13.3}_{-1.1}\%$ compared to $7.3^{+15.2}_{-7.3}\%$ calculated by this study. The larger period and radius space probed by this study more closely matches the parameter space studied by Zhu & Dong (2021), which reports a value of $\sim$2% with a 95%

confidence interval of 9.7% for the rate of companions nearby HJs. This is also consistent with our result. Both of these previous studies utilized the *Kepler* sample of HJs in their determination of the rate of companions nearby HJs, which has greater photometric precision - and therefore higher detection efficiencies - but a smaller sample size of HJs. Our study marks the first uniform calculation of this rate with the TESS HJ sample.

2.7.2 Implications for HJ Formation

The lack of any additional new validated planets in the HJ systems we searched supports previous results that indicate a general lack of planets in nearby orbits to HJs (Steffen et al., 2012). The only exceptions to this trend are WASP-47 d, WASP-47 e, Kepler-730 c, and the recently-discovered TOI-1130 b (Becker et al., 2015; Cañas et al., 2019; Huang et al., 2020a). This lack of nearby planets to HJs is in stark contrast to the "warm Jupiters" (WJs), a class of planet similar to HJs, but with an orbital period between 10 and 200 days. Approximately 50% of WJs have nearby companion planets compared to the $1.1^{+13.3}_{-1.1}\%$ of HJs with companions as reported by Huang et al. (2016) or the rate of $7.3^{+15.2}_{-7.3}\%$ reported here, despite the orbital period cutoff distinguishing the two classes being somewhat arbitrary. In fact, as discussed in Huang et al. (2020a), the period distribution of giant planets with nearby companions appears continuous from the shortest period of the three aforementioned HJs (WASP-47 b) through the WJ periods. This could suggest that these handful of HJs with companions formed in a similar manner to the slightly cooler WJs while the rest of the HJs formed via a separate pathway.

Some formation scenarios make specific predictions for the occurrence of nearby companion planets. In the case of formation through high eccentricity migration (HEM) where the giant planet arrives at its current position via gravitational scattering of other bodies in the system, the likelihood that nearby planets exist is low due to the disruptive nature of the planet migration (Mustill et al., 2015). In the case of a disk migration where the entire protoplanetary disk migrates inward, companion planets would be more likely to survive but would also likely exhibit orbital resonances with one another (Lee & Peale, 2002; Raymond et al., 2006).

However, while a lack of nearby companion planets cannot definitively determine the pathway through which each system formed, this characteristic may aid in classifying portions of the HJ population when combined with additional evidence. Some formation scenarios that challenge current HJ formation theories could benefit from knowing that HJs are lonely with a greater amount of certainty. For instance, there are possible situations where companion planets are retained despite HEM (Fogg & Nelson, 2007) or situations where HEM cannot explain the observed dynamics in a handful of known HJs (Dawson et al., 2014). Constraining the presence of nearby companions to HJs may help in determining the dynamical histories of some of these scenarios that complicate our theories on HJ formation.

Although these systems are proving to be quite rare, it is important to continue to search for HJ systems with closely-orbiting companions so that comparisons can be drawn between this unique subset of systems and the wider sample of HJs/WJs. Additional discoveries of HJ systems with nearby companions would contribute to a better understanding of how these systems formed and if the mechanism differs from other portions of the HJ/WJ population. Furthermore, a scaled-up statistical analysis including the larger TESS field and all three systems with known nearby companions to HJs would provide a companion rate per HJ that is much more representative of the HJ population as a whole since the rate reported here only considers the HJs of the TESS southern ecliptic hemisphere in TESS Cycle 1.

2.8 Summary

In this chapter, we present the results of an independent, uniform search for companions to HJs in TESS southern ecliptic hemisphere data (Sectors 1-13). Our investigation and results are summarized here:

- We searched the TESS light curves of 184 systems with HJs of $R_p > 8R_\oplus$ using Transit Least Squares with both the default and grazing transit shapes.
- New signals recovered by the Transit Least Squares search with a signal detection efficiency > 7.0 were passed through `DAVE` and `vespa` for vetting and validation.
- There were zero new signals with $P < 14$ days statistically validated as planet candidates to a false positive probability $< 1\%$ in either the 2-minute cadence SPOC PDC light curves or the 30-minute TESS FFI light curves. We cannot rule out the existence of transiting companions with $P > 14$ days, however.
- We probed the detectable parameter space of potential small planet signals using our pipeline, finding a dependence of recovery rates proportional to $R_p^{2.32}P^{-0.88}$. We found a strong dependence on magnitude and activity of the host star as well for all recovery rates.
- We performed a statistical analysis to estimate a rate of $7.3^{+15.2}_{-7.3}\%$ planets within $0.3 \leq R_p \leq 4$ $R_\oplus$ and $1 \leq P \leq 14$ days per HJ.
- A lack of new companion planets to HJs down to the photometric precision of TESS provides further evidence for the "loneliness" of HJs out to P=14 days and HEM as a plausible formation mechanism for a large portion of the HJ population. This is in contrast to warm

Jupiters where nearby companions are common, suggesting possible different formation mechanisms for the two populations.

- These search results suggest that the sensitivities of the SPOC search pipeline, MIT's QLP, and this TLS pipeline are comparable in the search for small companions to HJs.

This work constitutes a first step in comprehensively searching every HJ observed by TESS. Similar studies of the HJ systems observed by TESS in its survey of the northern ecliptic hemisphere will be beneficial for further exploring potential HJ formation mechanisms. Furthermore, TESS has recently started its extended mission where it is effectively repeating its survey of the southern and northern ecliptic hemispheres and will also survey part of the ecliptic plane for the first time.

As an additional component of this work, we provide updated transit ephemerides for each HJ with TESS 2-minute Cycle 1 data available in the online version of Hord et al. (2021). The majority of both the orbital period and the planetary radius value agree within 1σ errors with published values. For a subset of these HJs, the planetary radius is better constrained with smaller uncertainties than published values. The eccentricity values are calculated based on stellar density according to the prescription in Dawson & Johnson (2012) and are generally slightly higher than in the literature. This parameter is calculated and not directly sampled, so is subject to larger uncertainty than a sampled parameter. These can aid in follow-up observations and studies of the HJs themselves, since in the absence of planetary companions, further study of the HJs in these systems becomes even more important in constraining their formation processes.

Chapter 3: The Discovery of a Planetary Companion Interior to Hot Jupiter WASP-132 b

3.1 Overview

Hot Jupiters are generally observed to lack close planetary companions, a trend that has been interpreted as evidence for high-eccentricity migration. We present the discovery and validation of WASP-132 c (TOI-822.02), a 1.85 $\pm$ 0.10 $R_\oplus$ planet on a 1.01 day orbit interior to the hot Jupiter WASP-132 b. Transiting Exoplanet Survey Satellite (TESS) and ground-based follow-up observations, in conjunction with vetting and validation analysis, enable us to rule out common astrophysical false positives and validate the observed transit signal produced by WASP-132 c as a planet. Running the validation tools `vespa` and `TRICERATOPS` on this signal yield false positive probabilities of 9.02×10^{-5} and 0.0107, respectively. Analysis of archival CORALIE radial velocity data leads to a 3σ upper limit of 28.23 ms^{-1} on the amplitude of any 1.01-day signal, corresponding to a 3σ upper mass limit of 37.35 $M_\oplus$. Dynamical simulations reveal that the system is stable within the 3σ uncertainties on planetary and orbital parameters for timescales of $\sim$100 Myr. The existence of a planetary companion near the hot Jupiter WASP-132 b makes the giant planet's formation and evolution via high-eccentricity migration highly unlikely. Being one of just a handful of nearby planetary companions to hot Jupiters, WASP-132 c carries with it significant implications for the formation of the system and hot Jupiters as a population.

3.2 Introduction

Ever since the Nobel Prize-winning discovery of the first exoplanet around a Sun-like star (Mayor & Queloz, 1995), hot Jupiters have represented one of the greatest enigmas of exoplanet science. With radii $R_{\rm p} > 8$ $R_{\oplus}$ and orbital periods $P < 10$ days (Winn et al., 2010; Wang et al., 2015; Garhart et al., 2020), hot Jupiters represent a class of planets with no analogue in our solar system. Traditional theories on planet formation are insufficient to explain the existence of giant gaseous planets so close to a host star (Lin et al., 1996). Therefore, new formation scenarios have been put forth (e.g. disk migration, planet-planet scattering, secular migration) to explain the existence of hot Jupiters, most of which involve an inward migration after initially forming beyond the ice line (e.g., Lin et al. 1996; Rasio & Ford 1996). However, none of these mechanisms alone can satisfy all observable constraints, leaving the primary pathways of hot Jupiter formation largely still uncertain (Dawson et al., 2014; Dawson & Johnson, 2018).

One clue that may help distinguish between different formation pathways is that hot Jupiters are predominantly "lonely", meaning they are the only planet in their system within a factor of 2 or 3 in orbital distance (e.g. Steffen et al., 2012; Knutson et al., 2014; Endl et al., 2014; Hord et al., 2021), although they may have more distant companions, particularly giant companions (Schlaufman & Winn, 2016). This lack of nearby companions is expected from a high-eccentricity migration formation pathway - a scenario in which the hot Jupiter migrates inwards from beyond the ice line via some form of gravitational perturbations that put it on an eccentric orbit that eventually circularizes much closer to the host star (Rasio & Ford, 1996). This high-eccentricity migration results in the scattering and possible ejection of other planets in the system as the hot Jupiter's eccentric orbit sweeps through the inner parts of the stellar system (Mustill et al., 2015).

Of the $\sim$500 hot Jupiters currently confirmed, only three have proven to be exceptions to this lonely trend so far. The systems WASP-47 (Becker et al., 2015), Kepler-730 (Cañas et al., 2019), and TOI-1130 (Huang et al., 2020a) all host a hot Jupiter with at least one nearby companion planet, making the high-eccentricity migration scenario for these planetary systems unlikely[1]. It is more likely that these planetary systems formed via disk migration, where the protoplanets migrate inwards all together within the disk, potentially preserving planets near the hot Jupiter (Lin et al., 1996; Lee & Peale, 2002; Raymond et al., 2006). These systems serve as rare opportunities to dynamically constrain the formation of hot Jupiters and also potentially serve as a bridge to the slightly cooler population of warm Jupiters ($10 < P < 100$ d), which are often joined by smaller companion planets (Huang et al., 2016). Hot Jupiters with nearby planets may be key in understanding the connection of formation pathways to the observed hot Jupiter population.

The Transiting Exoplanet Survey Satellite (TESS; Ricker, 2015) is well suited to the discovery of hot Jupiters and potential nearby companions, as its almost-all-sky coverage is expected to observe nearly every known hot Jupiter system and discover hundreds or thousands more (Sullivan et al., 2015; Barclay et al., 2018). This is particularly important since the hot Jupiter sample is currently heterogeneous and incomplete (Yee et al., 2021). In addition, TESS has the photo-

[1]We note WASP-148b is a hot Jupiter with an outer, massive companion at just within 3 times the orbital distance of the hot Jupiter. We choose not to include this system in our discussion of hot Jupiters with nearby companions because of its very different architecture from the other systems (which have smaller, closer companions) and because the mass and orbital distance of the companion planet puts it on the borderline of the approximate definition of hot Jupiters with close planetary companions.

metric precision to identify smaller planets down to $\sim$0.7 $R_\oplus$ (e.g. Kostov et al., 2019b; Gilbert et al., 2020; Silverstein et al., 2022).

Here we present the TESS discovery of TOI-822.02 — henceforth referred to as WASP-132 c — a small planet associated with hot Jupiter WASP-132 b first discovered by Hellier et al. (2017). The new planet WASP-132 c is on a 1.01 d orbit interior to the 7.13 d orbit of the hot Jupiter WASP-132 b. This makes the WASP-132 system the fourth such system containing a hot Jupiter with a nearby small planetary companion, widening the sample of this rare subclass of hot Jupiters and further opening the possibility for comparative planetology both within the hot Jupiter system and between hot and warm Jupiter systems.

Section 3.3 details the discovery of the WASP-132 c signal in the TESS photometric data as well as the initial vetting efforts. Section 3.4 presents our refinement of the stellar parameters of the host star using a series of independent models. Section 3.5 describes our methodology for modeling the full photometric light curve to obtain precise planetary and orbital parameters for WASP-132 c as well as the confirmed hot Jupiter WASP-132 b. Section 4.6 presents the validation of WASP-132 c as a planet based on ground-based follow-up observations and statistical validation software. Section 3.7 details the dynamical simulations modeling a two-planet WASP-132 system to probe the long-term stability of the system. Section 3.8 discusses the implications of the discovery of such a system in terms of hot Jupiter formation and the larger hot Jupiter sample.

3.3 Signal Search and Vetting

WASP-132 (TOI-822, TIC 127530399) was observed by TESS in Sector 11 from UT April 23 to May 20, 2019 (23.96 d) in CCD 2 of Camera 1 and in Sector 38 from UT April 29 to May 26, 2021 (26.34 d) in CCD 1 of Camera 1. Data for WASP-132 were collected at 2 minute cadence in Sectors 11 and 38 and at 20 second cadence in Sector 38. The star was prioritized for high-cadence measurements as part of the Cycle 1 Guest Investigator Programs G011112, G011183, and G011132 and Cycle 3 Guest Investigator Programs G03278, G03181, and G03106.[2]

The TESS Science Processing Operation Center (SPOC) pipeline (Jenkins et al., 2016) processed the short cadence pixel data and generated the target pixel files (TPFs) and light curves cleaned of instrumental systematics. The Transiting Planet Search module (TPS; Jenkins, 2002; Jenkins et al., 2010; Jenkins et al., 2020) of the SPOC pipeline searched the generated 2-minute light curves for periodic, transit-like signals for each TESS sector independently and jointly as a single light curve. TPS recovered the previously confirmed hot Jupiter WASP-132 b as well as a new signal at 1.01153 d with a signal-to-noise ratio (SNR) of 10.6 in the combined data from the two sectors. This signal's depth corresponds to a planet with a radius of $2.33 R_\oplus$ when using the stellar radius value for this target contained in the TESS Input Catalog (TICv8.2; Stassun et al., 2018, 2019a) to calculate the potential planet radius. The transits of the hot Jupiter and WASP-132 c in the TESS data can be seen in Figure 3.1.

To provide an independent recovery of this periodic signal, we searched the available WASP-132 TESS light curves with the Transit Least Squares (TLS) search algorithm (Hippke & Heller, 2019). TLS utilizes analytical transit shapes, making it more sensitive to planet transits

[2]Details of approved TESS Guest Investigator Programs are available from `https://heasarc.gsfc.nasa.gov/docs/tess/approved-programs.html`

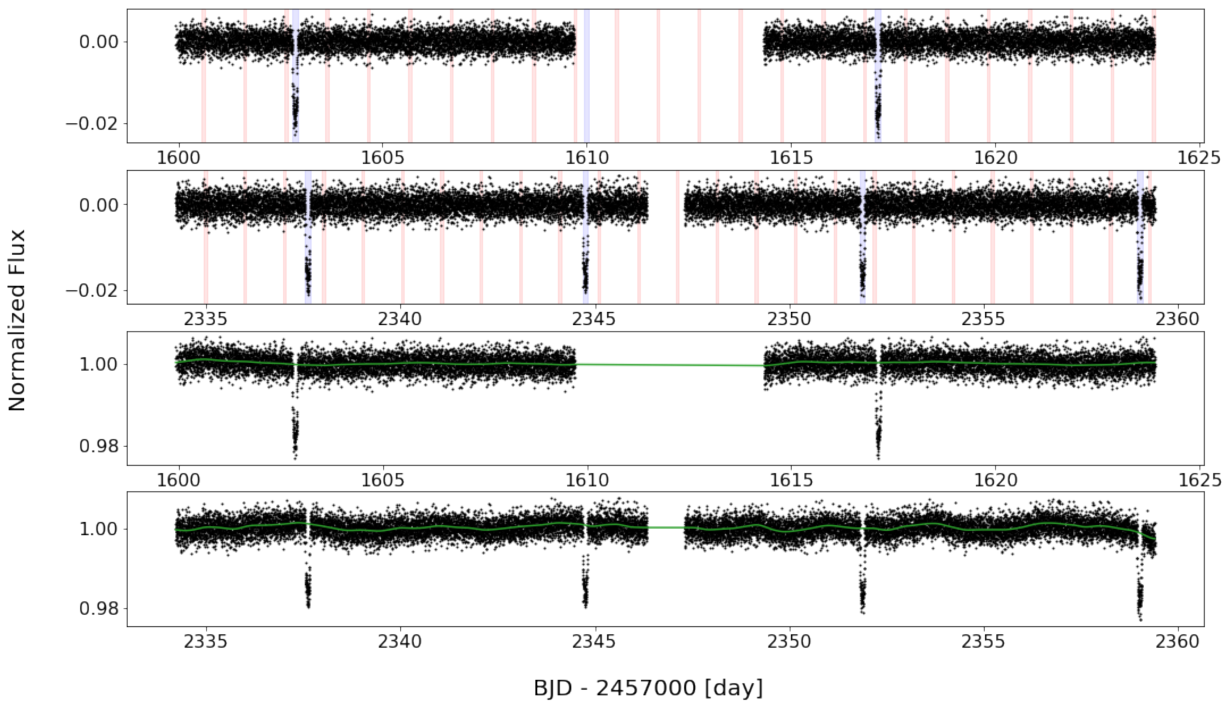

Figure 3.1: TESS PDC_SAP light curve of the WASP-132 system with the in-transit times of hot Jupiter WASP-132 b (blue) and WASP-132 c (red) highlighted. Both Sector 11 (top) and Sector 38 (second from top) are shown. The data is detrended with a Gaussian Process according to the method outlined in Section 3.5. These Gaussian Process noise models are shown in green for Sector 11 (second from bottom) and Sector 38 (bottom) overlaid on the PDC_SAP light curves to show how they capture the variability in the light curve.

than the conventional Box Least Squares (BLS; Kovács et al., 2002) search method and more finely tuned to detect small, short-period planets such as WASP-132 c.

Our transit search with TLS made use of the systematics-corrected Presearch Data Conditioning Simple Aperture Photometry (PDC_SAP) TESS light curves generated by the TESS SPOC pipeline (Smith et al., 2012; Stumpe et al., 2012, 2014) at the 2 minute and 20 second cadence for TESS Sectors 11 and 38, respectively[3]. We used the `lightkurve` Python package (Lightkurve Collaboration et al., 2018a) to download the data from the Mikulski Archive for Space Telescopes (MAST). The light curve exhibited small amplitude stellar variability and was detrended using `lightkurve`'s built in `flatten` method. A window length of >0.5 days was chosen as it was large enough to preserve transit signals (of duration on the order of $\lesssim$3 hours) while small enough to remove the slight stellar variability present in the light curve.

Using TLS on the clean light curve, we recovered the known signal of hot Jupiter WASP-132 b as well as a signal with a period of 1.0119 ± 0.0032 d with a false alarm probability (FAP) $< 10^{-4}$, which is well below the threshold of what Hippke & Heller (2019) states is a significant detection above white noise. The period, depth, and mid-transit time of this recovered signal are consistent with the values reported by the SPOC pipeline and listed on the Exoplanet Follow-up Observing Program-TESS (ExoFOP-TESS, ExoFOP 2019) website[4]. This recovery with TLS served as an independent check to ensure that the signal was not a pipeline-specific detection.

We performed multiple initial checks of the signal and TESS light curves for astrophysical false-positive scenarios that can mimic exoplanet transits. The Data Validation module (DV, Twicken et al., 2018a; Li et al., 2019a) of the SPOC pipeline performs a suite of diagnostic

[3]We elected to use the shortest cadence available for each sector to capture the shape of the transit as accurately as possible. As discussed in Chapter 2, the FFIs are not usually sensitive enough to find small nearby companions to hot Jupiters.

[4]`https://exofop.ipac.caltech.edu/tess/`

vetting tests to investigate the likelihood of many of these false-positive scenarios. These tests include a depth test of the odd and even transits, a statistical bootstrap test that accounts for the non-white nature of the light curve to estimate the probability of a false alarm from random noise fluctuations, a ghost diagnostic test to compare the detection statistic of the optimal aperture against that of a halo with a 1 pixel buffer around the optimal aperture, and a difference image centroid test. WASP-132 c passed all of these diagnostic vetting tests. Additionally, all TICv8.2 objects other than the target star were statistically excluded as sources of the 1.01 d transit signal since the difference centroid offset tests located the source of the transit signal to within 1 ± 3 arcsec of the target position. The Threshold Crossing Event (TCE) was promoted to TESS Object of Interest (TOI; Guerrero et al., 2021) status and designated TOI-822.02 by the TESS Science Office based on the clean model fit and diagnostic test results in the SPOC data validation report.

In addition to the vetting checks performed by the SPOC pipeline, we used the Discovery and Vetting of Exoplanets (`DAVE`; Kostov et al., 2019a) tool to further check for astrophysical false-positive scenarios. `DAVE` is an automated vetting pipeline built upon many of the tools developed for vetting planets in *Kepler* data (e.g. RoboVetter; Coughlin et al., 2014a). It has been used extensively in vetting planets in *K2* (Hedges et al., 2019; de Leon et al., 2021) and TESS (Kostov et al., 2019b; Crossfield et al., 2019; Gilbert et al., 2020a) data as well. `DAVE` performs two sets of vetting tests. The first are light curve-based vetting tests searching for odd/even transit differences, secondary eclipses, and light curve modulations that could introduce transit-like signals. The second set of tests are image-based that check the photocenter motion on the TESS image during transit.

Unfortunately, due to the weak signal resulting from the shallow transit depth and relatively dim ($Tmag$=11.11) stellar host, many of the results from `DAVE` were inconclusive but still showed no significant indication of an astrophysical false-positive scenario. As such, we determined that further, more detailed modeling of the transits was warranted.

3.4 Refinement of Host Star Parameters

To perform a comprehensive analysis of the transit and system light curve, it was necessary to refine the stellar parameters of the host star, WASP-132. The TICv8.2 reports key stellar parameters determined via independent analysis, but there are also stellar parameters reported by the WASP Collaboration in the initial discovery and confirmation of the hot Jupiter WASP-132 b (Hellier et al., 2017). We performed our own independent analysis given available data in order to determine the best values for the stellar parameters to use when modeling the TESS data. The results of each independent analysis method are contained in Table 3.1 for comparison. We find most stellar parameter values from each analysis method are consistent with each of the others as well as with both those reported by Hellier et al. (2017) and the TICv8.2 (Stassun et al., 2018, 2019a). The exception is a slight difference between the bolometric flux $F_{\rm bol}$ reported by the two SED analyses. The adopted stellar parameter values used in the remaining validation and analysis of WASP-132 c are based on the isochrone analysis described below and are contained in Table 3.2.

We also note that we see a low-amplitude 8 d periodic variation upon visual inspection of the Sector 38 light curve that does not match up with the 33 day stellar rotation period stated in Hellier et al. (2017). If the 8 d variability were to represent the rotation period of the star, this would imply a v sin i of $\sim$ 5 km s^{-1}, using the equation v sin i = (2πR)/P and assuming the star is viewed edge-on. This is well outside of the confidence interval of the measured value v sin i

Table 3.1: Stellar parameters obtained using each of the methods outlined in Section 3.4. Values from Hellier et al. (2017), which discovered WASP-132 b, and from the TICv8.2 (Stassun et al., 2018, 2019a) are included for comparison. The final adopted parameters for this analysis are contained in Table 3.2. All uncertainties reported are the 1σ value.

Parameter	TICv8.2	Hellier et al. (2017)	Isochrone Analysis	KGS SED Analysis	MLS SED Analysis
$T_{\rm eff}$ (K)	4742 ± 129	4750 ± 100	4714^{+87}_{-88}	4750 ± 75	4753 ± 80
[Fe/H]	—	0.22 ± 0.13	0.18 ± 0.12	0.0 ± 0.5	—
M_* ($M_\odot$)	0.760 ± 0.089	0.80 ± 0.04	0.782 ± 0.034	0.80 ± 0.05	—
R_* ($R_\odot$)	0.790 ± 0.057	0.74 ± 0.02	$0.753^{+0.028}_{-0.026}$	0.752 ± 0.024	0.767 ± 0.026
L_* ($L_\odot$)	0.284 ± 0.012	—	$0.253^{+0.032}_{-0.028}$	—	0.271 ± 0.007
log(g)	4.524 ± 0.094	4.6 ± 0.1	$4.576^{+0.028}_{-0.036}$	—	—
ρ_* (g cm^{-3})	2.17 ± 0.59	$2.82^{+0.10}_{-0.20}$	$1.81^{+0.18}_{-0.19}$	—	—
Age (Gyr)	—	$\gtrsim 0.5$	$7.055^{+7.114}_{-5.000}$	3.2 ± 0.5	—
Distance (pc)	122.91 ± 0.57	120 ± 20	126 ± 5	—	—
$F_{\rm bol}$ (erg s^{-1} cm^{-2} $\times 10^{-10}$)	—	—	—	5.442 ± 0.063	5.69 ± 0.14

= 0.9 ± 0.8 km s^{-1}, suggesting that this 8 d variability is not the stellar rotation period, although it may represent one of the harmonics of the true period if it is intrinsic to the star. However, extracted light curves using different apertures do not contain this $\sim$8 day variation, suggesting that this shorter-scale variability may not be inherent to the WASP-132 system. Regardless of the origin of this additional variability, our conclusions remain the same regarding the planetary nature of the 1.01 d transit signal.

Overall, WASP-132 does not show significant signs of activity. There is the possible 8 d variability and reported 33 d rotation period, activity that occurs on much longer timescales than the orbital period of WASP-132 c. We also found no evidence of flares or star spot crossings in either the space- or ground-based data. In the modeling of the system's light curves (see Section 3.5), a Gaussian Process was used to capture any variability in conjunction with transit models for each planet. Thus, photometric variability was modeled out while not diluting the transit signals (see Figure 3.1), in order to precisely measure the planet and orbital parameters.

Table 3.2: Adopted stellar parameters for WASP-132.

Parameter	Value	Source
	Identifying Information	
Name	WASP-132	
TIC ID	127530399	TICv8.2
TOI ID	TOI-822	Guerrero et al. (2021)
Alt. Name	UCAC4 220-083803	
	Astrometric Properties	
α R.A. (hh:mm:ss)	14:30:26.21 (J2015.5)	Gaia EDR3
δ Dec. (dd:mm:ss)	-46:09:34.29 (J2015.5)	Gaia EDR3
μ_α (mas yr^{-1})	12.255 $\pm$ 0.020	Gaia EDR3
μ_δ (mas yr^{-1})	-73.169 $\pm$ 0.022	Gaia EDR3
Distance (pc)	123.57 $\pm$ 0.29	Gaia EDR3
	Stellar Properties	
Spectral Type	K4	Hellier et al. (2017)
$T_{\rm eff}$ (K)	4714^{+87}_{-88}	This Work
[Fe/H]	0.18 $\pm$ 0.12	This Work
M_* (M$_\odot$)	0.782 $\pm$ 0.034	This Work
R_* (R$_\odot$)	$0.753^{+0.028}_{-0.026}$	This Work
L_* ($L_\odot$)	$0.253^{+0.032}_{-0.028}$	This Work
log(g)	$4.576^{+0.028}_{-0.036}$	This Work
ρ_* (g cm^{-3})	$1.81^{+0.18}_{-0.19}$	This Work
Rotation period (d)	$\sim$33	Hellier et al. (2017)
v sin i (km s^{-1})	0.9 $\pm$ 0.8	Hellier et al. (2017)
Age (Gyr)	3.2 $\pm$ 0.5	This Work
	Photometric Properties	
B (mag)	13.142 $\pm$ 0.011	APASS DR9
V (mag)	11.938 $\pm$ 0.046	APASS DR9
$G_{\rm G}$ (mag)	11.7467 $\pm$ 0.0002	Gaia EDR3
$G_{\rm BP}$ (mag)	12.3000 $\pm$ 0.0007	Gaia EDR3
$G_{\rm RP}$ (mag)	11.0487 $\pm$ 0.0004	Gaia EDR3
T (mag)	11.111 $\pm$ 0.006	TICv8.2
J (mag)	10.257 $\pm$ 0.026	2MASS
H (mag)	9.745 $\pm$ 0.023	2MASS
$K_{\rm s}$ (mag)	9.674 $\pm$ 0.024	2MASS
W_1 (mag)	9.557 $\pm$ 0.022	AllWISE
W_2 (mag)	9.638 $\pm$ 0.020	AllWISE
W_3 (mag)	9.575 $\pm$ 0.040	AllWISE
W_4 (mag)	8.281[1]	AllWISE

Gaia EDR3 - Prusti et al. (2016); Brown et al. (2021), TICV8.2 - Stassun et al. (2019a), APASS DR9 - Henden et al. (2016), 2MASS - Skrutskie et al. (2006a), AllWISE - Cutri et al. (2013).
[1]Only a limit is reported for W_4 since the signal-to-noise ratio was too low for a confident detection.

3.4.1 Isochrone Analysis

We performed an isochrone-based analysis for WASP-132 using `isoclassify` (Huber et al., 2017; Berger et al., 2020), which produces fundamental stellar parameters from a combination of input observables. We used spectroscopic T_{eff} and metallicity from the discovery paper (Hellier et al., 2017), $Gaia$ Data Release 2 (Prusti et al., 2016; Gaia Collaboration et al., 2018; Bailer-Jones et al., 2018, DR2) parallax and coordinates, and the Two Micron All-Sky Survey (Skrutskie et al., 2006a, *2MASS)* K_{s} magnitude as inputs. We also used the `allsky` extinction map detailed in Bovy et al. (2016) to estimate the photometric extinction based on the coordinates and distance inferred from the parallax. The best-fit values and their uncertainties are compiled in Table 3.1, and we estimate extinction to be A_V = 0.097 $\pm$ 0.024 mag, which is consistent with the A_V = 0.093 $\pm$ 0.031 mag reported in the TICv8.2.

3.4.2 KGS SED Analysis

As an independent determination of the basic stellar parameters, K.G. Stassun (KGS) performed an analysis of the broadband spectral energy distribution (SED) of the star together with the *Gaia* Early Data Release 3 (Prusti et al., 2016; Brown et al., 2021, EDR3) parallax (with no systematic offset applied; see, e.g., Stassun & Torres, 2021), in order to determine an empirical measurement of the stellar radius, following the procedures described in Stassun & Torres (2016); Stassun et al. (2017); Stassun et al. (2018). We pulled the the JHK_S magnitudes from *2MASS*, the W1–W3 magnitudes from the Wide-field Infrared Survey Explorer (*WISE*; Wright et al., 2010; Cutri et al., 2013), and the $G_{\text{BP}}G_{\text{RP}}$ magnitudes from *Gaia*. Together, the available photometry spans the full stellar SED over the wavelength range 0.4–10 μm (see Figure 3.2).

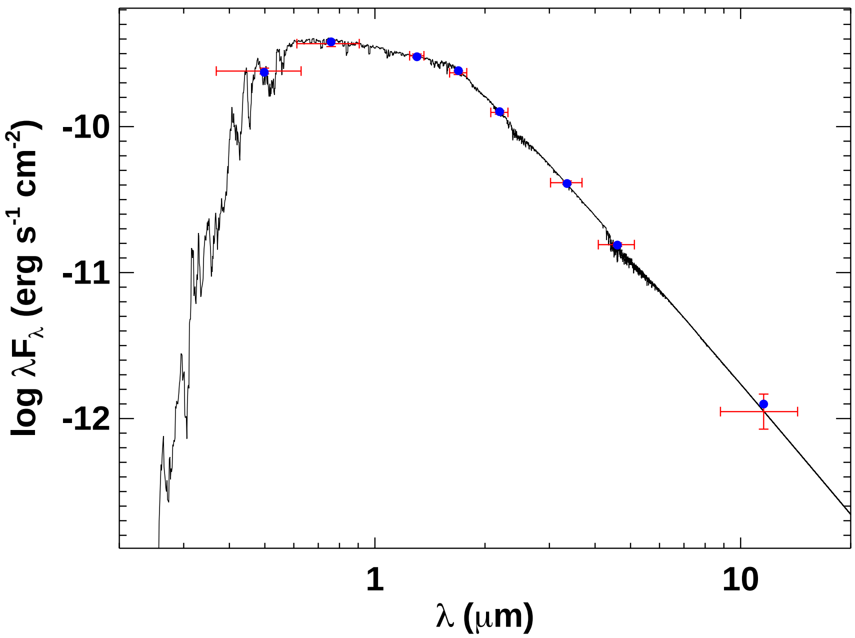

Figure 3.2: Spectral energy distribution of WASP-132. Red symbols represent the observed photometric measurements outlined in Section 3.4.2, where the horizontal bars represent the effective width of the passband. Blue symbols are the model fluxes from the best-fit NextGen atmosphere model (black).

We performed a fit using NextGen stellar atmosphere models, with the free parameters being the effective temperature ($T_{\rm eff}$) and metallicity ([Fe/H]), as well as the extinction A_V, which we fixed at zero due to the proximity of the system to Earth. The resulting fit (Figure 3.2) has a best-fit $T_{\rm eff} = 4750 \pm 75$ K, [Fe/H] = 0.0 ± 0.5, with a reduced χ^2 of 0.8. Integrating the (unreddened) model SED gives the bolometric flux at Earth, $F_{\rm bol} = 5.442 \pm 0.063 \times 10^{-10}$ erg s^{-1} cm^{-2}. Taking the $F_{\rm bol}$ and $T_{\rm eff}$ together with the *Gaia* parallax gives the stellar radius, $R_\star = 0.752 \pm 0.024$ R$_\odot$. In addition, we can estimate the stellar mass from the empirical relations of Torres et al. (2010), giving $M_\star = 0.80 \pm 0.05$ M$_\odot$. Finally, the reported stellar rotation period of $\sim$33 d implies an age of $\tau_\star = 3.2 \pm 0.5$ Gyr via the empirical gyrochronology relations of Mamajek & Hillenbrand (2008).

3.4.3 MLS SED Analysis

As an additional check on our stellar effective temperature, luminosity, and radius results, M. L. Silverstein (MLS) led a second SED analysis following methodology similar to Dieterich et al. (2014) (Silverstein et al., in preparation). Spanning optical to mid-infrared wavelengths, we extract JHK_S magnitudes from *2MASS* and W1–W3 magnitudes from *WISE* as in the previous subsection. We differ in our adoption of the *Gaia* DR2 parallax and of VRI photometry converted from *Gaia* DR2 $G_{\rm G}G_{\rm BP}G_{\rm RP}$. We compare nine different color combinations to the BT-Settl 2011 photospheric models (Allard et al., 2012) to derive a best-fitting $T_{\rm eff} = 4753 \pm 80$ K, assuming [Fe/H] = 0. Next we iteratively scale the resulting best-match model using a polynomial function until model and observed photometry match to within the error bars. We then integrate the final spectrum and apply a bolometric correction to determine $F_{\rm bol} = 5.691 \pm 0.137 \times 10^{-10}$ erg s^{-1} cm^{-2}, and we scale by the parallax to derive $L_* = 0.271 \pm 0.007\ L_\odot$. A radius of $R_* = 0.767 \pm 0.026\ R_\odot$ is then calculated using the Stefan-Boltzmann Law. These results are listed in Table 3.1 and match those from the other independent methods described in this chapter.

3.5 Modeling the Physical Properties of WASP-132 c

While TLS is useful at detecting signals, the period grid that it searches is not very fine by default. Combined with the refined stellar parameters discussed in Section 3.4, it is possible to model the light curve in a more detailed fashion than the initial transit search to find the maximum likelihood values for the planet properties in the system. To perform this detailed modeling, we used the software `exoplanet` (Foreman-Mackey et al., 2019). `exoplanet` is a toolkit for probabilistic modeling of transit and radial velocity observations of exoplanets using

PyMC3. This is a powerful and flexible program that can be used to build high-performance transit models and then sample them through Markov Chain Monte Carlo (MCMC) simulations to provide precise transit and orbital parameters.

We utilized the same PDC_SAP light curves used in the transit search with TLS with one difference. For the modeling with `exoplanet`, we did not apply any initial detrending that could possibly alter the transit signals but instead included a Gaussian Process (GP) in the model. Our model had three elements: two planet components with Keplerian orbits and limb-darkened transits (one for each potential planet in the system) and a GP component that modeled residual stellar variability. The planet models were computed using STARRY (Luger et al., 2019) and the GP was computed using `celerite` (Foreman-Mackey et al., 2017; Foreman-Mackey, 2018). The GP component models the residual stellar variability in the light curve and describes a stochastically-driven, damped harmonic oscillator with two hyper-parameters, ln(S_0) and ln(ω_0), which represent the undamped angular frequency of a simple harmonic oscillator and the power at ω = 0, respectively. We fixed the quality factor Q of the simple harmonic oscillator to 1 / $\sqrt{2}$ and put wide Gaussian priors on ln(S_0) and ln(ω_0), setting their means to the natural log of the standard deviation of the flux and natural log of one tenth of a cycle, respectively, with both of their standard deviations set to 10. This form of GP has the advantage of being able to model a wide range of low frequency astrophysical and instrumental signals without requiring a physical model for the observed variability. We also included a white noise term in the model which is parameterized by the natural log of the standard deviation of the flux with a prior identical to that of ln(S_0). The GP parameters of the two TESS sectors were modeled separately since the sectors may have different noise parameters, especially since the data were taken at different cadences.

The planet model was parameterized with a two term limb-darkening component and the stellar radius and mass. The individual planets were parameterized in terms of the natural log of orbital period, mid-transit time, transit depth, impact parameter, eccentricity, and periastron angle at time of transit. For our priors on the stellar parameter components of the model, we used the mean and standard deviation values of our analysis discussed in Section 3.4 and displayed in Table 3.2. We followed Kipping (2013a) for the parameterization of the limb-darkening. We used the SPOC values listed on ExoFOP-TESS for the means and standard deviations of Gaussian priors on the natural log of the orbital period, mid-transit time, and transit depth for the two planets. We imposed a uniform prior on the impact parameter bounded between 0 and 1. For the eccentricity prior, we used a Beta prior with α = 0.867 and β = 3.03 as suggested by Kipping (2013b). The eccentricity was bounded between zero and one and sampled as $e\cos(\omega)$. The periastron angle at transit was sampled in vector space to avoid the sampler seeing discontinuities. We sampled the posterior distribution of the model parameters using the No U-turn Sampler (NUTS; Hoffman et al., 2014), which is a form of Hamiltonian Monte Carlo, as implemented by `PyMC3` (Salvatier et al., 2016a). We ran 3 simultaneous chains, each with 2000 tuning steps and 2500 draws in the final sample.

Initially, since individual TESS sectors often have different noise properties, we modeled both Sectors 11 and 38 independently from one another using the model described above. However, the resulting posterior distributions were equivalent within 1σ errors, so we decided to combine both sectors of TESS data into a single light curve and use the same model. Since the two light curves are separated by $>$1 year, modeling both together as a single light curve increases the time baseline with which to model the orbit of the system, allowing for a better constrained orbital period than any individual sector or two sectors back-to-back in time. We binned the Sector 38 TESS data from 20 second cadence to 2 minute cadence to match with the TESS Sector 11

Table 3.3: Planet and orbital parameters for WASP-132 b and c calculated by modeling the TESS photometric data with `exoplanet`. Errors are reported at the 1σ level. Noise parameters are also included.

Parameter	Value
Model Parameters	
Star	
Limb darkening u_1	0.43 ± 0.11
Limb darkening u_2	0.17 ± 0.24
Radius [$R_\odot$]	0.754 ± 0.024
Mass [$M_\odot$]	0.781 ± 0.033
ln($\rho_{\rm GP}$)	1.03 ± 0.15
ln($\sigma_{\rm GP,S11}$)	-7.96 ± 0.16
ln($\sigma_{\rm GP,S38}$)	-7.11 ± 0.16
WASP-132 c	
T_0 (BJD - 2457000)	1597.5762 ± 0.0024
ln(Period) [days]	$0.011 \pm 4.69\text{e-}6$
Impact parameter	$0.28^{+0.24}_{-0.19}$
ln(Transit Depth)	-7.437 ± 0.068
eccentricity	$0.13^{+0.20}_{-0.09}$
ω [radians]	$-0.93^{+1.83}_{-1.65}$
WASP-132 b	
T_0 (BJD - 2457000)	2337.6080 ± 0.0002
ln(Period) [days]	$1.96 \pm 5.49\text{e-}7$
Impact parameter	0.16 ± 0.11
ln(Transit Depth)	-4.026 ± 0.01
eccentricity	$0.07^{+0.15}_{-0.05}$
ω [radians]	$-0.08^{+2.55}_{-2.67}$
Derived Parameters	
WASP-132 c	
Period [days]	1.011534 ± 0.000005
$R_{\rm p}/R_*$	0.023 ± 0.001
Radius [$R_\oplus$]	1.85 ± 0.10
Radius [$R_{\rm J}$]	0.165 ± 0.009
a/R_*	5.17 ± 0.18
a [AU]	0.0182 ± 0.0003
Inclination [deg]	$86.64^{+1.12}_{-3.52}$
Duration [hours]	$1.47^{+0.14}_{-0.22}$
WASP-132 b	
Period [days]	7.133514 ± 0.000004
$R_{\rm p}/R_*$	0.122 ± 0.006
Radius [$R_\oplus$]	10.05 ± 0.34
Radius [$R_{\rm J}$]	0.897 ± 0.030
a/R_*	19.03 ± 0.66
a [AU]	0.067 ± 0.001
Inclination [deg]	$89.51^{+0.14}_{-0.49}$
Duration [hours]	$3.18^{+0.18}_{-0.21}$

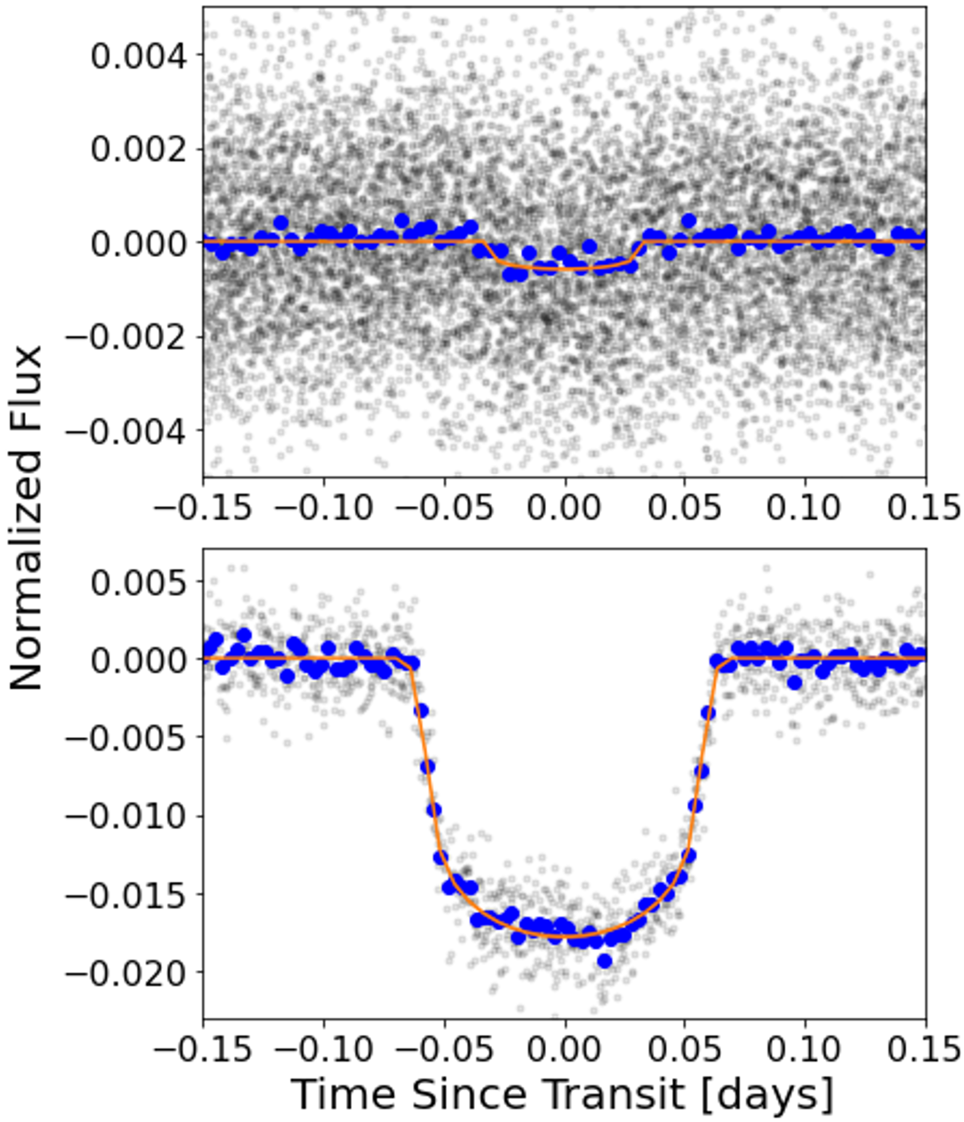

Figure 3.3: TESS data (light gray) for WASP-132 c (top) and WASP-132 b (bottom) phase folded to the best-fit period and mid-transit time with the `exoplanet` model overlaid. The process of fitting the transit model is described in Section 3.5. The blue points are the phase-folded photometric data binned for clarity.

data in order to create a uniform data set with an increased photometric precision in Sector 38. No correction for contamination from nearby sources of constant brightness was included since follow up observations by SOAR and LCOGT cleared the nearby field of contaminating sources of this nature (see Section 3.6.1).

The median values and 1σ errors for the best-fit transit model are contained in Table 3.3 and the folded light curve with the best-fit and 1σ bounds of the transit model are shown in Figure 3.3.

3.6 Validation of WASP-132 c

While the TESS pipeline and `DAVE` perform vetting analysis against possible false alarm and false positive scenarios, they alone are not rigorous enough to validate the planetary nature of WASP-132 c. We therefore investigated this signal using both observational constraints (Section 3.6.1) as well as publicly-available statistical software packages `vespa` and `TRICERATOPS` (Section 3.6.2).

3.6.1 Follow-up Observations

In order to better constrain the false positive probability of a planet candidate, follow-up observations can rule out sections of the parameter space of different astrophysical false positive scenarios. Since WASP-132 is already known to host a confirmed hot Jupiter, both speckle imaging and radial velocity follow-up observations were readily available for our analysis and could be included in our final validation of WASP-132 c.

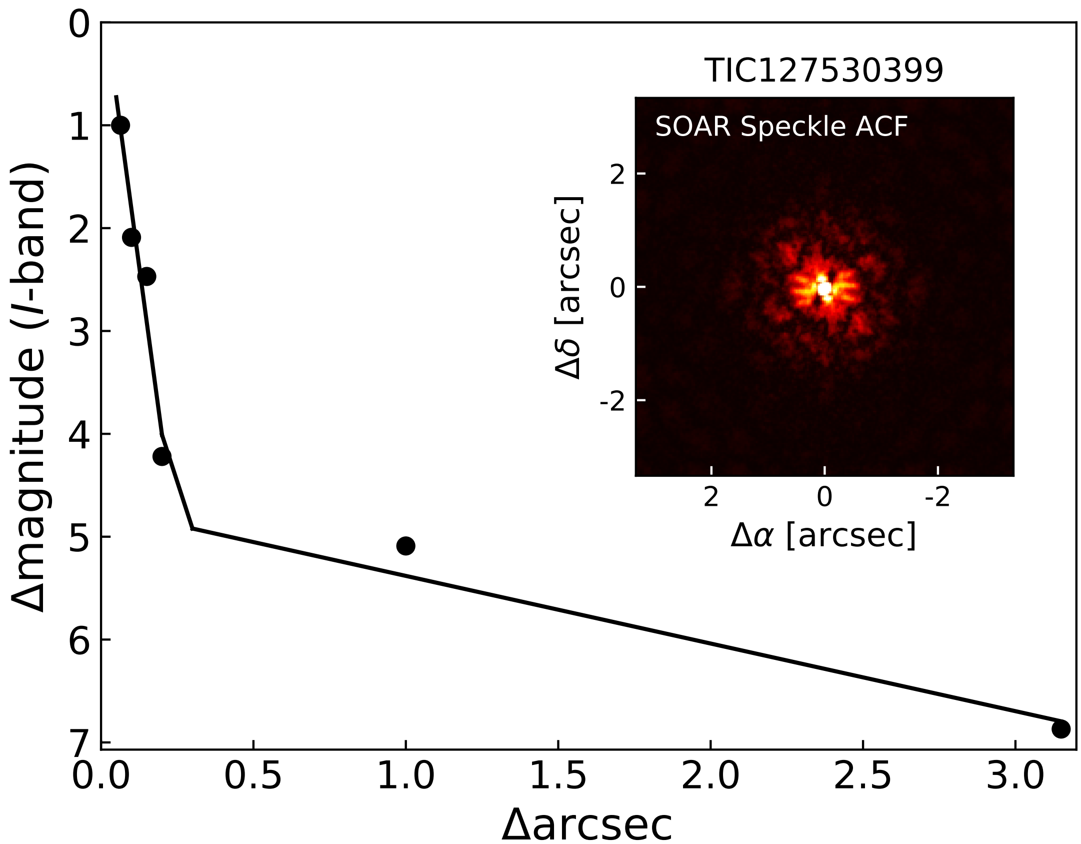

Figure 3.4: The 5-σ detection sensitivity of the SOAR speckle imaging of WASP-132, with inset two-dimensional auto-correlation function reconstructed image of the field. The data indicate that there are no close-in companions within 3 arcsecond of WASP-132.

3.6.1.1 SOAR Speckle Imaging

High-angular resolution imaging is needed to search for nearby sources that can contaminate the TESS photometry (resulting in an underestimated planetary radius) or be the source of astrophysical false positives, such as background eclipsing binaries. We searched for stellar companions to WASP-132 with speckle imaging using the HRCam instrument on the 4.1-m Southern Astrophysical Research (SOAR) telescope (Tokovinin, 2018) on 10 February 2020 UT, observing in Cousins I-band, a similar visible bandpass as TESS. This observation was sensitive to a 5.0-magnitude fainter star at an angular distance of 1 arcsec from the target. More details of the observation are available in Ziegler et al. (2020). The 5σ detection sensitivity and speckle auto-correlation functions from the observations are shown in Figure 3.4. No nearby stars were detected within 3" of WASP-132 in the SOAR observations.

3.6.1.2 CORALIE Radial Velocity Observations

In addition to SOAR speckle imaging, prior to the discovery of WASP-132 c there already existed radial velocity measurements of the host star WASP-132 which were used to confirm the planetary nature and measure the mass of the hot Jupiter WASP-132 b. In total, there were 36 radial velocity measurements taken across a time span of almost 2 years. All of these measurements were obtained with the CORALIE spectrograph which is an echelle spectrograph mounted on the 1.2-m Euler telescope in La Silla, Chile. These data are published in Hellier et al. (2017), which provides further information regarding the method used to reduce the radial velocity data.

According to the `forecaster` Python package (Chen & Kipping, 2016), the projected mass of WASP-132 c should be 4.45 $M_\oplus$. `forecaster` assumed a gaseous envelope when estimating the mass of WASP-132 c, however the radius of the planet may place it in the super-Earth regime of planets. This would imply that the density of the planet is higher than a gaseous planet, meaning that the mass follows the relation $M_\mathrm{p} \sim R_\mathrm{p}^{3.7}$. This would result in a mass of 9.74 $M_\oplus$. We made no distinction between these two scenarios in our analysis of CORALIE data since we imposed a very wide prior on the mass of WASP-132 c.

We first performed a joint fit of the time series TESS photometry with the CORALIE radial velocity measurements using `exoplanet`. This way, we were able to take advantage of the unique strengths of each data type in constraining the orbital and planet parameters as well as accounting for the noise and variability in the data. We used a model similar to that described in Section 3.5 but with the addition of planet mass as well as a quadratic trend and a jitter term for the radial velocities. The priors on the trend and jitter model components were Normal distributions with the quadratic trend distribution centered on 0 and the jitter term distribution centered on the standard deviation of the radial velocity data. We imposed a wide log-uniform prior on the mass from 0 to 8. This is more than wide enough to encompass the projected masses of both potential compositions for WASP-132 c as well as the 3σ upper limit on the reported mass of WASP-132 b. CORALIE also underwent an upgrade partway through the dataset and this is accounted for by an offset between the pre- and post-upgrade portions of the data. We also fit for the trend in the data described in Hellier et al. (2017).

The posterior probability distribution for the mass of WASP-132 c was highest around zero with a wide spread of values, indicating a non-detection in the radial velocity. Therefore, we report a 3σ upper limit from this distribution of 37.35 $M_{\oplus}$, corresponding to a radial velocity semi-amplitude upper limit of 28.23 ms^{-1}. All other planetary and orbital parameters modeled with the joint TESS + CORALIE data (e.g. period, mid-transit time, radius, etc.) are consistent with the values obtained from modeling the TESS data alone, described in Section 3.5. The best fit models are plotted with the phase-folded radial velocity data for WASP-132 b and c in Figure 3.5. We note that Hellier et al. (2017) report that the CORALIE radial velocities show excess scatter, which may be due to magnetic activity. Therefore, the upper limit on the mass reported here may be inflated due to the high scatter.

As a check on the validity of the procedure, we also compared the measured planet mass for the confirmed hot Jupiter in the system WASP-132 b against its reported mass in Hellier et al. (2017). We measure the mass to be 121.89 $\pm$ 21.85 $M_{\oplus}$ which is in agreement with the 130.31

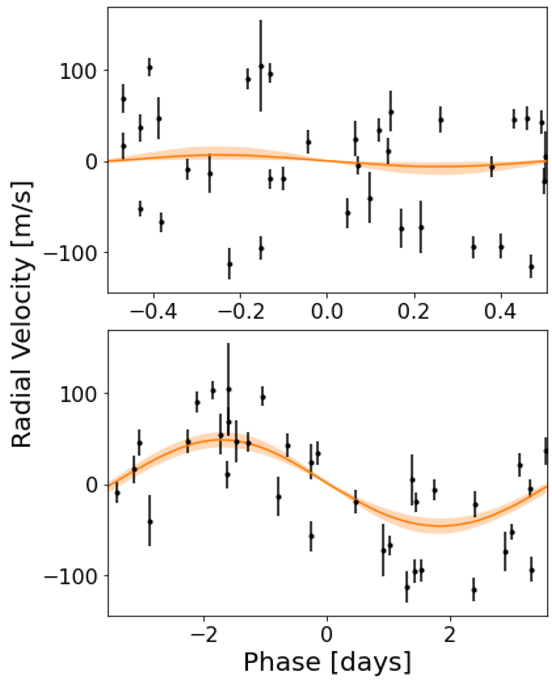

Figure 3.5: The CORALIE radial velocity measurements phase-folded to the best-fit periods of WASP-132 c (*top*) and WASP-132 b (*bottom*). The solid orange line represents the median radial velocity model and the shaded regions represent the 1σ uncertainties in the model.

$\pm$ 9.53 $M_{\oplus}$ measured by Hellier et al. (2017). The uncertainty on our calculated mass of the hot Jupiter is higher than that reported by Hellier et al. (2017) likely because Hellier et al. (2017) also joint fit the CORALIE data with photometric data from both Wide Angle Search for Planets (WASP) and TRAnsiting Planets and PlanetesImals Small Telescope (TRAPPIST) observations that our analysis does not include as well as other ancillary RV observation data products.

As an independent check of the values obtained from `exoplanet`, we used the online Data and Analysis Center for Exoplanets[5] (*DACE*) platform to model the radial velocity data and investigate the significance of any signals around 1.01 d (the period of WASP-132 c). The Keplerian model initial conditions for the hot Jupiter were input based on the values on ExoFOP-TESS for WASP-132 b and a decrease of 60 ms^{-1} over the course of the observations was added

[5] `https://dace.unige.ch`

as noted in Hellier et al. (2017). When viewing the periodigram of the radial velocity data after adding in these components, there appear to be spikes in signal around 1 d, but none of which has an FAP $< 10\%$. This is not surprising, since many signals are aliased to 1 d and this is a common phenomenon in analyzing radial velocity data. The addition of another Keplerian orbit at the expected orbital period of WASP-132 c with the predicted semi-amplitude based on the mass predicted by `forecaster` results in a higher reduced χ^2, indicating a worse fit.

According to Equation 14 in Lovis & Fischer (2011), the expected semi-amplitude of the radial velocity signal of WASP-132 c with 4.45 $M_\oplus$ as predicted by `forecaster` is 3.36 ms^{-1}. If an Earth-like composition is assumed, the mass of 9.74 $M_\oplus$ would result in a semi-amplitude of 7.44 ms^{-1}. CORALIE has been reported to have an individual measurement precision ranging between 3.5 and 6 ms^{-1} (Rickman et al., 2019), putting the projected mass of WASP-132 c slightly below and slightly above the lower limit of CORALIE's detectable parameter space for gaseous and Earth-like compositions, respectively. Combined with the fact that the orbital period falls very close to the highly-aliased value of 1 d, it is logical that there was no significant detection of WASP-132 c in the CORALIE radial velocity data. Further radial velocity observations are necessary with a more precise instrument such as the High Accuracy Radial velocity Planet Searcher (HARPS) or the Carnegie Planet Finder Spectrograph (PFS) in order to obtain a mass measurement for the planet WASP-132 c.

3.6.1.3 LCOGT 1 m

We observed TOI-822 c from the Las Cumbres Observatory Global Telescope (LCOGT; Brown et al., 2013a) 1.0 m network node at the South Africa Astronomical Observatory on UTC

2022 March 5, 2022 March 8, and 2022 March 9 in Sloan i' band. We used the `TESS Transit Finder`, which is a customized version of the `Tapir` software package (Jensen, 2013), to schedule our transit observations. The 1 m telescopes are equipped with 4096×4096 SINISTRO cameras having an image scale of $0''.389$ per pixel, resulting in a $26' \times 26'$ field of view. The images were calibrated by the standard LCOGT `BANZAI` pipeline (McCully et al., 2018). Photometric data were extracted using `AstroImageJ` (Collins et al., 2017). The target star apertures exclude virtually all of the flux from the nearest Gaia EDR3 and TESS Input Catalog known neighbor (TIC 1051778874), which is $10''.0$ northwest of TOI-822. The light curve data are available on the ExoFOP-TESS website[6] (ExoFOP, 2019).

The UTC 2022 March 5 observation used focused observations that were intended to saturate the target star for purposes of checking fainter stars within $2'.5$ of TOI-822 c for a potential nearby eclipsing binary (NEB) that could be the cause of the periodic detection in the TESS data. We rule out NEB signals, relative to the depth required in each neighboring star given its TIC version 8 delta TESS magnitude, by a factor of more than three times the RMS of the light curve scatter for all neighboring stars out to 50" from TOI-822. This is consistent with the SPOC pipeline's (lack of) centroid offset finding that the source of the TESS-detected signal is within ~ 10" of the target star location using data from TESS sectors 11 and 38. We also do not see any obvious NEB signals in stars out to $2'.5$, although some light curves suffer from blending from brighter nearby stars.

Although we expected the target star to be saturated in the UTC 2022 March 5 observation, it ultimately was strongly exposed, but not saturated. While the detrended light curve is consistent with a 40 min (2.7σ) late ~ 600 ppm deep event on-target relative to the SPOC sectors 11 and 38

[6] https://exofop.ipac.caltech.edu/tess/target.php?id=127530399

ephemeris, the detection is considered inconclusive due to limited post-transit baseline coverage and apparent systematics at the level of ~ 500 ppm in the undetrended light curve.

The UTC 2022 March 8 and UTC 2022 March 9 observations were intentionally defocused to attempt to confirm the tentative 2.7σ late ~ 600 ppm deep event in the UTC 2022 March 5 data. However, these data also suffered from ~ 500 ppm systematics in the undetrended light curves. With our best detrending efforts, the UTC 2022 March 8 would marginally suggest a roughly 100 min late $\sim 600 - 700$ ppm deep ingress at the end of the light curve. On the other hand, the UTC 2022 March 9 detrended light curve would suggest a roughly 20 min early ~ 700 ppm deep event.

Given the level of systematics in the undetrended data and the inconsistent timing of the three tentative transit detections in the detrended data, we do not further consider the on-target results in the following analyses. Although we favor the interpretation that the extracted events are systematics driven, we cannot rule out the interpretation that some or all of the tentative detections are astrophysical and that the timing offsets are indicative of large TTVs in the system.

3.6.2 Validation Using Software Tools

While observational constraints can rule out portions of the parameter space where astrophysical false positives could exist, these observational limits are incomplete and do not rule out the entirety of the false positive parameter space. We are able to statistically analyze the remaining likelihood of false positive signals using publicly-available software. Using the available follow-up observations as constraints, we ran `vespa` (Morton, 2012a, 2015a) and `TRICERATOPS` (Giacalone & Dressing, 2020a; Giacalone et al., 2021a) to further establish the planetary nature of this signal.

vespa compares the transit signal to a number of astrophysical false-positives including an unblended eclipsing binary (EB), a blended background EB (BEB), a hierarchical companion EB, and EB scenarios with a double-period. We ran vespa using the TESS light curves detrended with the noise model described in Section 3.5 and phase-folded using the median values of the posteriors for the period and mid-transit time. The modeled transits of hot Jupiter WASP-132 b were also subtracted from the light curve. We included the maximum possible secondary depth of phase-folded features calculated by DAVE (Section 3.3) and the SOAR I-band contrast curve (Section 3.6.1.1) as observational constraints when calculating the false positive probability of the WASP-132 c signal. By default, vespa simulates the background starfield within 1 square degree of the target, but we dictated that the maximum aperture radius interior to which the signal must be produced be $42''$, which is the radius of two TESS pixels and the maximum size of the aperture that the SPOC pipeline used to extract the light curves.

Using these inputs, we calculated the false positive probability (FPP) of the WASP-132 c signal to be 0.00193. The only false positive scenario with any remaining probability was the case of a blended background EB, however the probability for that scenario was $\ll$0.01 and is highly disfavored over the planet scenario. Since the overall FPP $\ll$0.01, this signal can be considered statistically validated by vespa.

As an independent check, we ran the WASP-132 c signal through the statistical validation software TRICERATOPS. This software is similar to vespa in that it checks the signal against a set of scenarios that could produce transit-like signals. TRICERATOPS was specifically designed for TESS observations and accounts for known nearby stars contained within the light curve extraction aperture as well as stars within $2.5'$ of the target. This tool calculates both the FPP of the signal and the probability that the planet candidate is a false positive originating from a known nearby star, labeled the nearby FPP (NFPP).

Since TRICERATOPS is sensitive to the extraction aperture, we ran TRICERATOPS using light curves extracted with two separate apertures for comparison and quality check. The first run used the apertures that the TESS SPOC pipeline used to extract the PDC_SAP light curves, which were 12 and 10 pixels centered on the target position for Sectors 11 and 38, respectively. The second run used custom light curves extracted using reduced apertures that were smaller than those used by the TESS SPOC pipeline with 4 and 6 pixels centered on the target position for Sectors 11 and 38, respectively.

For each TRICERATOPS run, we input the apertures used to extract the light curves, the I-band contrast curve from SOAR, and the median values for period and mid-transit time from the modeling performed in Section 3.5. The light curves used were phase-folded at these period and mid-transit time values. For each set of apertures, we ran TRICERATOPS twenty times and took the average FPP values. Using the apertures from the TESS SPOC pipeline, we obtained an FPP = 0.0126 $\pm$ 0.0003 for WASP-132 c. Using the reduced apertures, we obtained an FPP = 0.0107 $\pm$ 0.0004. Since the nearby field has been cleared of nearby and background eclipsing binary systems by the LCOGT observations (see Section 3.6.1.3), SOAR observations (see Section 3.6.1.1), and the the TESS SPOC centroid offset tests (which put the signal within 1 $\pm$ 3 arcsec of the target), we assume an NFPP value of 0.

According to Giacalone et al. (2021a), for a signal to be statistically validated as a planet by TRICERATOPS, it must have FPP < 0.015. Our signal of 1.01 d meets the TRICERATOPS FPP criterion for both sets of extraction apertures. For consistency, we also reran vespa on the reduced aperture light curve obtained an FPP = 9.02×10^{-5}, still well below the vespa statistical validation threshold. This difference in FPP between `vespa` and `TRICERATOPS` may stem from the fact that `TRICERATOPS` uses the actual TESS aperture and background star population while `vespa` simulates this with a extraction radius and TRILEGAL simulations. Therefore, given the `vespa` validation, sufficiently low `TRICERATOPS` FPP values, and strong constraints on nearby background stars in the field of view, we consider this signal to be statistically validated as a planet.

Furthermore, neither of these statistical validation packages account for the fact that this signal is a part of a multi-planet system. Lissauer et al. (2012a, 2014) demonstrated that false positives are less likely in multi-planet systems and that the FPPs calculated without accounting for this fact should be treated as upper limits. An analysis of TESS multiplanet systems indicates that this "multiplicity boost" may reduce these FPPs by a factor of $\sim 20\times$ (Guerrero et al., 2021), although the scarcity of inner companions to hot Jupiters suggests that the multiplicity boost should be smaller than this factor.

3.7 Dynamical Stability

To probe the dynamical stability of the system, we simulated the system using `REBOUND` (Rein & Liu, 2012), a flexible N-body integrator written in both Python and C. We ran 30 iterations of the system, each time perturbing the mass, eccentricity, inclination, and periods of each of the planets within their 3σ uncertainties to test stability at the extremes of the possible parameter space for both planets. Each iteration was integrated for simulation timescales of 100 Myr and a timestep of 0.2 d ($\sim$20% of WASP-132 c's best-fit orbital period) using the MERCURIUS integrator (Rein et al., 2019).

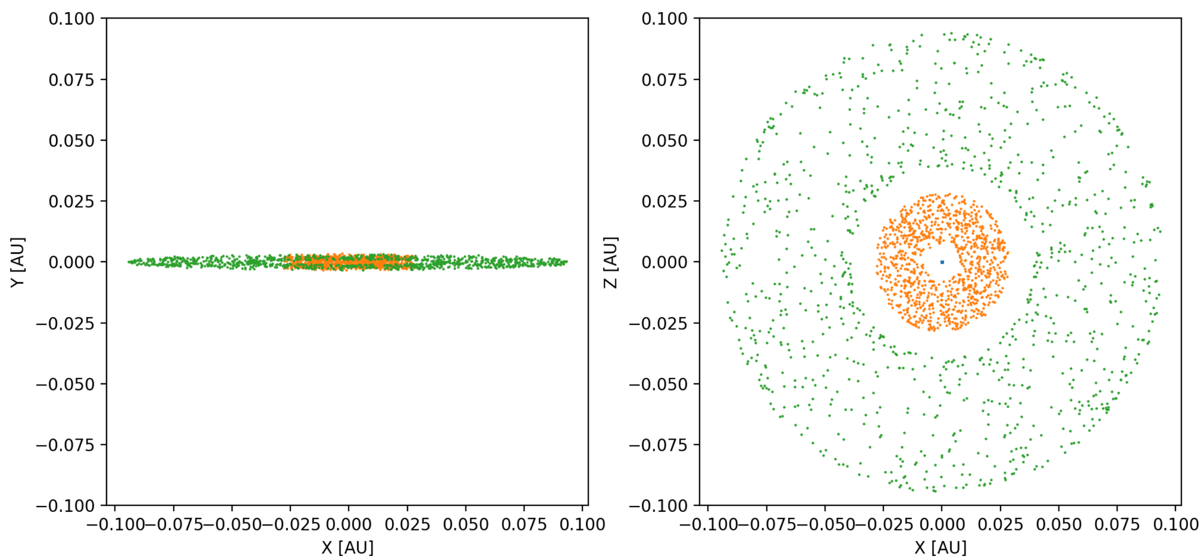

Figure 3.6: Position of WASP-132 b and c at 1000 evenly spaced points in time during the 1 Myr simulation with mass, eccentricity, and inclination initial values set to the 3σ upper limits for both planets. WASP-132 b is denoted by the outer, green points and WASP-132 c is denoted by the inner, orange points. *Left:* A side-on view of the system as it would be seen from Earth. *Right:* A top-down view to illustrate the positions of both planets as they orbit over the course of 1 Myr. Note the gap between the maximum distance of WASP-132 c and the minimum distance of WASP-132 b from the host star.

The MERCURIUS integrator is a hybrid integrator that uses the symplectic Wisdom-Holman integrator WHFast when particles are far apart from each other and switches to the higher order integrator IAS15 during close encounters, which integrates with a smaller, adaptive timestep. We specified the minimum timestep for the IAS15 integrator as 0.02 d in order to speed up computation time.

We found that the planetary system is stable for all portions of the parameter space simulated on timescales of 100 Myr. None of the simulations exhibited a drastic change in semi-major axis outside of the normal oscillations due to gravitational interactions between the three bodies in the system (the two planets and the host star). Furthermore, no collisions were registered between any of the bodies over the course of the simulations.

We also simulated the system using the 3σ upper limits on mass, eccentricity, and inclination for both of the planets in order to maximize the likelihood of a close encounter. We integrated this system using the MERCURIUS integrator for 1 Myr at a timestep of 1.2 hours ($\sim$5% of WASP-132 c's best-fit orbital period). The positions of both planets at 1000 different evenly-spaced timesteps can be seen in Figure 3.6. We found that the system was stable at the extreme end of the parameter space of both planets as there were no close encounters between the planets and no significant change in the semi-major axis the two planets over the course of the simulation. This is illustrated by the gap between the innermost positions of WASP-132 b and outermost positions of WASP-132 c in Figure 3.6. Given the stability from both the simulations with random draws of parameters as well as the simulation with the planet parameter values most likely to cause a close encounter, the addition of WASP-132 c into the WASP-132 system does not appear to affect the long-term stability of the system.

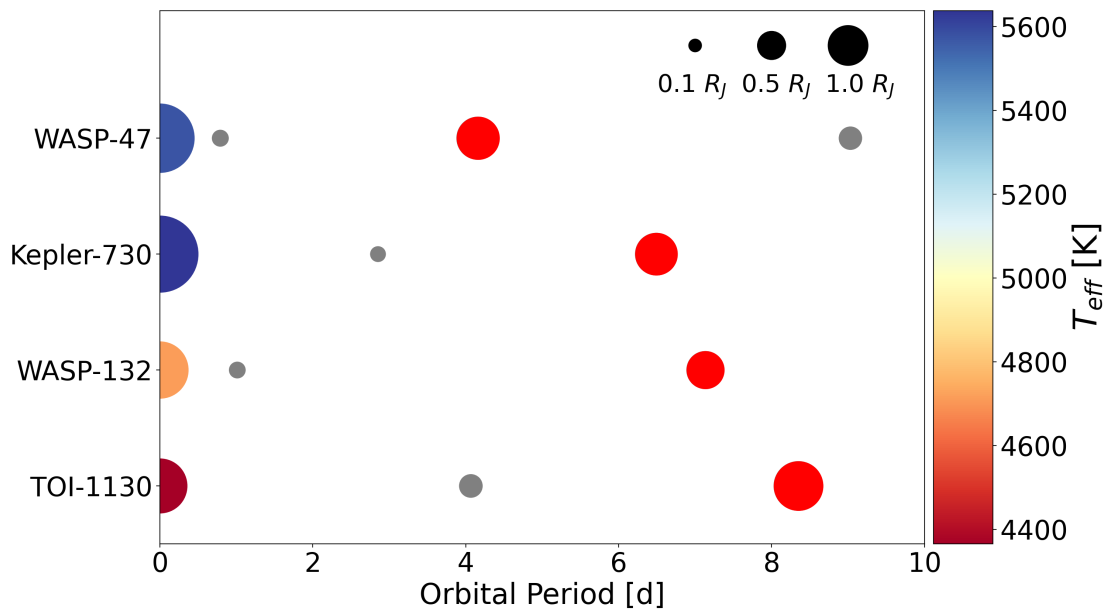

Figure 3.7: A schematic depiction of the four known systems with a hot Jupiter and at least one nearby companion planet (WASP-47, Kepler-730, TOI-1130, WASP-132). Orbital periods of the hot Jupiters increase from top to bottom. Sizes of circles for the planets are to scale with one another but not with distance from host star and host star radius. Likewise, circles for the host stars are to scale with one another but not with planets or orbital distance. Hot Jupiters are denoted by red circles, companion planets by gray circles, and the stellar hosts are colored based on their effective temperature.

3.8 Discussion

The discovery and validation of WASP-132 c places the WASP-132 system among only a handful of systems with nearby companions to a hot Jupiter. Prior to WASP-132, only WASP-47 (Becker et al., 2015), Kepler-730 (Cañas et al., 2019), and TOI-1130 (Huang et al., 2020a) were known to harbor a hot Jupiter with nearby companions. Figure 3.7 illustrates all of the currently known systems containing hot Jupiters with nearby companions. These four multi-planet systems are still consistent with occurrence rate estimates provided by both Huang et al. (2016), Zhu & Dong (2021), and Hord et al. (2021) which calculate $1.1^{+13.3}_{-1.1}\%$, $\sim 2\%$ ($<9.7\%$, 95% upper limit), and $7.3^{+15.2}_{-7.3}\%$ of hot Jupiters to have nearby companions, respectively.

3.8.1 Potential Formation Pathways

The existence of nearby companions in four hot Jupiter systems suggests a dynamically cooler formation mechanism than the high-eccentricity migration that is invoked to explain a significant fraction of hot Jupiters. Although TESS appears to be improving our understanding of the architecture of hot Jupiter systems – now with a second hot Jupiter companion discovery presented here – hot Jupiters with companions are still a rarity, comprising only a small percentage of the nearly 500 hot Jupiters currently confirmed. Few hot Jupiter systems have yet to been searched for companions to this level of sensitivity, though. This scarcity of hot Jupiters with nearby companions suggests that high-eccentricity formation scenarios may dominate the observed hot Jupiter population. However, there is increasing evidence that there must be a subpopulation of hot Jupiters that do not form via high-eccentricity migration. This is evidenced not only by the existence of hot Jupiters with nearby companions as presented here, but also statistical simulations and analytical calculations show that high-eccentricity migration alone cannot reproduce the observed hot Jupiter population and require a mechanism such as disk migration (Dawson et al., 2014; Anderson et al., 2016; Muñoz et al., 2016). Although disk migration could explain these handful of unique systems, it is also possible that a super-Earth could have managed to exceed the threshold mass for runaway gas accretion, forming the hot Jupiter and leaving intact any planets orbiting interior (Lee et al., 2014; Batygin et al., 2016; Huang et al., 2020a). It is worth noting that, to our current knowledge, none of the systems containing hot Jupiters and nearby companion planets possess exterior companions or companions on highly misaligned orbits, which are key observables of in-situ formation described by Batygin et al. (2016).

The subpopulation of hot Jupiters with companions that apparently did not undergo high-eccentricity migration may have more in common with warm Jupiters ($10 < P < 100$ d) than their fellow hot Jupiters in terms of formation. In contrast to hot Jupiters, $\sim$50% of warm Jupiters have nearby companion planets (Huang et al., 2016). Hot Jupiters with companions form a seemingly continuous period distribution with their warm Jupiter counterparts (Huang et al., 2020a) and may represent the tail end of a wider population spanning across the physically-unmotivated 10 d dividing line.

Taking, for instance, a definition of hot Jupiter based on equilibrium temperature where $T_{\rm eq}$ >1000 K defines a hot Jupiter (e.g. Miller & Fortney 2011; Thorngren & Fortney 2018) leaves only WASP-47 b and Kepler-730 b classified as hot Jupiters with $T_{\rm eq}$ of 1259 and 1219 K, respectively, with TOI-1130 b and WASP-132 b classified in a slightly lower "warm" range with $T_{\rm eq}$ of 637 and 763 K, respectively. This definition of hot Jupiters based on equilibrium temperature is equally arbitrary with respect to orbital properties, however, as it still fails to provide a clear distinction between hot Jupiter subpopulations that formed via different formation mechanisms. Systems from a potential "warm Jupiter tail," such as those discussed here, would inadvertently be included in this definition of hot Jupiters.

3.8.2 Investigating System Architectures

Comparing these unique systems to the overall exoplanet population (see Figure 3.8), it becomes apparent that three of the hot Jupiters with nearby companions have orbital periods that are longer than the typical hot Jupiter. The hot Jupiters with companions reside in a more sparsely-populated region of period-radius space farther from their host stars than most hot Jupiters. While this is notable, the sample of known hot Jupiters with nearby companions is currently too small

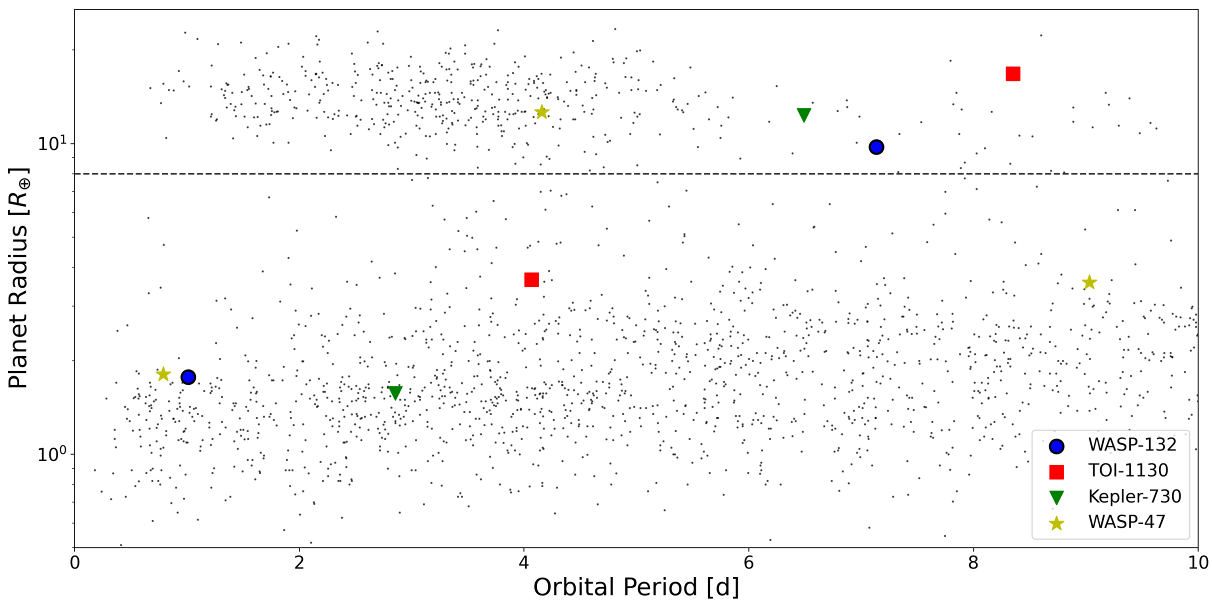

Figure 3.8: The period and radius of all planets in the four hot Jupiter systems with known companion planets (WASP-47, Kepler-730, TOI-1130, WASP-132) overlaid on the periods and radii of all planets contained on the NASA Exoplanet Archive. The larger, colored markers represent planets in one of these systems, with similar markers corresponding to planets in the same system. The markers for WASP-132 b and c are outlined in black. A dashed horizontal line has been included at $8R_\oplus$ to denote the division between hot Jupiters and smaller planets.

to determine if there is a correlation between the presence of a companion and the hot Jupiter orbital or physical properties (or host star type). Furthermore, the cluster of hot Jupiters around an orbital period of 2-3 days is dominated by transit detections, whereas hot Jupiters are quite common on 4-5 day orbits when considering only radial velocity discoveries. Further analysis is required to quantify the extent to which the hot Juiters with close companions are outliers in the period-radius space.

What we know today is that the known hot Jupiter nearby companions predominantly orbit interior to the hot Jupiter, so the hot Jupiter must orbit at a certain distance from the host star so that there is enough room in the system for a stable orbit of a smaller planet interior to the hot Jupiter. There is the notable exception of the WASP-47 system, which also has one exterior companion. Whether additional exterior transiting companions to hot Jupiters exist remains to be seen, especially given the fact that all of the currently known close companions have been discovered via transits, which are biased towards planets on shorter orbital periods. With the probability of transit dropping with increasing orbital period, the discovery of additional exterior transiting companions is more challenging. Constraints have been placed on the existence of nearby, non-transiting planets through the investigation of transit timing variations (TTVs) using *Kepler* data, with only WASP-148 c found (Steffen et al., 2012; Hébrard et al., 2020), supporting the idea that exterior companions are indeed perhaps intrinsically rarer than interior companions. Analysis of comprehensive transit timing searches using TESS data (such as that of Ivshina & Winn 2022) could provide updated constraints, however.

Simulations performed by Ogihara et al. (2013, 2014) have provided a possible explanation for the dearth of external companions. They show that the existence of super-Earths exterior to a hot Jupiter would drive the hot Jupiter into the host star. Therefore, any hot Jupiters with external planets would have been driven into the host star prior to their discovery, thus leading to the "crowding-out of giants by dwarfs", as Ogihara et al. (2013) refers to it.

In each of the previously known hot Jupiter systems with nearby companions, none of the planets are in orbital resonance with each other. The case is the same for WASP-132. A small fraction of *Kepler* multiplanet systems are in resonances (Lissauer et al., 2011), whereas wide-orbiting giant planets frequently are (Winn & Fabrycky, 2015). Expanding the sample of hot Jupiters with nearby companions would allow for the comparison of the period ratio distribution of hot Jupiters with nearby companions to other known exoplanet populations. Similar distributions of period ratios would be expected from populations of systems that were assembled in a similar manner, and comparing the period ratio distribution of hot Jupiters with companions and the occurrence of resonances to a population such as super-Earth systems could elucidate possible common formation mechanisms.

3.8.3 Prospects for Follow-Up

These hot Jupiters with companions provide a unique opportunity to test if spin-orbit misalignment is a consequence of high-eccentricity migration as theorized but none have yet had their misalignment measured. Based on the derived parameters of the host star and WASP-132 c, we estimate that the semi-amplitude of the Rossiter-McLaughlin effect for WASP-132 c is $\sim$0.5 m s^{-1} (assuming a v sin i $\sim$0.9 km s^{-1} as reported by Hellier et al. 2017). The estimated semi-amplitude of the hot Jupiter WASP-132 b is much larger at $\sim$17 m s^{-1}. Although the prospect of measuring the Rossiter-McLaughlin effect for WASP-132 c is quite low, that of WASP-132 b can easily be detected with current radial velocity precision and may inform our understanding of the orbital alignment with the host star's rotation. The WASP-132 system is otherwise amenable to additional follow-up observations as it is relatively bright at near-infrared wavelengths (K_{s} = 9.674).

Further radial velocity monitoring and a measured mass is necessary to confirm the planetary nature of this planet. Given that the expected semi-amplitude of WASP-132 c is between 3 and 6 ms^{-1}, an instrument more sensitive than CORALIE such as HARPS or PFS would be ideal to follow up on WASP-132 c to obtain a mass measurement and further characterize the system. Both of these instruments have 1 ms^{-1} sensitivity or better, making a detection of WASP-132 c with either instrument possible.

3.9 Summary

In this chapter, we present the discovery and validation of a companion planet orbiting interior to hot Jupiter WASP-132 b. Our investigation and results are summarized here:

1. A $\sim$1.01 d periodic signal with a false alarm probability $\ll 1\%$ was detected in the TESS photometric data for WASP-132 (TOI-822) with both the SPOC pipeline and the Transit Least Squares search algorithm. Neither the TESS SPOC pipeline nor the vetting software `DAVE` found any immediate false positive indicators.

2. We refined the system parameters, obtaining a host star of R_* = $0.753^{+0.028}_{-0.026}$ $R_\odot$ and M_* = 0.782 $\pm$ 0.034 $M_\odot$ and planets with periods and radii of 7.13 d and 10.05 $\pm$ 0.28 $R_\oplus$ for WASP-132 b and 1.01 d and 1.85 $\pm$ 0.10 $R_\oplus$ for WASP-132 c.

3. An analysis of archival CORALIE radial velocity measurements did not yield a significant

detection at the 1.01 d period, with a 3σ upper limit of 37.35 $M_{\oplus}$ on the mass of WASP-132 c.

4. Using LCOGT ground-based follow-up photometry, we ruled out NEB signals as the potential source of the TESS detection in stars out to $50''$ from the WASP-132 c, and likely ruled out potential NEB signals in stars out to $2\farcm5$

5. WASP-132 c is statistically validated as a planet with false positive probabilities (FPPs) of 9.02×10^{-5} and 0.0107 using `vespa` and `TRICERATOPS`, respectively (see Section 3.6.2 for further discussion).

6. The system is dynamically stable on timescales of 100 Myr for planetary and orbital parameters within 3σ of the best-fit values.

7. WASP-132 is the second system discovered by TESS (and one of only four systems in total) to contain a hot Jupiter with a nearby companion planet, suggesting that a mechanism other than high-eccentricity migration may play a significant role in the formation of hot Jupiters.

The discovery of WASP-132 c demonstrates the ability of TESS to not only find new planets but also enhance our knowledge of those already known. As TESS continues its almost-all-sky survey, it will surely reveal additional systems similar to WASP-132 which will improve our understanding of the evolution of hot Jupiter systems. With an ever-expanding census of hot Jupiters with nearby companion planets, it may even be possible to identify sub-populations of these hot, giant planets. It is imperative to continue the search for this type of system architecture as a larger data set will allow us to solidify our understanding of how these rare systems form.

Chapter 4: Validation of the Top TESS Objects of Interest for Atmospheric Characterization of Transiting Exoplanets with JWST

4.1 Overview

JWST has ushered in an era of unprecedented ability to characterize exoplanetary atmospheres. While there are over 5,000 confirmed planets, more than 4,000 TESS planet candidates are still unconfirmed and many of the best planets for atmospheric characterization may remain to be identified. We present a sample of targets that we identify as "best-in-class" for transmission and emission spectroscopy with JWST. These targets are sorted into bins across equilibrium temperature T_{eq} and planetary radius R_{p} and are ranked by transmission and emission spectroscopy metric (TSM and ESM, respectively) within each bin. In forming our target sample, we perform cuts for expected signal size and stellar brightness, to remove sub-optimal targets for JWST. Of the 194 targets in the resulting sample, 103 are unconfirmed TESS planet candidates, also known as TESS Objects of Interest (TOIs). We perform vetting and statistical validation analyses on these 103 targets to determine which are likely planets and which are likely false positives, incorporating ground-based follow up from the TESS Follow-up Observation Program (TFOP) to aid the vetting and validation process. We statistically validate 18 TOIs, marginally validate 38 TOIs to varying levels of confidence, deem 29 TOIs false positives, and leave the dispositions for 4 TOIs as inconclusive. 14 of the 103 TOIs were confirmed independently over the course of our analysis. We provide our final best-in-class sample as a community resource for future JWST proposals and observations. We intend for this work to motivate formal confirmation and mass measurements of each validated planet and encourage more detailed analysis of individual targets by the community.

4.2 Introduction

Since the first exoplanets were discovered by Wolszczan & Frail (1992b) and Mayor & Queloz (1995), over 5,000 exoplanets have been confirmed, opening up a wide array of planets of varying sizes, temperatures, and masses for study. The rate of exoplanet discovery has notably accelerated over time, originating with serendipitous or targeted observations and culminating in the concerted efforts of ground-based surveys such as the Wide Angle Search for Planets (WASP; Pollacco et al., 2006) and the Hungarian-made Automated Telescope Network (HATNet; Bakos et al., 2004) and space-based observatories such as the COnvection, ROtation and planetary Transits satellite (CoRoT; Auvergne et al., 2009; Moutou et al., 2013), Kepler (Borucki et al., 2010), K2 (Howell et al., 2014), and the Transiting Exoplanet Survey Satellite (TESS, Ricker et al. 2015).

Although the exoplanet discovery process can reveal important properties of planets like mass and equilibrium temperature, further observations and analysis are required to understand the conditions on the planets themselves and examine the planet's atmospheric composition and dynamics. The first observation of an exoplanetary atmosphere was conducted by Charbonneau et al. (2002b), and since then, in a parallel to the diversity of the types of exoplanets, spectroscopic characterization has revealed a wide variety of atmospheric compositions and aerosol properties as well (e.g., Sing et al., 2016; Welbanks et al., 2019; Mansfield et al., 2021; Changeat et al., 2022; August et al., 2023).

Transmission and emission spectroscopy have proven to be the workhorses of exoplanetary atmospheric characterization. These methods utilize the absorption of stellar flux transmitted through the exoplanetary atmosphere and the thermal emission from the exoplanet as seen through secondary eclipse to probe the atmospheric characteristics of the planet. Exoplanet atmospheric characterization and spectral modeling have greatly expanded our understanding of the formation and evolution of planets, the physical and chemical processes that shape planetary atmospheres, and atmospheric aerosol properties (e.g. Madhusudhan, 2019; Mollière et al., 2022; Wordsworth & Kreidberg, 2022) as well as the range of diverse conditions within each of these individual topics. As the outermost layer of a planet, the atmosphere is the easiest component of an exoplanet to probe in detail and can be used to infer other planetary properties.

Although space- and ground-based resources for atmospheric characterization have become more abundant since the first transmission spectrum was taken, these resources remain in high demand. The premier atmospheric characterization tools have largely been the Hubble Space Telescope and, until its retirement in 2020, the Spitzer Space Telescope, both of which have historically been heavily oversubscribed. High-resolution spectrographs on ground-based telescopes have become increasingly important in the study of exoplanet atmospheres, but these are often limited by what's visible in the night sky and the signal-to-noise ratios achievable.

The highly anticipated JWST launched in 2021 (Gardner et al., 2006, 2023), with promises of greatly improved capabilities for exoplanet atmospheric characterization (e.g. Deming et al., 2009; Greene et al., 2016; Stevenson et al., 2016), owing to its large aperture and infrared (IR) instrument complement. Although still early in its mission, JWST has already begun delivering on these promises with its first year of exoplanet results (e.g. Tsai et al., 2023; Ahrer et al., 2023; Greene et al., 2023; Kempton et al., 2023). But time on JWST is in high demand, and this, coupled with the review process for general observer programs, has resulted so far in a patchwork of exoplanet atmospheric observations.

When it comes to identifying targets for atmospheric characterization observations, there is a critical synergy between JWST and TESS. Touted from the very beginning as a "finder scope for JWST," the almost-all sky survey strategy of TESS was intended to find a myriad of new planets around bright, nearby stars that would be amenable to atmospheric characterization with JWST, in contrast to the dimmer, more distant host stars of Kepler planetary systems. So far, TESS has discovered more than 300 confirmed planets, with more than 4,000 planet candidates classified as unconfirmed TOIss. There is currently no published false positive rate for TESS and it is possible that many of these 4,000 TOIs may be false positives. However, if even a fraction of them are true planets, this would dramatically grow the sample of planets whose atmospheres may be well-suited to observe and characterize with JWST.

In fact, some of the highest quality (i.e. highest signal-to-noise) atmospheric characterization targets likely still lie among the unconfirmed TOIs list, since TESS has unique capabilities for finding small planets orbiting bright stars in particular. The JWST-TESS synergy is demonstrated especially by the fact that $\sim$37% of JWST Cycle 1 targets and $\sim$56% of JWST Cycle 2 targets are TESS discoveries. With JWST already flying, it is of the utmost importance to systematically and expeditiously identify the best JWST targets to provide a uniform coverage of parameter space.

In an effort to better streamline use of JWST for atmospheric characterization and identify which targets are likely to exhibit the most clearly detectable features in their atmospheric spectra, we present a set of "best-in-class" targets for transmission and emission spectroscopy. Our best-in-class sample consists of the targets ranked in the top five according to the TSM and ESM from Kempton et al. (2018) within each cell of a grid spanning the $R_{\rm p}$-$T_{\rm eq}$ space, which is described in Section 4.3. $R_{\rm p}$-$T_{\rm eq}$ axes were chosen since radius is expected to be a loose proxy for metallicity (Baraffe et al., 1998; Fortney et al., 2013) while temperature correlates to chemistry and aerosol formation (Gao et al., 2020). We account for the technical capabilities of JWST's instruments through the inclusion and calculation of various additional metrics (e.g. stellar host magnitude, expected atmospheric signal size, and observability metrics benchmarked against JWST's instrumental capabilities) for each target and further incorporate these values into our rankings, thus tuning our best-in-class sample to JWST specifically.

In our rankings, we initially make no distinction between confirmed planets and unconfirmed TOIs in order to assess how the TESS planet candidates fit in with the overall sample and to identify which TOIs might displace known planets as best-in-class atmospheric characterization targets. For each unconfirmed TOIs on our best-in-class list, we perform cursory vetting and statistical validation analyses to determine which targets are obvious false positives and which are worthy of additional follow up prior to future atmospheric characterization observations with JWST. We note that while we only statistically "validate" planets rather than label them as "confirmed", we consider them to be planets for the purposes of our best-in-class sample. Our aim is to produce a sample of planets (or likely planets) that are well-suited for JWST atmospheric characterization to serve as a community resource for upcoming JWST proposal cycles and future observing programs aimed at regions of planetary parameter space where the highest SNR targets have yet to be identified.

In Section 4.3, we outline our methodology for obtaining our best-in-class sample including the data origin, the metrics calculated, and the specific boundaries in parameter space that were used when defining each class of planets. In Section 4.4, we describe the follow-up observations obtained to aid in our vetting and validation analyses of each unconfirmed TOI contained in our best-in-class sample. Section 4.5 details our vetting procedures, the follow-up and independent resources that were used in our consideration of false positive scenarios for each unconfirmed TOI, and the criteria against which each target was compared. Section 4.6 walks through our statistical validation procedures including our implementation of statistical validation softwares and the disposition categories that we sorted each unconfirmed TOI into based on the results of our vetting and validation analyses. In Section 4.7 we summarize the results of our vetting and statistical validation including which unconfirmed TOIs were statistically validated and which we considered a false positive. Our findings are summarized in Section 4.8.

4.3 Grid Generation

Identifying targets across $R_{\rm p}$-$T_{\rm eq}$ space that are well-suited to atmospheric characterization with JWST is critical to our understanding of exoplanet atmospheres. By sampling across this parameter space, we expect to cover a range of metallicities as well as atmospheric chemistry and aerosol regimes that would allow us to tease out trends and test models on the population level. This could include a mass-metallicity relation, an aerosol-$T_{\rm eq}$ relation, or a transition between planets that have CO vs. CH_4 in their atmospheres as the dominant carbon carrier. To accomplish this, we've divided up the $R_{\rm p}$-$T_{\rm eq}$ parameter space into a grid, sorted each planet and planet candidate into cells within this grid, and ranked each target according to its expected signal-to-noise ratio approximated via its TSM or ESM. The samples for both transmission and emission spectroscopy can be found in Figure 4.1 and a visual outline of our sample generation is shown in the top box of Figure 4.2.

4.3.1 Provenance of Sample Parameters and TSM & ESM Calculation

In order to obtain a standardized list of planets and planet candidates to consider when determining which are the best-in-class for atmospheric characterization with JWST, we relied on the data tables maintained by the NASA Exoplanet Archive[1] and the parameter values contained therein. The Exoplanet Archive collates parameter sets for confirmed and unconfirmed planets and acts as a single repository for published parameter values for each target. For the confirmed planets, we downloaded the Planetary Systems table which contains every planet that has a published validation or confirmation and the accompanying set of parameter values with a single parameter set labeled as the default by the archive staff for each planet. For the unconfirmed TOIs, we downloaded the TESS Candidates table from the Exoplanet Archive, which updates directly from the TESS TOI Catalog (Guerrero et al., 2021) with new targets and refined parameter values from the TESS mission. These two tables were both downloaded on November 3, 2022.

We elected to use the parameter set denoted as the default set of values for each of the planets in the Planetary Systems table throughout our analysis. In the case that the default parameter set was incomplete and missing values for critical parameters necessary to our analysis, values were pulled from other, non-default parameter sets for each planet, if they existed. Values with lower uncertainties from other parameter sets were given priority for inclusion in the final parameter set.

[1] https://exoplanetarchive.ipac.caltech.edu/

We calculated the TSM and ESM for each planet according to the prescription outlined in Kempton et al. (2018), specifically equations 1 and 4. The calculation of TSM and ESM assume cloud-free atmospheres, solar composition for planets larger than 1.5 $R_\oplus$, and a pure H_2O steam atmosphere for planets smaller than 1.5 $R_\oplus$. These two values represent analytical metrics that quantify the expected signal-to-noise in transmission and thermal emission spectroscopy for a given planet and can be used to identify which planets are best-suited for atmospheric characterization with JWST relative to one another. We maintained two separate samples for best-in-class targets: one for transmission spectroscopy driven by TSM and the other for emission spectroscopy driven by ESM. Both of these initially started with the same overall sample of planets and planet candidates downloaded from the Exoplanet Archive and were each shaped by the observational constraints unique to each respective sample. Figure 4.3 illustrates the parameter space coverage of our combined best-in-class samples.

Even after pulling values from other parameter sets, some targets did not contain finite values for all of the parameters necessary to calculate the spectroscopy metrics and the observability criteria with which we defined and ranked our sample. For targets without a value for the ratio between semi-major axis and stellar radius, a/R_*, we converted both the semi-major axis a and the stellar radius R_* to units of meters and took the ratio of the two. In the case that a was missing but a/R_* was a finite value, a/R_* was multiplied by R_* to calculate a. A similar procedure was performed for the ratio between the planet and stellar radii, R_p/R_*. We preferred to use the reported ratios if they existed to reduce the propogation of potential errors in generating these ratios from the reported values of their individual components. Reported mass and equilibrium temperature values were used when reported, but were calculated later in the procedure if unavailable. All targets that still lacked full parameter sets to perform the necessary calculations were removed from the sample. We checked each parameter set to ensure that $R_p/R_* < 1$ and targets with values that did not conform to this criterion were replaced with a value from another parameter set, if available.

We calculated the masses of the planets from the Planetary Systems table and candidates from the TOI list that did not have published masses using a mass-radius distribution adapted from the mean of the Chen & Kipping (2017) mass-radius distribution. Specifically, we set the S^3 coefficient to be 0.01 rather than -0.044, to ensure that each radius value corresponded to a unique mass, while minimally affecting the shape of the curve. We used this distribution up to planetary radii of 15 $R_\oplus$, fixing the mass of planets larger than this threshold to 1 M_{Jup}. Above this radius, the scatter of the mass-radius distribution is large and results in a mean that is nearly constant in mass across radius. This is the same procedure that is used by the Exoplanet Archive to calculate expected masses. We divided the sample into three categories: confirmed planets with $> 5\sigma$ mass measurements, planets marked as confirmed on the Exoplanet Archive with $< 5\sigma$ mass measurements, and unconfirmed planet candidates without any mass measurement. (Batalha et al., 2019) showed that different mass confidence levels result in different precision with which an exoplanet's atmosphere can be characterized. A stratification of these targets based on mass measurement will also allow the community to better prioritize follow up resources for the best-in-class targets and allowed us to identify which targets are unconfirmed and in need of statistical validation.

Additionally, we calculated the mass of the host star for each TOI based on the star's log g and radius because stellar mass is not included in the Exoplanet Archive's TOI table. We then calculated the equilibrium temperatures $T_{\rm eq}$ of each planet – both TOI and confirmed – according to Equation 3 of Kempton et al. (2018). This was done to ensure a uniform data set for T_{eq} since the definition of equilibrium temperature varies with each data set on the Exoplanet Archive, with different assumptions regarding surface albedo and atmospheric heat distribution serving as variables with no set standard. Since T_{eq} is integral to our determination of the best targets for transmission and emission spectroscopy, we elected to calculate the value for each planet and planet candidate to ensure a uniform comparison. Our calculation of T_{eq} assumes zero albedo and full day-night heat redistribution.

4.3.2 Observability Cuts

While useful for relative comparisons between targets, the TSM and ESM only predict the signal to noise but do not account for other observability considerations such as the absolute signal size relative to the instrumental noise floor or the target being within an instrument's brightness limits. To incorporate the observability of our sample with JWST into our best-in-class rankings, we also calculated the expected sizes of transmission spectral features and secondary eclipse depth for transmission and emission spectroscopy, respectively.

4.3.2.1 Observability in Transmission

We again follow the prescription outlined in Kempton et al. (2018), expressing the size of expected spectral features at one scale height as

$$\frac{2R_p}{R_*^2} \times \frac{kT_{eq}}{\mu g} \tag{4.1}$$

where R_{p} is the planetary radius, R_* is the radius of the host star, k is the Boltzmann constant, T_{eq} is the equilibrium temperature of the planet, μ is the mean molecular weight of the atmosphere, and g is the surface gravity of the planet. For planets with $R_{\mathrm{p}} > 1.5$ $\mathrm{R}_{\oplus}$, we assume μ = 2.3 (in units of proton mass) while for planets with $R_{\mathrm{p}} < 1.5$ $\mathrm{R}_{\oplus}$, we assume μ = 18, following the assumption that all planets in a given size bin have the same atmospheric composition as made by Louie et al. (2018). We calculated g using the expression g=$GM_{\mathrm{p}}/R_{\mathrm{p}}^2$ where G is the gravitational constant and M_{p} and R_{p} are the mass and radius of the planet, respectively. The second term of Equation 4.1 represents the scale height of the planetary atmosphere, H.

We assumed a depth of $2H$ when calculating expected spectral feature size based off of the spread in the sizes of H_2O features observed using the Hubble Space Telescope's NIR WFC3 instrument (Stevenson, 2016). The average size of these features was reported to be $\sim 1.5H$, but at longer wavelengths such as those probed by JWST, the size of spectral features for molecules increases, so we elected to assume a depth slightly above the average reported by Stevenson (2016). Assuming a larger expected spectral feature also allows for our sample to capture more planets to compare between within our sample as well as to account for differences in cloud cover or the mean molecular weight of exoplanet atmospheres.

In fact, for all constraints applied to our sample, we chose liberal thresholds in order to allow for more targets to appear in our best-in-class sample, especially in parameter spaces where there otherwise would be no promising targets. This was done not only for illustrative purposes, but to attempt to account for some of the variance in parameters governing exoplanet atmospheres and potentially improved observational capabilities going forward.

To ensure that all best-in-class targets would be observable with JWST, we imposed a requirement for a 2σ spectral signal size assuming a noise floor of 10 ppm for the NIRCam, NIRISS, and NIRSpec instruments on JWST. These instruments are all ideal for transmission spectroscopy since their wavelength coverage overlaps prominent transmission spectral features.

We note the TSM was benchmarked for use with NIRISS (Kempton et al., 2018).

4.3.2.2 Observability in Emission

We perform a similar procedure for the secondary eclipse depth in order to determine which targets are amenable for emission spectroscopy with the MIRI instrument onboard JWST. The expected secondary eclipse depth can be estimated using the expression

$$\frac{B_{7.5}(T_{day})}{B_{7.5}(T_*)} \times \left(\frac{R_p}{R_*}\right)^2 \tag{4.2}$$

where $B_{7.5}$ is the Planck function evaluated for a given temperature at a representative wavelength of 7.5 μm, $T_{\rm day}$ is the dayside temperature in Kelvin of the planet as calculated by $1.1 \times T_{\rm eq}$, T_* is the effective temperature of the host star, and $R_{\rm p}/R_*$ is the ratio of the planetary and stellar radii. We calculate the dayside temperature as $1.1 \times T_{\rm eq}$ to account for the dayside hotspot on the planet, following the analysis by Kempton et al. (2018) that tuned this relation according to a suite of global circulation and 1D atmospheric models. The 7.5 μm was chosen as the representative wavelength since it is the center of the "conservative" MIRI LRS bandpass on JWST as data beyond 10 μm are often unreliable (Bell et al., 2023; Kempton et al., 2023) and 7.5 μm is still near the peak of the MIRI LRS response function (Rieke et al., 2015; Kendrew et al., 2015). We imposed a requirement that the secondary eclipse depth be measurable to the 3σ level assuming a noise floor of 20 ppm for the MIRI instrument on JWST. There were more small planets contained within the emission spectroscopy sample and so we were able to adopt a more conservative 3σ threshold rather than the 2σ threshold applied to the transmission spectroscopy sample. We also imposed an ESM > 3 requirement on our emission spectroscopy sample to remove targets that would produce small secondary eclipses even under ideal observing conditions with JWST. Like TSM with NIRISS, ESM was benchmarked for use with MIRI and MIRI is ideal for emission spectroscopy among JWST's instruments thanks to its longer wavelength coverage.

We applied additional observability cuts to the sample to ensure that each of our best-in-class targets would be observable by JWST and would produce significant spectral detections. For transmission spectroscopy targets, we restricted the J magnitude of the host star to $>$ 6.0 while for emission spectroscopy targets, we restricted the K magnitude of the host stars to $>$ 6.4. These values represent the approximate maximum brightnesses at which the NIRCam long-wavelength channel grism spectroscopy (which can observe the brightest stars of the near-infrared spectroscopic modes, Beichman et al., 2014) and MIRI Low Resolution Spectroscopy (LRS, Kendrew et al., 2016) modes will not saturate, respectively, according to v2.0 of the JWST exposure time calculator (Pontoppidan et al., 2016). We also removed any planets or planet candidates with impact parameter $b >$ 0.9 to remove grazing transits that could produce unreliable transit depths.

We then divided our full sample of targets that are observable with JWST into bins of planetary radius and equilibrium temperature to determine which targets are best for atmospheric characterization in their class. This division included both confirmed planets and unconfirmed planet candidates. The edges of these bins in planetary radius were chosen in order to match the cutoffs used in Kempton et al. (2018), setting the minimum and maximum radii to include the smallest and largest transiting planets at the time the Exoplanet Archive was queried. The temperature bin edges were chosen to capture the ultra-hot Jupiters at $T_{eq} >$ 2250 K, the carbon equilibrium chemistry transition from CO (and CO_2) to CH_4 around 800 K (assuming an otherwise solar C/O ratio, Fortney et al., 2013), and roughly equal spacing otherwise. The coldest temperature bin in our sample was chosen to encompass the habitable zone.

4.3.3 Description of Best-in-Class Grids

The planets contained within each bin in radius and temperature space were then sorted and ranked by TSM and ESM for the transmission spectroscopy and emission spectroscopy samples, respectively. This ranking was performed agnostic to confirmation status and the existence of a well-constrained mass, resulting in a combination of confirmed planets and unconfirmed planet candidates mixed together within grid cells. The top five targets in each bin are considered the best-in-class for that portion of parameter space. Our rankings of the transmission and emission spectroscopy targets are contained within the grids shown in Figure 4.1.

Almost every bin for both the transmission and emission target samples has at least one unconfirmed planet candidate contained within it, with most bins dominated by unconfirmed candidates. While certainly not all of the planet candidates are true planets, if even a fraction of the them are, these rankings indicate that there is a large number of TESS planet candidates that are both (i) among the best currently known targets for atmospheric characterization with JWST from a SNR perspective; and (ii) required to provide a uniform coverage of the $R_{\rm p}$-$T_{\rm eq}$ space.

4.4 Follow-up Observations

In order to determine which of the TESS-discovered planet candidates in our best-in-class samples are true planets, we first collated all of the follow-up observations for each target. These follow-up observations provided valuable, independent information on the validity of each planet candidate as true planets. We worked closely with TFOP[2] subgroups (SGs) to compile available photometric, spectroscopic, and imaging follow-up observations for each target. These observa-

[2] https://tess.mit.edu/followup

tions were used in initial vetting to determine whether each target was an obvious false positive or if it could proceed to more in-depth vetting and validation. TFOP follow-up observations and the constraints that they impose on the system were incorporated into our vetting and statistical validation procedures where possible (see Sections 4.5 & 4.6). The follow-up resources used in vetting and validating the best-in-class planet candidates are summarized here with a representative sample of the specific observations used for individual targets detailed in Table **??** located in Appendix **??** and a full, machine-readable version available from the online version of this article. An outline of where follow-up observations were used in our vetting procedures can be found in the middle panel of Figure 4.2.

4.4.1 Ground-based Photometry

TFOP's Sub Group 1 (SG1; Collins, 2019) performed ground-based photometry for almost all of the targets in our best-in-class samples in order to clear the background fields of eclipsing binaries (EBs), to check if the candidate transit signal could be identified as on target, and to check the chromaticity of the targets themselves. This ground-based photometry was taken by a variety of observatories over a span of multiple years. The `TESS Transit Finder`, which is a customized version of the `Tapir` software package (Jensen, 2013), was used to schedule the transit follow-up observations included here. Below we detail the observatories, instruments, and data reduction methods used to obtain the ground-based photometry for our samples. Unless otherwise noted, all image data were calibrated and photometric data were extracted using `AstroImageJ` (Collins et al., 2017). Further discussion on the use of ground-based photometry in vetting and validation can be found in Sections 4.5.3 & 4.6.

4.4.1.1 LCOGT

The Las Cumbres Observatory Global Telescope (LCOGT; Brown et al., 2013a) 2.0 m, 1.0 m and 0.4 m network nodes are located at Cerro Tololo Inter-American Observatory in Chile (CTIO), Siding Spring Observatory near Coonabarabran, Australia (SSO), South Africa Astronomical Observatory near Cape Town South Africa (SAAO), Teide Observatory on the island of Tenerife (TEID), McDonald Observatory near Fort Davis, Texas, United States (McD), and Haleakala Observatory on Maui, Hawai'i (HAI). The MuSCAT3 multi-band imager (Narita et al., 2020) is installed on the LCOGT 2 m Faulkes Telescope North at Haleakala Observatory. The 1 m telescopes are located at all nodes except Haleakala and are equipped with 4096×4096 SINISTRO cameras having an image scale of $0\farcs389$ per pixel, resulting in a $26' \times 26'$ field of view. The 0.4 m telescopes are located at all nodes and are equipped with 2048×3072 pixel SBIG STX6303 cameras having an image scale of $0\farcs57$ pixel^{-1}, resulting in a $19' \times 29'$ field of view. All LCOGT images were calibrated by the standard LCOGT `BANZAI` pipeline (McCully et al., 2018), and differential photometric data were extracted using `AstroImageJ` (Collins et al., 2017).

4.4.1.2 MuSCAT

The MuSCAT (Multicolor Simultaneous Camera for studying Atmospheres of Transiting exoplanets; Narita et al., 2015) multi-color imager is installed at the 1.88 m telescope of the National Astronomical Observatory of Japan (NAOJ) in Okayama, Japan. MuSCAT is equipped with three detectors for the Sloan g', Sloan i', and Pan-STARRS z-short band (z-short). The image scale is $\farcs358$ per pixel resulting in a in a $6.1' \times 6.1'$ field of view. MuSCAT data were extracted using the custom pipeline described in (Fukui et al., 2011).

4.4.1.3 MuSCAT2

The MuSCAT2 multi-color imager (Narita et al., 2019) is installed at the 1.52 m Telescopio Carlos Sanchez (TCS) in the Teide Observatory, Spain. MuSCAT2 observes simultaneously in Sloan g', Sloan r', Sloan i', and z-short. The image scale is $''\!.44$ per pixel resulting in a in a $7.4' \times 7.4'$ field of view. The photometry was carried out using standard aperture photometry calibration and reduction steps with a dedicated MuSCAT2 photometry pipeline, as described in Parviainen et al. (2019).

4.4.1.4 MEarth-S

MEarth-South (Irwin et al., 2007) consists of eight 0.4 m telescopes and observes from Cerro Tololo Inter-American Observatory, east of La Serena, Chile. Each telescope uses an Apogee U230 detector with a $29' \times 29'$ field of view and an image scale of 0.84" per pixel. Results were extracted using the custom pipelines described in Irwin et al. (2007).

4.4.1.5 El Sauce

The Evans 0.51 m telescope is located at the El Sauce Observatory in Coquimbo Province, Chile. The telescope is equipped with a 1536×1024 pixel SBIG STT-1603-3 detector. The image scale is $1''\!.77$ per 2×2 binned pixel resulting in an $18.8' \times 12.5'$ field of view.

4.4.1.6 Deep Sky West

Deep Sky West is an Observatory in Rowe, NM. The 0.5 m telescope is equipped with a Apogee U16M detector that has a image scale of $1\farcs09$ pixel^{-1} resulting in a $37' \times 37'$ field of view.

4.4.1.7 Dragonfly

The Dragonfly Telephoto Array is a remote telescope consisting of an array of small telephoto lenses roughly equivalent to a 1.0 m refractor housed at the New Mexico Skies telescope hosting facility, near Mayhill, New Mexico, USA. Dragonfly uses SBIG STF8300M detectors that have an image scale of $2\farcs85$ pixel^{-1}, resulting in a $156' \times 114'$ field of view. The data were reduced and analyzed with a custom differential aperture photometry pipeline designed for multi-camera image processing and analysis.

4.4.1.8 SUTO-Otivar

The Silesian University of Technology Observatory (SUTO-Otivar) is an Observatory near Motril, Spain. The 0.3 m telescope is equipped with a ZWO ASI 1600MM detector that has a image scale of $0\farcs685$ pixel^{-1}, resulting in a $18' \times 13'$ field of view.

4.4.1.9 Wellesley College Whitin Observatory

The Whitin observatory is a 0.7 m telescope in Wellesley, MA. The 2048×2048 FLI Pro-Line PL23042 detector has an image scale $0\farcs68$pixel^{-1}, resulting in a $23\farcm2 \times 23\farcm2$ field of view.

4.4.1.10 Adams Observatory

Adams Observatory is located at Austin College in Sherman, TX. The 0.6 m telescope is equipped with a FLI ProLine detector that has a image scale of $0\farcs38$ pixel^{-1}, resulting in a $26' \times 26'$ field of view.

4.4.1.11 OAUV-TURIA2

The Observatori Astronòmic de la Universitat de València (OAUV) is located near Madrid, Spain. The 0.3 m telescope is equipped with a FLI ProLine PL16803 detector that has a image scale of $0\farcs38$ pixel^{-1}, resulting in a $26' \times 26'$ field of view.

4.4.1.12 Lewin Observatory

The Maury Lewin Astronomical Observatory is located in Glendora, CA. The 0.35 m telescope is equipped with a SBIG STF8300M detector that has a image scale of $0\farcs84$ pixel^{-1}, resulting in a $23' \times 17'$ field of view.

4.4.1.13 ASP

The Acton Sky Portal private observatory is in Acton, MA, USA. The 0.36 m telescope is equipped with an SBIG ST-8300M camera having an image scale of $1\farcs79$ pixel^{-1}, resulting in a $1.67 \times 1.26\,\mathrm{deg}$ field of view.

4.4.1.14 WCO

The Waffelow Creek Observatory (WCO) is located in Nacogdoches, TX. The 0.35 m telescope is equipped with a SBIG STXL-6303E detector that has a image scale of $0\farcs66$ pixel^{-1}, resulting in a $34' \times 23'$ field of view.

4.4.1.15 PvDKO

The Peter van de Kamp Observatory is located atop the Science Center at Swarthmore College in Swarthmore, PA. The 0.24 m telescope has a QHY600 CMOS camera, which yields a $26' \times 17'$ field of view.

4.4.1.16 TRAPPIST

The TRAnsiting Planets and PlanetesImals Small Telescope (TRAPPIST) North 0.6 m telescope is located at Oukaimeden Observatory in Morocco and TRAPPIST-South 0.6 m telescope is located at La Silla Observatory in Coquimbo, Chile (Jehin et al., 2011). TRAPPIST North is equipped with an Andor IKONL BEX2 DD camera that has an image scale of $0\farcs6$ per pixel, resulting in a $20' \times 20'$ field of view. TRAPPIST South is equipped with a FLI camera that has an image scale of $0\farcs6$ per pixel, resulting in a $22' \times 22'$ field of view. The image data were calibrated and photometric data were extracted using either `AstroImageJ` or a dedicated pipeline that uses the `prose` framework described in Garcia et al. (2022).

4.4.1.17 ExTrA

The Exoplanets in Transits and their Atmospheres (ExTrA) is cited at the La Silla Observatory near La Higuera, Chile and consists of an array of three 0.6 m telescopes. Image data were calibrated and photometric data were extracted using a custom pipeline described in Bonfils et al. (2015).

4.4.1.18 SPECULOOS-S

The SPECULOOS Southern Observatory consists of four 1 m telescopes at the Paranal Observatory near Cerro Paranal, Chile. (Jehin et al. 2018). The telescopes are equipped with detectors that have an image scale of $0\farcs35$ per pixel, resulting in a $12' \times 12'$ field of view. The image data were calibrated and photometric data were extracted using a dedicated pipeline described in Sebastian et al. (2020).

4.4.1.19 SAINT-EX

The SAINT-EX Observatory is located in San Pedro Mártir, Mexico. The 1.0 m telescope is equipped with a Andor detector that has an image scale of $0\farcs34$ per pixel, resulting in a $12' \times 12'$ field of view. The image data were calibrated and photometric data were extracted using the SAINT-EX automatic reduction and photometry pipeline (PRINCE; Demory et al., 2020).

4.4.1.20 CHAT

The 0.7 m Chilean-Hungarian Automated Telescope (CHAT) telescope is located at Las Campanas Observatory, in Atacama, Chile. Image calibration and photometric data were extract using standard calibration and reduction steps and extracted using a custom pipeline which implements bias, dark, and flat-field corrections.

4.4.1.21 Observatori Astronòmic Albanyà

The Observatori Astronòmic Albanyà (OAA) is located in Albanyà, Girona Spain. The 0.4 m telescope is equipped with a Moravian G4-9000 camera that has an image scale of $1\farcs44$ per 2×2 binned pixel resulting in an $36' \times 36'$ field of view.

4.4.1.22 Lookout Observatory

The Lookout Observatory is located in Colorado Springs, CO. The 0.5 m telescope is equipped with a ZWO ASI1600MM Pro CMOS detector that has a image scale of $1\farcs46$ pixel^{-1}, resulting in a $152' \times 101'$ field of view. The image data were calibrated and photometric data were extracted using the reduction and photometry pipeline described in Thomas & Paczkowski (2021).

4.4.1.23 Brierfield Private Observatory

The Brierfield Observatory is located near Bowral, N.S.W., Australia. The 0.36 m telescope is equipped with a 4096×4096 Moravian 16803 camera with an image scale of $0\farcs74$ pixel^{-1}, resulting in a $50' \times 50'$ field of view.

4.4.1.24 Caucasian Mountain Observatory

The Caucasian Mountain Observatory (CMO SAI MSU) is a 2.5ṁ telescope located near Kislovodsk, Russia (Abraham & van Dokkum, 2014). The ASTRONIRCAM detector has an image scale of $''.18$ pixel^{-1}, resulting in a $4.6' \times 4.6'$ field of view.

4.4.1.25 Observatory de Ca l'Ou

Observatori de Ca l'Ou (CALOU) is a private observatory in Sant Martí Sesgueioles, near Barcelona Spain. The 0.4 m telescope is equipped with a 1024×1024 pixel FLI PL1001 camera having an image scale of $1''.14$ pixel^{-1}, resulting in a $21' \times 21'$ field of view.

4.4.1.26 Privat Observatory Herges-Hallenberg

The Privat Observatory Herges-Hallenberg is a 0.28 m telescope near Steinbach-Hallenberg, Germany. It is equipped with a Moravian Instrument G2-1600 detector that has an image scale of $1''.02$ pixel^{-1}, resulting an a $27' \times 41'$ field of view.

4.4.1.27 Catania Astrophysical Observatory

The 0.91 m telescope at Catania Astrophysical Observatory is located in Catania, Italy. The custom built 1024×1024 detector uses a KAF1001E CCD with an image scale of $0''.66$ pixel^{-1}, resulting in a $11'.2 \times 11'.2$ field of view.

4.4.1.28 Campo Catino Astronomical Observatory

The Campo Catino Astronomical Observatory houses a 0.43 m telescope and is located in Siding Spring, Australia. It is equipped with a FLI ProLine PL4710 detector that has an image scale of $0\farcs92$ pixel^{-1}, resulting an a $15.5' \times 15.5'$ field of view.

4.4.1.29 RCO

The 0.4 m RCO telescope is located at the Grand-Pra Observatory in Valais Sion, Switzerland. The telescope is equipped with a FLI 4710 detector with an image scale of $0\farcs73$ pixel^{-1}, resulting in a $12.9\farcm2 \times 12.55\farcm2$ field of view.

4.4.1.30 CROW Observatory

The 0.36 m telescope CROW Observatory is located in Portalegre, Portugal. It is equipped with a SBIG ST-10XME (KAF3200ME) detector that has an image scale of $0\farcs66$ pixel^{-1}, resulting an a $24' \times 17'$ field of view.

4.4.1.31 MASTER-Ural

The Kourovka observatory of Ural Federal University houses two 0.4 m MASTER-Ural telescopes near Yekaterinburg, Russia. Each telescope is equipped with an Apogee ALTA U16M detector with an image scale of $1\farcs85$ pixel^{-1}, resulting an a $120' \times 120'$ field of view. The image data were calibrated and photometric data were extracted using the reduction and photometry pipeline described in Lipunov et al. (2012).

4.4.1.32 Kutztown University Observatory

The 0.6 m telescope at Kutztown University Observatory is located near Kutztown, PA. The SBIG STXL-6303E detector has an image scale of $0''.76$ per 2×2 binned pixel, resulting in an $13' \times 19.6'$ field of view.

4.4.1.33 Union College Observatory

The Union College observatory houses a 0.51 m telescope and is located in Schenectady, New York. The SBIG STXL detector has an image scale of $0''.93$ per 2×2 binned pixel, resulting in an $30' \times 20'$ field of view.

4.4.1.34 George Mason University

The George Mason University 0.8 m telescope near Fairfax, VA. The telescope is equipped with a 4096×4096 SBIG-16803 camera having an image scale of $0''.35$ pixel^{-1}, resulting in a $23' \times 23'$ field of view.

4.4.1.35 Mount Kent Observatory

The Mount Kent Observatory houses a 0.51 m telescope and is located in Toowoomba, Australia. The Apogee Alta U16 (KAF-16803) has an image scale of $0''.35$ pixel^{-1}, resulting in a $23' \times 23'$ field of view.

4.4.1.36 Mt. Stuart Observatory

The Mt. Stuart Observatory near Dunedin, New Zealand. The 0.32 m telescope is equipped with a 3072×2048 SBIG STXL6303E camera with an image scale of $0\farcs88$ pixel^{-1} resulting in a $44' \times 30'$ field of view.

4.4.1.37 Fred L. Whipple Observatory

The Fred Lawrence Whipple Observatory houses a 0.43 m telescope and is located on Mt. Hopkins in Amado, AZ. The Fairchild CCD 486 detector has an image scale of $0\farcs672$ per 2×2 binned pixel, resulting in a $23\farcm1 \times 23\farcm1$ field of view.

4.4.1.38 Hazelwood Observatory

The Hazelwood Observatory is located near Churchill, Victoria, Australia. The 0.32 m telescope is equipped with a SBIG STT3200 camera with an image scale of $0\farcs55$ pixel^{-1}, resulting in a $20' \times 14'$ field of view.

4.4.1.39 Salerno University Observatory

The Salerno University Observatory houses a 0.6 m telescope and is located in Fisciano, Italy. The telescope is equipped with a FingerLakes Instrument Proline L230 that has a $21' \times 21'$ field of view with $0\farcs61$ pixel^{-1}.

4.4.1.40 Ground Survey and Space Data

We used archival ground-based survey data and related follow-up observations from HAT-South (Bakos et al., 2013) and WASP (Pollacco et al., 2006) that pre-dated the TESS mission to help disposition some of the planet candidates. We also used results from the Gaia-TESS collaboration (Panahi et al., 2022), which is a joint analysis of TESS photometry and unpublished Gaia time-series photometry, to disposition some planet candidates.

4.4.2 Reconnaissance Spectroscopy

TFOP's SG2 performed ground-based reconnaissance spectroscopy on a subset of targets in our best-in-class samples. These observations are crucial to constraining the mass of potential stellar or planetary companions to the host star and for refining the stellar parameters to be used in future analysis. Below we detail the observatories, instruments, and data reduction methods used to obtain the reconnaissance spectroscopy used in our analysis. See Section 4.5.4 for further discussion on how reconnaissance spectroscopy is used in our vetting procedures.

4.4.2.1 TRES

Reconnaissance spectra were obtained with the Tillinghast Reflector Echelle Spectrograph (TRES; Fűrész, 2008) which is mounted on the 1.5m Tillinghast Reflector telescope at the Fred Lawrence Whipple Observatory (FLWO) located on Mount Hopkins in Arizona. TRES is a fiber-fed echelle spectrograph with a wavelength range of 390-910nm and a resolving power of R$\sim$44,000. Typically, 2-3 spectra of each target are obtained at opposite orbital quadratures to check for large velocity variation due to a stellar companion. The spectra are also visually inspected to ensure a single-lined spectrum. The TRES spectra are extracted as described in Buchhave et al. (2010) and stellar parameters are derived using the Stellar Parameter Classification tool (SPC; Buchhave et al., 2012). SPC cross correlates an observed spectrum against a grid of synthetic spectra based on Kurucz atmospheric models (Kurucz, 1992) to derive effective temperature, surface gravity, metallicity, and rotational velocity of the star.

4.4.2.2 FIES

We used the FIbre-fed Echelle Spectrograph (FIES; Telting et al., 2014), a cross-dispersed high-resolution spectrograph mounted on the 2.56 m Nordic Optical Telescope (NOT; Djupvik & Andersen, 2010), at the Observatorio del Roque de los Muchachos in La Palma, Spain. FIES has a maximum resolving power of $R \sim 67,000$, and a spectral coverage that ranges from 3760 Å to 8820 Å. The data was extracted as described in Buchhave et al. (2010).

4.4.2.3 CHIRON

4.4.2.4 Keck/HIRES

4.4.2.5 HARPS-N

4.4.2.6 PFS

4.4.2.7 CORALIE

4.4.2.8 Minerva-Australis

4.4.2.9 NRES

The Network of Robotic Echelle Spectrographs (Siverd et al., 2018, NRES;) is a set of four identical fiber-fed spectrographs on the 1m telescopes of Las Cumbres Observatory (Brown et al., 2013b, LCOGT;). The NRES units are located at the LCOGT nodes at Cerro Tololo Inter-American Observatory, Chile; McDonald Observatory, Texas, USA; South African Astronomical Observatory, South Africa; and Wise Observatory, Israel. The spectrographs deliver a resolving power of R$\sim$53,000 over the wavelength range 3800-8600 Å. The data were reduced and radial velocities measured using the BANZAI-NRES pipeline (McCully et al., 2022). We measured stellar parameters from the spectra using a custom implementation of the SpecMatch-Synth package[3].

[3] https://github.com/petigura/specmatch-syn

4.4.2.10 WINE

4.4.3 High-resolution Imaging

As part of our standard process for validating transiting exoplanets to assess the possible contamination of bound or unbound companions on the derived planetary radii (Ciardi et al., 2015), we also observed the set of TOIs with a combination of near-infrared adaptive optics (AO) imaging and optical speckle interferometry at a variety of observatories including Gemini, Keck, Lick, Palomar, VLT, and WIYN Observatories. The combination of the observations in multiple filters enables better characterization for any companions that may be detected. See Sections 4.5.5 & 4.6 for further discussion on how high-resolution imaging was incorporated into our vetting and validation analyses, respectively.

4.4.3.1 Near-Infrared AO Imaging

Near-infrared AO observations are performed with a dither pattern to enable the creation of a sky-frame from a median of the science frames. All science frames are flat-fielded (which are dark-subtracted) and sky-subtracted. The reduced science frames are combined into a single combined image using an intra-pixel interpolation that conserves flux, shifting the individual dithered frames by the appropriate fractional pixels; the final resolution of the combined dithers was determined from the full-width half-maximum of the point spread function. The sensitivities of the final combined AO images were determined by injecting simulated sources azimuthally around the primary target every 20° at separations of integer multiples of the central source's FWHM (Furlan et al., 2017). The brightness of each injected source was scaled until standard aperture photometry detected it with 5σ significance. The final 5σ limit at each separation was determined from the average of all of the determined limits at that separation and the uncertainty on the limit was set by the rms dispersion of the azimuthal slices at a given radial distance.

4.4.3.2 Optical Speckle Imaging

High-Resolution optical speckle interferometry was performed using the 'Alopeke and Zorro instruments mounted on the Gemini North and South telescopes respectively (Scott et al., 2021; Howell & Furlan, 2022). These identical instruments provide simultaneous speckle imaging in two bands (562 nm and 832 nm) with output data products including a reconstructed image and robust contrast limits on companion detections (Howell et al., 2011). For each observed source, the final reduced data products contain 5σ contrast curves as a function of angular separation, information on any detected stellar companions within the angular range of 0.20 to 1.2 arcsec (delta magnitude, separation, and position angle), and reconstructed speckle images in each band-pass. The angular separation sampled, the 8-m telescope diffraction limit (20 mas) out to 1.2", can be used to set spatial limits in which companions were or were not detected.

4.5 Vetting

In order to determine the planetary nature of each target, we performed a uniform vetting procedure on each of the unconfirmed candidates. This included utilizing a mix of publicly-available resources and follow-up observations obtained by TFOP. We outline our overall procedure in schematic form in the middle panel of Figure 4.2. We ran each target through as many steps of our vetting procedure as possible given the availability of resources at the time of analysis since not all targets had the resources to complete each step in our procedure.

Although our vetting procedure checked for a number of false positive indicators, we refrained from classifying a target as a false positive unless we were confident that the transit signal could not be coming from a planet stemming from multiple false positive indicators. Our conservative approach to vetting passed most targets on to statistical validation, but provided invaluable information to be used in conjunction with the results from our validation analysis to make a final determination. In this way, vetting served as a complement to a more holistic determination of the planetary nature that accounts for a larger number of factors than any individual analysis alone could provide.

For all of our vetting, we used the orbital and planetary parameter values posted on ExoFOP[4] unless follow-up observations revealed more accurate or precise values for a given parameter, in which case, the parameters obtained from follow-up were used. There were two targets with ambiguous periods contained in our best-in-class samples from the query of the Exoplanet Archive. These targets were single transits that transited again in one or more later TESS sectors, but without two or more transits within a single TESS sectors or consecutive TESS sectors, the period could not be confidently determined. Since we are unable to obtain the true periods to these targets without a concerted observing campaign, we analyzed them with the reported ExoFOP periods that represent upper limits to the true periods. We recognize that the periods and therefore amenability to atmospheric characterization with JWST may change for these targets, but we include them in our best-in-class samples to emphasize their potential as prime JWST targets and encourage their further study.

[4]https://exofop.ipac.caltech.edu/tess/

4.5.1 *TESS* SPOC Data Validation Report

Most of the targets in our best-in-class samples were either discovered by (or at the very least run through) the TESS SPOC pipeline (Jenkins et al., 2016). This pipeline performs a number of tasks on each target, including light curve extraction, correction, and searches for potential planets as well as a suite of diagnostic tests in the Data Validation (DV) module to help adjudicate the planetary nature of each signal (Twicken et al., 2018b; Li et al., 2019b). Upon running the pipeline, the outputs were reviewed by the TESS TOI Working Group (TOI WG) to perform initial vetting. This initial vetting has already been performed by the TOI WG for all of our targets, but we reviewed the SPOC pipeline outputs again to ensure nothing was missed.

The DV module includes a depth test of the odd and even transits, a statistical bootstrap test that accounts for the non-white nature of the observation noise to estimate the probability of a false alarm from random noise fluctuations, a ghost diagnostic test to compare the detection statistic of the optimal aperture against that of a halo with a 1 pixel buffer around the optimal aperture, and a difference image centroid test. At the conclusion of these tests, the module synthesizes a summary of the results for each individual test, including assigning a pass/fail disposition for each test. We used the results of each of these tests in our vetting efforts to help determine if a target was a likely planet, false positive, or false alarm.

In addition to the DV module results, we also determined if the period was ambiguous for a given target due to nonconsecutive transits from gaps in the TESS data. Although not a false positive indicator, this was flagged for future reference in downstream analyses. We also checked the light curves for significant photometric modulation indicative of stellar activity that could pose a problem in future vetting and validation analysis. In the absence of SPOC DV results, we still inspected the light curve and ephemerides for an ambiguous period or photometric modulation using available, published light curves such as those from MIT's QLP.

4.5.2 DAVE Vetting from Cacciapuoti, et al.

A subset of our targets had already been vetted not only by the TESS TOI WG, but by an independent team using DAVE. The results of this vetting were collated in Cacciapuoti et al. (2022) where each of the 999 targets vetted were assigned a final disposition as to the target's planetary nature.

DAVE is an automated vetting pipeline built upon many of the tools developed for vetting planets in *Kepler* data (e.g. RoboVetter, Coughlin et al. 2014b) and has been used extensively in vetting planets for TESS (e.g. Gilbert et al., 2020b; Hord et al., 2021; Quintana et al., 2023). DAVE performs two sets of vetting tests: 1.) light curve-based vetting tests searching for odd/even transit depth differences, secondary eclipses, and light curve modulations and 2.) image-based centroid tests to check the photometric motion on the TESS image during transit.

For the targets in our best-in-class samples that were also contained in the Cacciapuoti et al. (2022) catalog, we included their dispositions in our vetting analysis. Since there is overlap between the tests performed by the TESS SPOC pipeline and DAVE, we treat the two as independent checks of one another and review the results in comparison.

4.5.3 Reconnaissance Photometry

Due to the large 21" pixel size of TESS, ground-based photometry at higher spatial resolutions is crucial in determining whether a transit-like feature is occurring on-target or is the result of a background target in the starfield that may have been blended within the TESS pixel. Stars nearby the target are checked for deep EBs that could cause the observed transits and are ruled out on a case-by-case basis. Any deviations from an on-time transit are also noted. These often occur due to uncertainties in the period or mid-transit time reported by ExoFOP but may be caused by gravitational interactions within the system. If the period deviates significantly from the reported period, the ephemerides are refined based on the ground-based photometric observations. This was the case for multiple targets, especially those with fewer sectors of TESS data or those with an ambiguous period.

In addition to checking which star the transit-like feature originates from, ground-based photometry uses multiple filters to check for possible chromaticity in the transit depth that would indicate an eclipsing binary rather than a planet is causing the transit. A light curve is also extracted from the target star with a small aperture to mitigate the contamination from nearby stars. The transit depth is measured to ensure that it is not only consistent across wavelength bandpasses, but is the right depth to cause the transit observed in the TESS data.

TFOP's SG1 synthesizes the results of the photometric observations for each target into a single disposition describing the confidence with which a signal can be considered on-target. We utilized these dispositions and observations when determining which background stars to consider as potential sources of astrophysical false positives in our vetting analysis.

In addition to the photometry gathered by SG1, we also utilized the code `DEATHSTAR` (Ross et al., submitted) to search archival images from ZTF for the transit signal.

DEATHSTAR attempts to either confirm or refute exoplanet detections with already available ground-based data from the Zwicky Transient Facility (ZTF) (Bellm et al., 2019) by extracting light curves for each star in a 2.5 arcminute field and plotting them for manual verification of the actual signal location. This way we can tell if an unconfirmed TOI is an exoplanet transiting in front of the target star or an eclipsing binary on a nearby fainter star. DEATHSTAR creates plots for each extracted light curve and displays them in custom sheets for us to easily find the source of the transiting signal. We work with SG1 in checking these results with the SG1 Observation Coordinator sheet and sending them to reduce extraneous telescope follow-up time. For deeper transit depths on-target (ranging from 1-3%), DEATHSTAR has been able to confirm on-target detections making the target a Verified Planet Candidate (VPC). Due to ZTF's multiple filters (green, red, and infrared), these detections are achromatic where we can promote VPCs to VPC+, with the plus denoting achromaticity. In most of the cases for these targets, the depth was much shallower than a percent which DEATHSTAR was not able to detect, but we still cleared all the surrounding stars in the field for being potential eclipsing binaries. This means that the signal of the transit must be from an exoplanet orbiting the target star.

4.5.4 Reconnaissance Spectroscopy

Although only a subset of the targets in our sample had ground-based spectroscopic observations available, these data provided strong constraints on the presence of bound companions in the target system that photometry is unable to capture. Spectroscopy alone is often able to determine if the stellar spectrum is composite which would indicate the presence of a bound stellar mass companion. The presence of a composite spectrum with orbital motion that is consistent with the TESS ephemeris was an automatic false positive designation for the targets in our samples but only applied to one target (TOI-4506.01).

For most targets, two spectroscopic observations were taken at opposite quadratures assuming a circular orbit at the photometric ephemeris and compared to the photometric ephemeris to determine if they were in-phase. Spectroscopic data at opposite quadratures that are out of phase with the photometric ephemeris could indicate the presence of a large stellar-mass object instead of a planet, although this could also indicate a long-term trend in the system due to additional bodies in the system or an eccentric orbit rather than a false positive scenario. For reconnaissance spectroscopy that was in-phase with the photometric ephemeris, the semi-amplitude of the measurements at quadrature was used to constrain the mass of the object producing the transit signal, potentially ruling out stellar masses and providing evidence for the planetary nature of the body.

By virtue of modeling the stellar spectrum, reconnaissance spectroscopy also has the potential to measure parameters such as the effective temperature, metallicity, and v sin$i$ of the host star. Where possible, we used these measured values rather than those from TIC or *Gaia* DR3.

Similar to SG1, TFOP's SG2 also synthesizes reconnaissance spectroscopic observations into a disposition for each target. These dispositions capture the confidence that the target is a planetary mass object and is suitable for precision radial velocity observations to determine the orbit and constrain the mass further. We broadly utilized these dispositions when vetting to determine whether a target can be safely deemed a false positive or should continue to statistical validation analysis. There were multiple cases where reconnaissance spectroscopy existed but the stellar activity or rotational broadening of spectral features precluded anything but upper limits on the masses of potential companions.

4.5.5 Imaging Constraints

As a complement to ground-based photometry and reconnaissance spectroscopy, high-resolution imaging can provide strict constraints on the presence of stellar companions in the system or nearby background targets that could potentially contaminate the target signal. Each target was first cross-referenced with the *Gaia* DR3 catalogue to determine if there were any resolved nearby stars within a few arcseconds of the target star. In a handful of cases, *Gaia* resolved nearby stars at similar parallaxes to targets in our best-in-class samples. While not a definite indicator of a false positive, the presence of a nearby companion at a similar parallax invited further scrutiny for that particular target. In those cases, we cross-referenced the nearby star with other follow-up observations where possible to determine if the star observed by *Gaia* may be the cause of anomalies and potential false positive indicators in the ground-based photometry or reconnaissance spectroscopy.

We also utilized speckle or adaptive optics (AO) imaging available on ExoFOP (see Section 4.4.3) that observed each planet candidate in a more targeted manner at a higher angular resolution than *Gaia*. These observations allowed us to search for bound companions or background stars that may contaminate the photometry or cause the observed transit signal. These observations were also cross-referenced with other follow-up observations to determine how strongly false positive or dilution scenarios can be constrained or if the signal is likely not due to a planet. The sensitivity curves that these observations produced were also used in our statistical validation analysis (Section 4.6).

4.6 Validation

While vetting is an integral step in determining whether a periodic signal is indeed due to the presence of a planet, it cannot alone demonstrate that a signal is not a false positive. The preferred method for determining whether a signal is a planet is a mass measurement through radial velocity (RV) observations, however these oftentimes require a significant commitment of resources and time on targets that may not prove to be planets.

In lieu of a mass measurement, statistics can be used to validate the target rather than confirm it. Statistical validation of a target often only requires photometric and imaging observations as well as planetary and orbital parameters input into one or multiple statistical validation softwares. Targets that are validated to a greater than 99% confidence threshold are considered planets despite not having a mass measurement (Morton, 2012b; Giacalone et al., 2021b). Since the time and observational resources required to validate a planet are far less than required to obtain a mass measurement, statistical validation serves as an excellent intermediate step to weed out targets that are very likely not planets in order to better streamline and prioritize the RV observations required to confirm a target as a bona fide planet.

In the case of our best-in-class samples, since there are undoubtedly false positives contained within the unconfirmed planet candidates, we performed statistical validation on all candidate planets to not only determine which targets are most likely to be true planets, but which merit follow up with RV observations. To do this, we run the statistical validation softwares `vespa` (Morton, 2012b, 2015b) and `TRICERATOPS` (Giacalone & Dressing, 2020b) on each of our unconfirmed targets in both the transmission and emission spectroscopy samples.

For all of our targets, we use the orbital and planetary parameters from ExoFOP unless the follow-up observations that we collated reported refined parameters (Section 4.4), in which case the refined parameters were used. For `vespa`, this also included stellar parameters. TESS photometry was used to produce the phase-folded transits used in both `vespa` and `TRICERATOPS`. When possible, we favored light curves produced by the TESS SPOC at the shortest cadence available since shorter cadence TESS data has been shown to be more photometrically precise when binned than data taken at the binned cadence itself (Huber et al., 2022). A small subset of targets did not have SPOC PDCSAP light curves, in which case we used light curves produced by MIT's QLP.

4.6.1 `vespa`

`vespa` (Morton, 2012b, 2015b) was originally developed for use on *Kepler* data and compares the input orbital and planetary parameters as well as the phase-folded transit against a number of astrophysical false positive scenarios to determine the likelihood that the signal can be produced by each false positive population. Currently, `vespa` tests against the hypotheses that the signal is a blended background or foreground EB (BEB), the target itself is an EB, or the target is a hierarchical-triple system where two of the components form an EB (HEB). To do this, `vespa` simulates a representative population of each false positive scenario at the observed period and calculates the priors of each scenario, accounting for the probability that the scenario is contained within the photometric aperture, the probability of an orbital alignment that would cause an observable eclipse, and the probability that the eclipse could mimic a transit. A TRILEGAL simulation (Girardi et al., 2005, 2012) is used to simulate the background starfield for each target when calculating the priors. The likelihoods of each scenario are then calculated by modeling the shape of the eclipse for each instance of each false positive population and fitting it to the observed light curve. The priors and likelihoods are finally combined to calculate the total FPP of the input transit signal. Signals with an FPP < 0.01 are considered statistically validated.

Beyond the phase-folded light curve and planetary and orbital parameters, `vespa` can also intake sensitivity curves from high-resolution imaging to rule out portions of the false positive parameter space. Additionally, `vespa` takes the maximum photometric aperture radius as an input to use in calculations of the BEB prior. We set this parameter to 42”, the size of two TESS pixels.

4.6.2 `TRICERATOPS`

Similar to `vespa`, `TRICERATOPS` (Giacalone & Dressing, 2020b) compares the user-provided phase-folded transit, orbital, and stellar parameters against a set of astrophysical false positive scenarios to rule out portions of parameter space in which the false positive scenarios can remain viable. The methodology of `TRICERATOPS` is identical to `vespa` in many respects, however, in contrast to `vespa`, `TRICERATOPS` was developed specifically for TESS and accounts for the real sky background of each target out to 2.5’ as well as the TESS point spread function and aperture used to extract the photometric light curve in each sector of TESS data. An example of what `TRICERATOPS` considers in this portion of its analysis is seen in Figure 4.4.

For each target, we used the extraction apertures produced by the TESS SPOC contained within the headers of the SPOC PDC-SAP light curves queried by `lightkurve` (Lightkurve Collaboration et al., 2018b) on a sector-by-sector basis. For the targets missing SPOC PDC-SAP light curves from some or all TESS sectors they were observed in, we used a standard aperture of

5×5 TESS pixels. This is larger than any of the PDC-SAP apertures and is the `TRICERATOPS` default for sectors without provided apertures.

When accounting for nearby background stars for each target, `TRICERATOPS` queries the TICv8 for the stellar parameters of each star. The TIC is based heavily on the *Gaia* DR2 data release, which has since been updated by *Gaia* DR3. Therefore, in our analysis, we queried the RA, Dec, mass, effective temperature, parallax, and *Gaia G* magnitude of the host star *Gaia* DR3 Catalog for use in our analysis in lieu of using the values provided by the TIC. To convert the *Gaia* magnitude to TESS magnitude, we used Equation 1 from Stassun et al. (2019b) which is valid for dwarfs, subgiants, and giants of any metallicity. We then cross-referenced each *Gaia* target with the 2MASS catalog (Skrutskie et al., 2006b) to obtain J, H, and K magnitudes where available as these magnitudes are used by `TRICERATOPS` in its estimation of false positive probability.

Additionally, we included follow-up constraints into our analysis with `TRICERATOPS`. When available, we included a contrast curve from high-resolution imaging to constrain the existence of additional stellar mass companions in the system. Unlike `vespa`, `TRICERATOPS` only accepts a single contrast curve per target, so in the case a target possessed multiple contrast curves from follow-up observations, we only included the contrast curve that provided the greatest imaging contrast magnitude to most stringently constrain possible companions in the system. Furthermore, our photometric follow-up allowed us to clear individual nearby stars of potentially harboring EBs that would cause the observed transit signal on target. Background stars that were definitively determined to not be EBs at the target period or have an eclipse depth that could cause the observed transit on-target were discarded from consideration as potential sources of a false positive. Targets whose transits were observed on-target had all background stars removed from false positive consideration. As recommended by (Giacalone et al., 2021b), we ran each multiple trials of the TRICERATOPS FPP calculation for each target, with a minimum of 10 trials per target and report the mean of these FPPs.

TRICERATOPS provides not only a final FPP value, but also a NFPP value that encapsulates the probability that the signal originates from a star other than the target. Giacalone et al. (2021b) defines validated planets as signals with FPP < 0.015 and NFPP $< 10^{-3}$ and outlines a separate category for marginal validations when FPP < 0.5 and NFPP $< 10^{-3}$. We adopt these categories in our determination of the planetary nature for our best-in-class samples. We extend the marginal validations category to vespa, which does not explicitly have such a distinction. In the case of vespa, we conservatively set the marginal validation threshold to FPP < 0.25, lower than that of TRICERATOPS.

Morton et al. (2023) recommends the use of TRICERATOPS in favor of vespa since the latter is no longer maintained and has not been updated to account for the modern astronomy landscape. We present validation using both softwares as an independent check on one another but emphasize the results of TRICERATOPS over those of vespa in cases where their FPP values may disagree. This means that many of the targets in our best-in-class sample that are classified as "Likely Planets" may actually fall within the realm of true statistical validation when only considering the results from TRICERATOPS.

We also note that our statistical validation analysis cannot rule out the scenario in which validated planets with $R_p > 9\ R_\oplus$ are actually brown dwarfs. A measured mass is required to disentangle the brown dwarf and planet scenarios and we encourage follow up on all validated planets to this effect.

Table 4.1: All of the statistically validated planets in both the transmission and emission spectroscopy best-in-class samples. Empty values for the TSM and ESM indicate that the target was not considered best-in-class for transmission or emission spectroscopy, respectively.

Planet Name	T_{eq} [K]	R_{p} [$R_{\oplus}$]	Period [d]	TSM	ESM
TOI-128.01	1345	2.22	4.94	90	
TOI-238.01	1454	1.86	1.27		8
TOI-406.01	344	1.96	13.18	55	
TOI-261.01	1722	3.04	3.36	79	
TOI-332.01	1946	3.28	0.78	62	11
TOI-654.01	749	2.37	1.53		9
TOI-907.01	1847	9.62	4.58		28
TOI-1135.01	1074	9.34	8.03	243	
TOI-1194.01	1405	8.89	2.31	217	69
TOI-1347.01	1793	2.70	0.85	79	12
TOI-1410.01	1396	2.94	1.22	118	20
TOI-1683.01	929	2.64	3.06	101	
TOI-3353.01	1264	2.67	4.67	90	
TOI-4495.01	1383	3.63	5.18	74	
TOI-4527.01	1363	0.91	0.40		13
TOI-4602.01	1380	2.55	3.98	111	11
TOI-5082.01	1165	2.55	4.24	160	15
TOI-5388.01	601	1.89	2.59		12

4.7 Results

Of the 103 unconfirmed TESS planet candidates contained in our best-in-class samples, 18 passed vetting and were calculated to have FPP values firmly meeting the threshold for statistical validation from both `vespa` and `TRICERATOPS`. These targets are shown in Table 4.1. We strongly recommend these targets for additional, in-depth study and confirmation to measure their masses and model their orbits and atmospheres in preparation for potential observation with JWST.

A total of 29 targets were deemed false positives. These targets all exhibited obvious signs of a false positive in the vetting stage and/or produced FPP values from both statistical validation softwares. A target was deemed a false positive if the FPP from both `vespa` and `TRICERATOPS` did not meet either the validation or marginal validation thresholds. For one of these false positive targets, we were unable to locate the transit-like event that was flagged by the TESS SPOC during our manual inspection of the phase-folded light curve and we deemed it a false alarm (TOI-1022.01). Most of these 29 false positive targets exhibited obvious V-shaped transits indicative of an EB and a subset of them were revealed by TFOP follow-up to have a nearby ($\leq$2") companion star that served as the likely cause of the signal.

There was a subset of targets with high FPP values that could be large grazing planets or systems with a high planetary to stellar radius ratio (R_p/R_*) rather than their current FP classification. Grazing transits or high R_p/R_* systems often produce transits that look somewhat V-shaped and can masquerade as a stellar eclipse rather than a planet transit. These scenarios are limiting cases for the validation softwares since the analyses rely so heavily on transit shape. Therefore, targets with high FPP values that could potentially fall under these categories warrant further follow-up. For our purposes, we keep these targets classified as FPs for the sake of a uniform analysis, but we flag them here for future study and as examples of the limitations of statistical validation.

A third category of validation emerged for targets with FPP values that did not quite meet the threshold for validation but also were not obvious false positives. These 38 targets were deemed to be marginal validations and had at least one or both FPP values from `vespa` and `TRICERATOPS` that met the marginal validation criteria described in Section 4.6. This category was further subdivided into "likely planets" (LPs) and "potential false positives" (pFPs). LPs were targets with either both FPP values residing in the marginal validation zone or one FPP in the marginal validation zone and the other meeting the threshold for validation. pFPs were targets with one marginal validation FPP and one FPP that indicates a false positive.

The results of our vetting analysis agrees with these distinctions based on FPP. Almost all of the targets in the pFP category had at least one vetting factor that could indicate a false positive origin (e.g. V-shaped transit, possible odd-even transit depth differences, etc.) but are not definitive enough to warrant labeling the target a full-fledged false positive. There were a total of 19 targets in the LP category and 19 in the pFP category of marginal validations. We encourage future study and follow up of these targets to ascertain their true nature as they could potentially be prime targets for atmospheric characterization with JWST. Examples of transits from each disposition category are shown in Figure 4.5.

The remaining 4 targets produced inconclusive vetting and validation results. This category is distinct from marginal validations in that in most of these inconclusive cases `vespa` and `TRICERATOPS` disagree significantly on the status of each target or there are additional factors precluding an adequate vetting or validation analysis. The targets TOI-1355.01, TOI-1954.01, and TOI-4552.01 were validated by one statistical validation software while the other software produced an FPP that did not meet the threshold for even a marginal validation.

In the case of TOI-1355.01, the discrepant FPPs may be due to overly constraining photometric follow-up observations. The transit shape is slightly V-shaped, and our follow-up observations rule out a large portion of parameter EB and BEB parameter space, but those are the models that fit the phase-folded transit the best (resulting in FPP values with large uncertainties from `TRICERATOPS`). This target may be a grazing planet, which would explain the V-shape as well as the small parameter space for EBs and BEBs.

In the case of TOI-1954.01, no follow-up exists and the target is in a crowded field, both of which likely combine to cause the discrepancy between `vespa` and `TRICERATOPS`. For TOI-4552.01, the signal is shallow and the light curve exhibits some variability which is likely causing variability in the FPP values calculated by the different validation softwares.

The final inconclusive case is TOI-4597.01. This target was statistically validated by `vespa` but `TRICERATOPS` was unable to run on it. This is likely due to the short periodic oscillations that appear in the light curve as a result of stellar activity or variability. A clear transit exists, but we are unable to complete our vetting and validation analysis without properly modeling the variability in the light curve to produce a clean transit. This is beyond the scope of this work as it would require a physically-motivated model to subtract from the light curve that our vetting and validation procedure is incapable of. We encourage follow-up analysis of these four inconclusive targets to determine their true nature.

There were an additional 14 targets from our samples that were confirmed by independent teams over the course of our analysis. These targets are TOI-179 b (Desidera et al., 2022), TOI-622 b (Psaridi et al., 2023), TOI-836 b (Hawthorn et al., 2023), TOI-969 b (Lillo-Box et al., 2023), TOI-1099 b (Barros et al., 2023), TOI-1468 b & c (Chaturvedi et al., 2022), TOI-1853 b (Naponiello & et al., accepted), TOI-2134 b (Rescigno & et al., submitted), TOI-3235 b (Hobson et al., 2023), TOI-3884 b (Almenara et al., 2022), TOI-4463 A b (Yee et al., 2023), GJ 806 b (TOI-4481 b; Palle et al., 2023), and HD 20329 b (TOI-4524 b Murgas et al., 2022). This high number of targets in our best-in-class sample being confirmed in such a short period of time is very positive for the prospects for atmospheric characterization with JWST. Indeed, the goal of our synthesis of the best-in-class sample is to highlight and elevate targets potentially well-suited to such observations for follow-up to measure their masses and confirm their planetary nature. In the case of TOI-1853 b, the measured mass differed significantly from that predicted by the

Chen & Kipping (2017) mass distribution, resulting in TSM and ESM values much lower than calculated. We therefore remove it from our best-in-class sample.

Of the 103 unconfirmed planet candidates analyzed, 11 reside in potential multiplanet systems (TOI-1468.01, TOI-1468.02, TOI-1798.02, TOI-1806.01, TOI-2134.01, TOI-3353.01, TOI-406.01, TOI-4443.01, TOI-4495.01, TOI-835.02, TOI-880.02). Three of these have already been confirmed by independent teams (TOI-1468.01 & .02 and TOI-835.02). These systems represent an excellent opportunity to perform comparative planetology with the other planets in their system using JWST. It has been shown that transit-like signals in systems with multiple transit-like signals are more likely to be true planets, assuming false positives are uniformly distributed throughout the sky (Lissauer et al., 2012b). This results in a decreased FPP value of up to 56$\times$ depending on the size of the planets and how crowded the field is for signals detected with TESS (Guerrero et al., 2021). Our validation analysis does not account for the "multiplicity boost" and so many of these targets in potential multiplanet systems may have lower FPP values than reported here.

Our best-in-class sample also includes three targets with ambiguous periods – TOI-2299.01, TOI-1856.01, and TOI-4317.01. These targets were originally discovered as single transits before transiting again in later sectors of TESS data. The periods reported on ExoFOP represent the upper limit on their periods since additional transits of these targets could have fallen in gaps in the TESS data and their true periods may be shorter. We performed our vetting and validation using the stated periods but knowing that future observations could reveal shorter periods that would alter the TSM and ESM values as well as their observability with JWST. We choose not to discard these targets from our best-in-class samples to emphasize their potential as ideal JWST targets and emphasize the need for additional follow-up on them. Only TOI-4317.01 had low enough FPP values to be considered statistically validated, but due to its ambiguous period, we place it in the "likely planet" category and we caution that a deeper analysis is required for this target to identify the true period and therefore its true planetary status.

The final best-in-class sample is displayed in Figure 4.6, which mirrors Figure 4.1 but now includes updated dispositions for all targets in our samples, both confirmed and unconfirmed. Additional information on each target can be found in Table **??** in Appendix **??**. An extended machine-readable version of this table is also available in the online version of this article.

There were a number of targets in our best-in-class sample that are also in the process of being validated by independent teams. These include TOI-4226.01 (Timmermans & et al., in prep.) and TOI-4317.01 (Osborn et al., in prep.). We direct the reader to these upcoming publications for a more in-depth analysis and exploration than is available here and to treat such in-depth analyses as the definitive discovery papers for these individual targets. Dressing et al. (in prep.) is also conducting a parallel large-scale validation effort on TOIs 261.01, 4317.01, 4527.01, 4602.01, and 5082.01, as is Mistry & et al. (in prep.) for TOIs 238.01 and 771.01 and we direct the reader to this upcoming publication for an additional, independent vetting and validation of these targets. Additionally, independent teams are conducting confirmation and characterization of TOI-1410.01 (Livingston & et al., in prep.) and TOIs 1194.01, 1347.01, and 1410.01 (Polanski & et al., in prep.) and we direct the reader to that paper for an in-depth analysis of these targets.

4.8 Summary and Conclusion

In this paper, we present a set of best-in-class planets for atmospheric characterization with JWST through both transmission and emission spectroscopy. Our vetting, validation, and results are summarized here:

- We queried the NASA Exoplanet Archive for all transiting confirmed planets and unconfirmed TESS candidates and calculated their TSM, ESM, and observability with JWST.
- We divided all planets into grids with bins in equilibrium temperature, T_{eq}, from 100 to 3000 K and planetary radius, R_p, from 0.3 to 25.0 $R_\oplus$ and the top five planets and candidates were ranked by spectroscopy metric in each bin to create a best-in-class sample for each spectroscopy method.
- The 103 unconfirmed TESS-discovered candidates from the transmission and emission spectroscopy grids were vetted using a combination of follow-up observations collected by TFOP and independent analyses such as the SPOC DV reports.
- We used `vespa` and `TRICERATOPS` to calculate the false positive probabilities and determine a final disposition for each target.
- Our analysis resulted in 18 validated targets, 29 false positives, 38 targets that were marginally validated, and 4 inconclusive validations. Of our original targets, 14 were independently confirmed over the course of our analysis.
- This final sample represents the best-in-class targets for atmospheric characterization with JWST and deeper analysis on each target is highly encouraged.

We recognize that this best-in-class sample will undoubtedly change over time as new targets supplant previous ones in the JWST observability rankings, as targets are shown to be false positives, or as the orbital and planetary parameters of targets are refined with further observation. The sample presented here is meant to represent an initial look at many of the targets with the potential to yield high quality spectra from JWST. We hope that this work paves the way for future studies of a similar sort. We highly encourage independent analysis of each target presented here to discern the true nature of each and build a catalog of planets that can reliably provide exquisite atmospheric data from JWST.

This sample may also change based on the assumptions used to generate it. Our analysis calculated the ESM value for planets in all portions of parameter space even though it was originally developed by Kempton et al. (2018) for terrestrial planets. Parameter values baked into the ESM quantity such as the day-night heat redistribution on a planet may be different from what is assumed by our calculations. However, since our rankings of best-in-class targets are relative to other planets and candidates of similar radius and equilibrium temperature, this factor can likely be ignored. Additionally, it is possible that the thermal emission of planets hotter than ~ 800 K can be observed with NIR instruments rather than with MIRI as assumed by our analysis. This would open up access to brighter stars due to the favorable ratio between the flux of the planet's thermal emission and the flux of the star and would allow for study of a different set of spectral features compared to those available to MIRI. The sample presented here makes parameter cuts for emission spectroscopy based on the performance of MIRI, but a blend of instruments would open up the pool of potential best-in-class targets for the hottest portions of parameter space.

This sample also demonstrates the power of TESS in its ability to discover planets amenable for atmospheric characterization and from which we can subsequently study to learn a great deal about their atmospheric structure and composition. Approximately 57% of the targets in the final best-in-class sample (excluding false positives) are TESS discoveries. It is therefore important to continue searching for planet candidates that could turn out to be excellent targets for atmospheric study since, as shown here, many of the best planets for study with JWST are still being revealed.

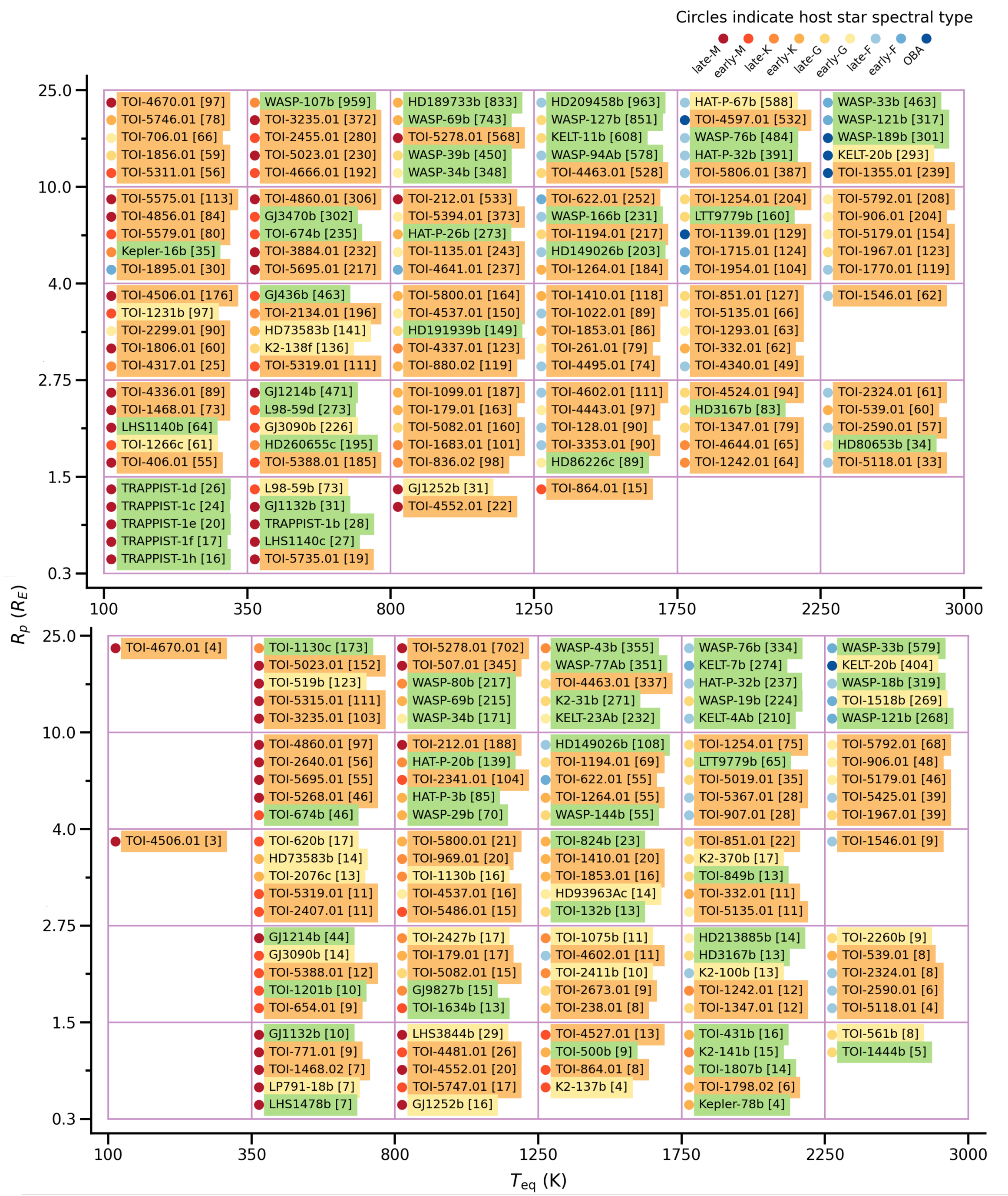

Figure 4.1: Our best-in-class targets for transmission (*top*) and emission (*bottom*) spectroscopy as of November 3, 2022 sorted by equilibrium temperature, T_{eq}, and planetary radius, R_p. Target names are shown with the respective spectroscopy metrics (ESM or TSM) in brackets next to the name. Targets are sorted within each cell by spectroscopy metric in descending order. Stellar type of the host star is denoted by the colored circle to the left of each name. Targets are color-coded by mass status: green targets are confirmed planets with mass measurements $>5\sigma$, yellow targets are confirmed planets with mass measurements $<5\sigma$, and orange targets are unconfirmed TOIs.

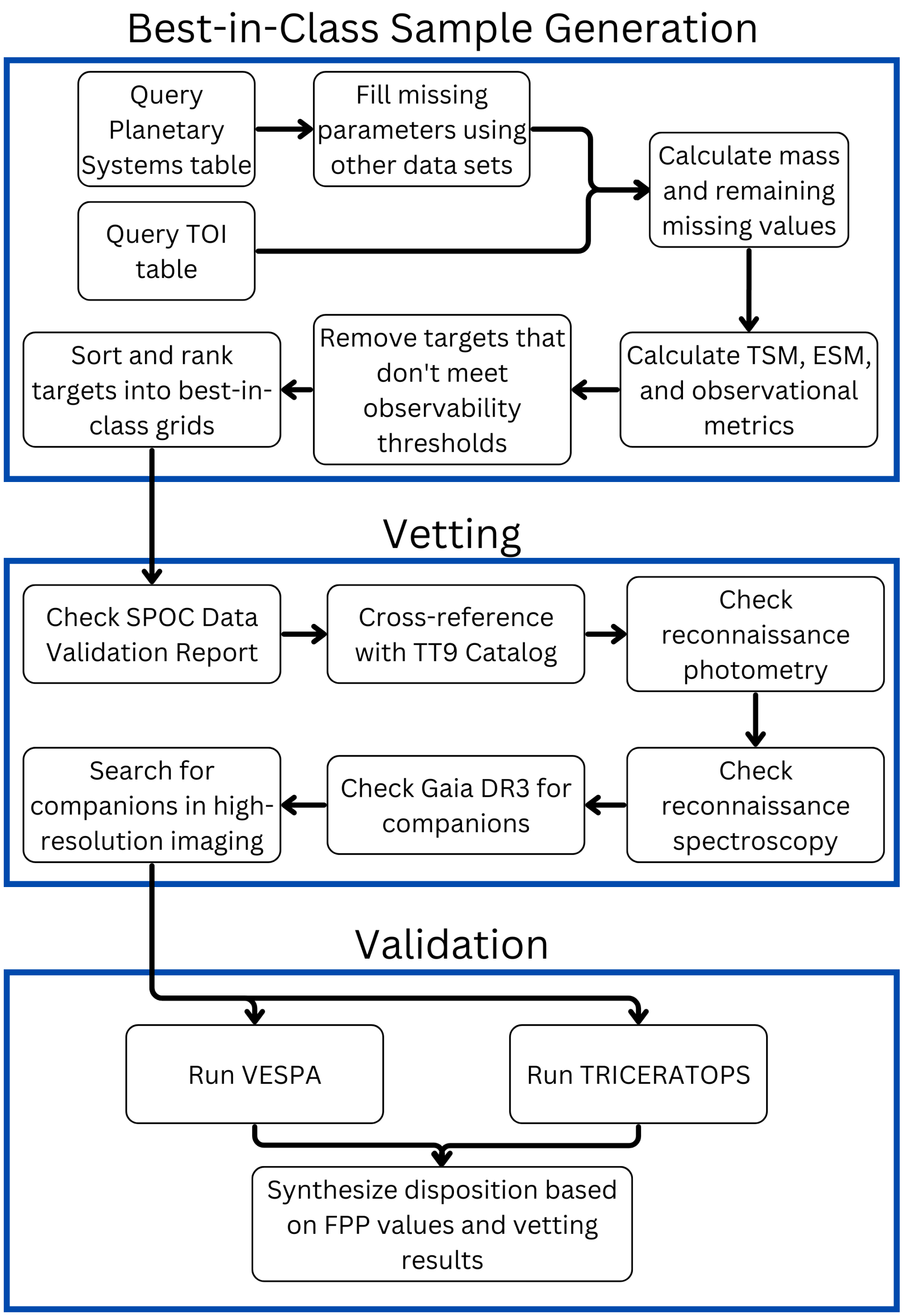

Figure 4.2: A schematic outline of our analysis procedure. From the initial query of the Exoplanet Archive and generation of the best-in-class sample, each target went through every step of the procedure to check for factors that could indicate a false positive to arrive at a final disposition. Not every vetting step applied to every target due to lack of follow-up, so each vetting step was applied when possible but skipped when not.

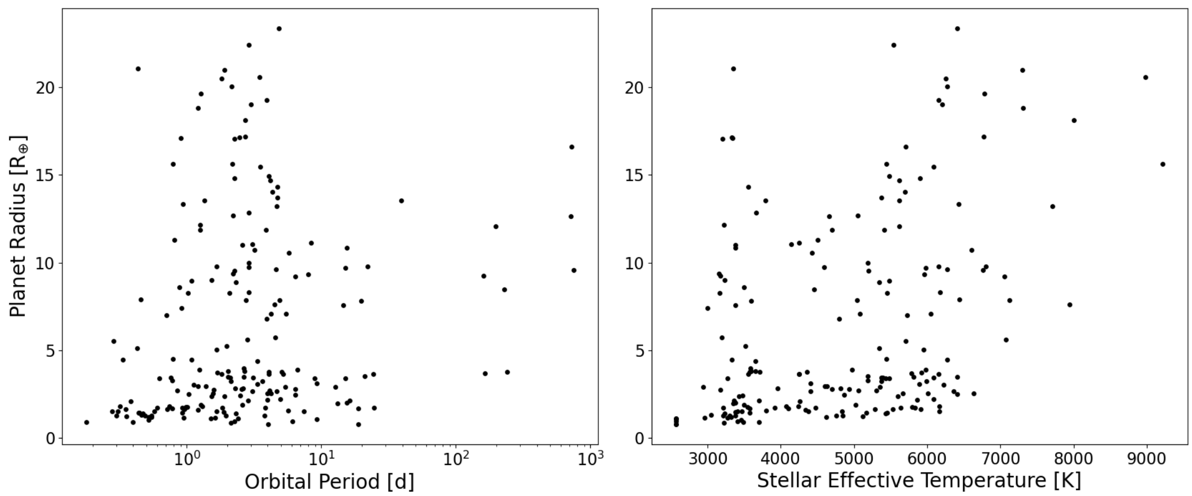

Figure 4.3: The spread of targets in our best-in-class samples. *Left:* the orbital periods and planetary radii of the combined TSM and ESM best-in-class samples. *Right:* the effective temperature of the host stars and the planetary radii of the same combined best-in-class sample. Although only selected to adequately cover the planetary radius and equilibrium temperature parameter space, the best-in-class sample exhibits good coverage of multiple different parameter spaces and can be considered a representative subset of exoplanetary targets.

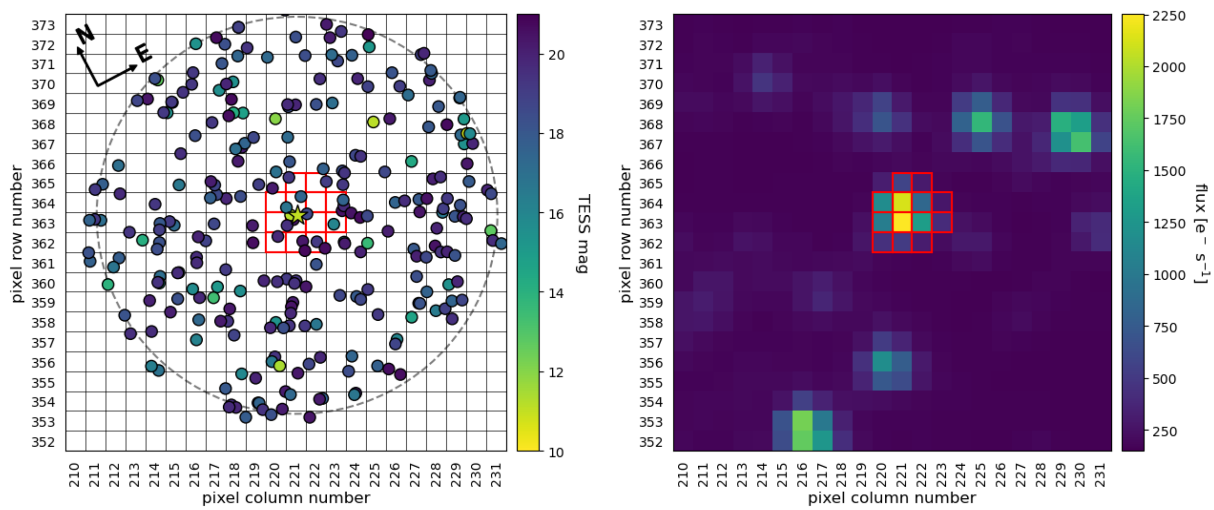

Figure 4.4: Starfield around TOI-4336.01 in TESS Sector 38 used by `TRICERATOPS` in its FPP and NFPP calculations. *Left:* plot of the positions of each star within 2.5 arcminutes centered on the target with the color of each point representing the TESS magnitude of the star. The overlaid grid denotes the TESS pixel borders with pixel column and row numbers labeled on the X and Y axis, respectively. The dashed gray circle represents a distance of 2.5 arcminutes and the red squares denote the extraction aperture used by the SPOC when generating the PDC_SAP light curve for this TESS sector. *Right:* Same as left but instead of displaying each background star near the target, TESS data is shown. The SPOC extraction aperture is in red and the colormap represents the flux captured by each TESS pixel.

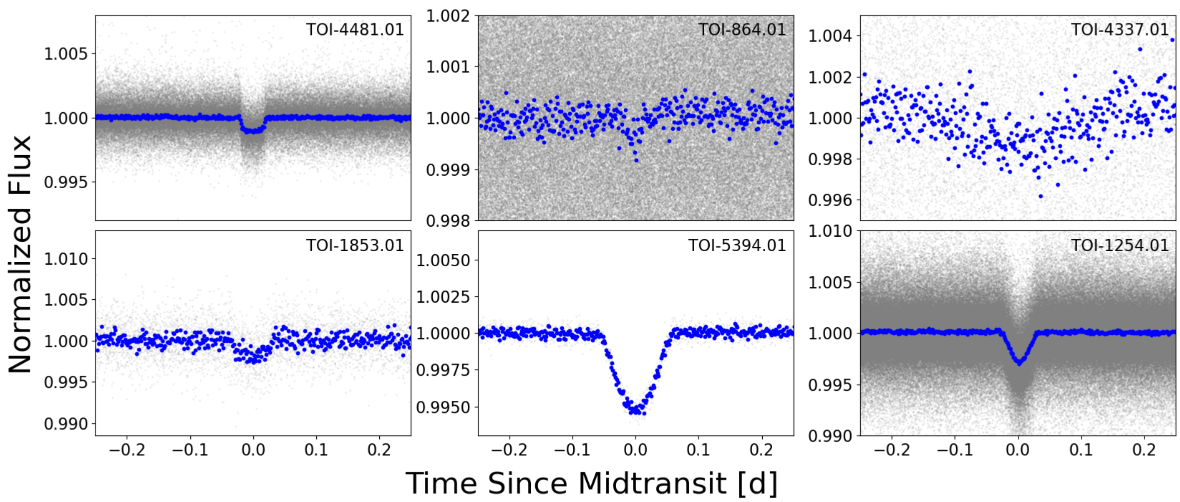

Figure 4.5: Examples of transits from targets in each disposition category. *Left column:* examples of validated planets. Both transits are well-defined with flat bottoms. *Middle column:* examples of a marginal validations; a likely planet (*top*) and a potential false positive (*bottom*). These targets either have a low signal-to-noise ratio or a transit shape that can be confused with an eclipsing binary and cannot be validated but are also not clear false positives. *Right column:* examples of false positives. These targets either have a very obvious V-shape, otherwise non-transit-shaped feature, or have been deemed false positives during vetting (e.g. a large centroid offset).

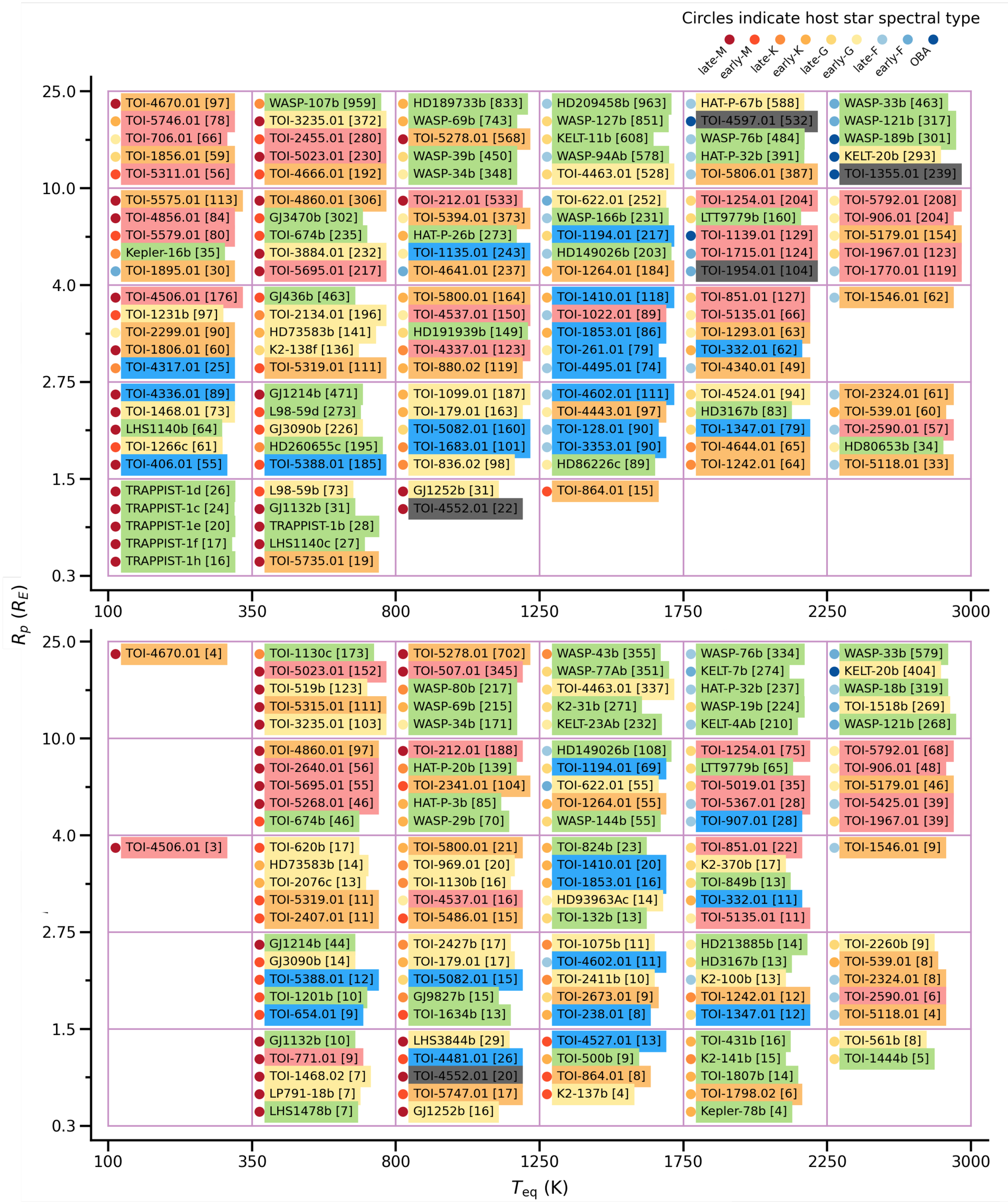

Figure 4.6: Our best-in-class targets for transmission (*top*) and emission (*bottom*) spectroscopy after performing our vetting and validation analysis on the sample. Similar to Figure 4.1, target names are displayed in the cell corresponding to the parameter space they occupy next to their TSM or ESM value in brackets with host stellar type denoted by the colored circle. Each target's background color corresponds to its mass measurement and validation status: green targets are confirmed planets with mass measurements $>5\sigma$, yellow targets are confirmed planets with mass measurements $<5\sigma$ and TOIs that were independently confirmed over the course of our analysis, blue targets have been statistically validated by our analysis, orange targets are marginal validations (LPs and pFPs), red targets were deemed false positives by our analysis, and gray targets were deemed to have an inconclusive validation.

Chapter 5: Conclusions and Future Work

5.1 Conclusions

The results of this work probe the formation mechanisms of hot Jupiters through the use of nearby companion planets as a key observable to distinguish between possible formation pathways.

As shown in Chapter 2, large-scale searches for nearby companion planets to hot Jupiters have turned up very little in the way of new planets. This gives credence to the idea that most hot Jupiters formed via high-eccentricity migration since the dynamically-active formation history prescribed by high-eccentricity migration would eject or significantly disrupt the orbits of the planets interior to the hot Jupiter's original semi-major axis. That said, a lack of nearby companion planets to hot Jupiters is not a smoking gun for high-eccentricity migration in and of itself since other factors such as observational bias or high mutual inclination could preclude companion planets from transiting or being detected by TESS. However, when looking at hot Jupiters as an ensemble, such a dearth of companion planets does imply that high-eccentricity migration does play a major role in hot Jupiter formation, even if the formation pathway of a given individual system cannot be confidently determined. Indeed, previous studies have shown that it is most likely impossible that all hot Jupiters formed via high-eccentricity migration and some fraction must have formed through disk migration (Dawson et al., 2014). This conclusion is supported by the fact that not only do a small handful of hot Jupiters exist with nearby companion planets, but the calculated expected occurrence rate of such planets calculated in Chapter 2 suggests that potentially 1 in 5 transiting hot Jupiters could possess a transiting nearby companion planet.

As presented in Chapter 3, the discovery of additional hot Jupiter systems with companion planets is ongoing and as TESS continues its observations of the sky, additional examples of this rare system architecture will likely be found. Multiple sectors of TESS data were necessary for the discovery of WASP-132 c since one year's worth of TESS data alone provided an insufficient signal-to-noise ratio to allow for a confident detection and validation. Therefore, the discovery of WASP-132 c is just the beginning.

Already we are able to see some emerging trends in the sample of hot Jupiters with nearby companions. As discussed in Chapter 3, almost all currently known companions to hot Jupiters orbit interior to the hot Jupiter on orbits with periods between 1 and 5 days. This is consistent with a quiescent disk migration in the systems' evolutionary histories and may indicate that these planets migrated inwards together. What is not as obvious, however, is why only WASP-47 also possesses an exterior companion. If disk migration were the cause of the formation of these hot Jupiters, the expectation would be that the relative system architecture would remain intact over the course of the migration and the quiescent nature of this evolution cannot explain the dearth of exterior companions to hot Jupiters.

The resolution to this issue could be twofold. The first is that it's an observational effect. Since TESS observes the sky in sectors in duration of $\sim$28 days, it is possible that the searches for companion planets thus far have not been sensitive to exterior companions since a single TESS sector only allows for periods of up to 14 days to be discovered given that two transits are required to determine a planet's period. This means that since most of the hot Jupiters with companions orbit on periods in excess of 6 or 7 days, many of the potential exterior planets are not being detected due to the TESS observation strategy. The other resolution to this lack of exterior companions could be that hot Jupiter systems that form with exterior companions gradually have their orbital angular momentum leeched by these planets during close encounters until the hot Jupiter's orbit – which is already unstable to tidal decay – shrinks enough that it is engulfed by the host star. Therefore, it is not that hot Jupiters with exterior companions do not form, but rather the ones that do have already been engulfed by their host stars.

Additionally, another question raised by the distribution of hot Jupiters with nearby companions is why these hot Jupiters are not located at the $\sim$3 day orbital period pileup. As stated in Heller (2019), disk migration most likely places hot Jupiters within the range of this pileup and even hot Jupiters that form via high-eccentricity migration are acted upon by tidal forces to shrink their orbits to this range. Given that these hot Jupiters with companions likely formed via disk migration over high-eccentricity migration, it is puzzling why they would not be located within the observed $\sim$3 day pileup. It is possible that the $\sim$3 day pileup does not exist and can be attributed to a number of observational biases. This will require further investigation as the sample grows, as will the previous trends discussed in this section. Although the sample size presented in this dissertation numbers only four, additional systems have since been identified that fit this system architecture (TOI-2000, TOI-2494, TOI-5143) and they, too, fit this observed structure, thus extending the trend to a growing sample of greater than four.

As a result of this work, it is likely that high-eccentricity migration still dominates hot Jupiter formation, but there is mounting evidence that other formation pathways are required to adequately describe the observed hot Jupiter population. This may also imply that the distinction between warm Jupiters and hot Jupiters is not as stark as previously thought, and that a subpopulation of hot Jupiters may just be an extension of a warm Jupiter population in terms of formation and evolutionary history.

Furthermore, this work presents the synthesis of a best-in-class sample of planets most amenable to atmospheric characterization with JWST across parameter space. Included in this is a targeted large-scale validation of these best-in-class planet candidates that have been discovered by TESS.

Chapter 4 demonstrates that there are a great many targets that already exist for atmospheric characterization with JWST. Of these targets, a significant fraction – if not most – are TESS discoveries that have yet to be vetted and validated as planets and another significant subset of them are TESS discoveries that have already been confirmed as planets. It is imperative that these targets get the attention that they need to have the source of the signals determined as JWST observation time is a precious resource and there are plenty of excellent targets that have not received adequate attention.

By vetting and validating the TESS-discovered planet candidates the best-in-class sample generated, Chapter 4 will prove to be a valuable resource for future JWST observations and proposals. Indeed, not only will the newly-validated TESS discoveries prove to be useful for future JWST observations, but the entire sample of confirmed plus unconfirmed targets will be as well. Up to this point, there has yet to be a concerted effort to rank and prioritize targets for atmospheric characterization by observability in a manner agnostic to science case.

5.2 Future Work

In order to unlock the mysteries posed by the ever-growing sample of hot Jupiters with nearby companion planets, it is necessary to continue searching for these types of planets. TESS is already well into its second extended mission and is expected to operate for many years to come. This will provide invaluable additional data to not only increase the signal-to-noise ratio of many small companion planets that have yet to be discovered, but it may also help resolve the issue regarding the lack of observed exterior planetary companions. Additional observations of the same systems will increase the baseline of the periods that we are sensitive to and will allow us to probe both hot Jupiter systems already known to have companions and those without for the existence of longer-period companions. The Roman Space Telescope is expected to deliver thousands or tens of thousands of new transiting planets and reobserve many that are already known at higher photometric precision than TESS. This will undoubtedly provide a wealth of new hot Jupiters and potentially even smaller companion planets as well as unlock the ability to perform detailed demographic analysis of this rare system architecture. As the sample of hot Jupiters with nearby companions grows, new trends in this population may also emerge.

It will also be imperative to combine these transit searches with searches for companions through other methods. Since it is quite possible that companion planets may not transit, it will be necessary to search hot Jupiter systems using radial velocity techniques and also look for transit timing variations in hot Jupiter periods that would indicate the presence of additional bodies in the system. By capturing non-transiting parameter spaces of potential companions, we will be able to further refine the expected occurrence rate of nearby companions to hot Jupiters. This value is critical in understanding the contribution of each formation pathway to the ensemble of hot Jupiters. Extreme precision radial velocity (EPRV) capabilities in the near future will not only unlock this complementary parameter space but will provide the ability to characterize the nature of these companions to determine if they are rocky or gaseous in composition, which could lead to new revelations in their connection to hot Jupiter formation. This could potentially also discover even less massive companions and enhance our completeness down to even smaller and less dense planets.

This effort should be coupled with dynamical simulations to determine the rate at which companion planets survive the formation process through each formation pathway. Understanding this can help calibrate the anticipated contribution of each mechanism to the observed hot Jupiter population. For example, knowing the percentage of disk migration scenarios that destroy companion planets prior to their arrival at the current positions and assuming that all of the systems containing both hot Jupiters and companion planets formed via disk migration, the proportion of hot Jupiter plus companion systems to the whole hot Jupiter population can be extrapolated to determine how many systems form via disk migration, with or without planets.

As for the best-in-class sample: this set of targets will almost certainly change with time. As targets currently in this sample have their parameters refined, as new targets are discovered, and as planet candidates are deemed false positives, this list of targets most amenable for atmospheric characterization with JWST will shift and change. The process and code to generate this sample are replicable and the procedures for vetting and validating candidates that were used are fairly standard across the field. Therefore, it should not be difficult to periodically update this target list as new targets are discovered and old ones are altered.

One of the most pressing needs for this list, however, is a concerted effort to follow-up on the targets that were vetted and validated in Chapter 4. The targets that were statistically validated need to be followed up with radial velocity observations to obtain mass measurements. These mass measurements will be critical in not only confirming the planets but also in predicting what sorts of atmospheric features and sizes can be expected from observations with JWST. Additionally, following up the marginally validated targets with additional photometry, imaging, and reconnaissance spectroscopy will aid in determining the planetary nature of these targets. Many of the targets that were not statistically validated in Chapter 4 require further follow-up observations to investigate their true nature and, given the fact that they are all potentially fantastic targets for atmospheric characterization with JWST, they warrant additional attention and care to make sure potential prime targets are not overlooked. Additionally, the tools and methods developed in the synthesis of the best-in-class sample presented in Chapter 4 are applicable to future exoplanet observatories such as the Pandora SmallSat.

Appendix A: Facilities and Software Used in this Thesis

A.1 Facilities

1. Adams Observatory
2. ASP
3. Brierfield Private Observatory
4. Campo Catino Astronomical Observatory
5. Catania Astrophysical Observatory
6. Caucasian Mountain Observatory
7. CHAT
8. CHIRON
9. CORALIE
10. CROW Observatory
11. Deep Sky West
12. Dragonfly

13. El Sauce
14. ExTrA
15. FIES
16. Fred L. Whipple Observatory
17. Gaia
18. Gemini (‘Alopeke, Zorro)
19. George Mason University
20. HARPS-N
21. HAT-South
22. Hazelwood OBservatory
23. Kutztown University Observatory
24. Keck/HIRES
25. LCOGT
26. Lewin Observatory
27. Lick Observatory
28. Lookout Observatory
29. MASTER-Ural

30. MEarth-S

31. Mikulski Archive for Space Telescopes

32. Minerva-Australis

33. Mount Kent Observatory

34. Mt. Stuart Observatory

35. MuSCAT

36. MuSCAT2

37. MuSCAT3

38. NASA Exoplanet Archive

39. NRES

40. OAUV-TURIA2

41. Observatori Astonòmic Albanyà

42. Observatory de Ca l'Ou

43. Palomar Observatory

44. PEST

45. PFS

46. Privat Observatory Herges-Hallenberg

47. PvDKO
48. RCO
49. SAINT-EX
50. Salerno University Observatory
51. SOAR
52. SPECULOOS
53. SUTO-Otivar
54. TESS
55. TRAPPIST
56. TRES
57. ULMT
58. Union College Observatory
59. VLT
60. WASP
61. WCO
62. Wellesley College Whitin Observatory
63. WIYN

A.2 Software

1. AstroImageJ (Collins et al., 2017)
2. Astropy (Astropy Collaboration et al., 2013, 2018, 2022)
3. astroquery (Ginsburg et al., 2019)
4. `BANZAI` (McCully et al., 2018)
5. BATMAN (Kreidberg, 2015)
6. celerite (Foreman-Mackey et al., 2017; Foreman-Mackey, 2018)
7. DACE (`https://dace.unige.ch`)
8. DAVE (Kostov et al., 2019a)
9. DEATHSTAR (Ross et al., submitted)
10. eleanor (Feinstein et al., 2019)
11. exoplanet (Foreman-Mackey et al., 2019)
12. Jupyter (Kluyver et al., 2016)
13. Lightkurve (Lightkurve Collaboration et al., 2018b)
14. matplotlib (Hunter, 2007)
15. NumPy (Van Der Walt et al., 2011)
16. Pandas (McKinney, 2010)

17. PyMC3 (Salvatier et al., 2016b)

18. SciPy (Oliphant, 2007)

19. STARRY (Luger et al., 2019; Agol et al., 2019)

20. TAPIR (Jensen, 2013)

21. `TESS Transit Finder` (Jensen, 2013)

22. Tesscut (Brasseur et al., 2019b)

23. Theano (Theano Development Team, 2016)

24. Transit Least Squares (Hippke & Heller, 2019)

25. TRICERATOPS (Giacalone & Dressing, 2020b; Giacalone et al., 2021b)

26. REBOUND (Rein & Liu, 2012)

27. vespa (Morton, 2012b, 2015b)

Bibliography

Abraham, R. G., & van Dokkum, P. G. 2014, Publications of the Astronomical Society of the Pacific, 126, 55, doi: 10.1086/674875

Agol, E. 2011, The Astrophysical Journal Letters, 731, L31, doi: 10.1088/2041-8205/731/2/L31

Agol, E., Cowan, N. B., Knutson, H. A., et al. 2010, The Astrophysical Journal, 721, 1861, doi: 10.1088/0004-637X/721/2/1861

Agol, E., Luger, R., & Foreman-Mackey, D. 2019, arXiv e-prints

Ahrer, E.-M., Stevenson, K. B., Mansfield, M., et al. 2023, Nature, 614, 653, doi: 10.1038/s41586-022-05590-4

Albrecht, S., Winn, J. N., Johnson, J. A., et al. 2012, The Astrophysical Journal, 757, 18

Allard, F., Homeier, D., & Freytag, B. 2012, Philosophical Transactions of the Royal Society of London Series A, 370, 2765, doi: 10.1098/rsta.2011.0269

Almenara, J. M., Bonfils, X., Forveille, T., et al. 2022, Astronomy & Astrophysics, 667, L11, doi: 10.1051/0004-6361/202244791

Alonso, R., Deeg, H. J., Brown, T. M., & Belmonte, J. A. 2004, in ESA Special Publication, Vol. 538, Stellar Structure and Habitable Planet Finding, ed. F. Favata, S. Aigrain, & A. Wilson, 255–259

Anderson, K. R., Storch, N. I., & Lai, D. 2016, Monthly Notices of the Royal Astronomical Society, 456, 3671

Arcangeli, J., Désert, J.-M., Line, M. R., et al. 2018, The Astrophysical Journal Letters, 855, L30, doi: 10.3847/2041-8213/aab272

Astropy Collaboration, Robitaille, T. P., Tollerud, E. J., et al. 2013, Astronomy and Astrophysics, 558, A33, doi: 10.1051/0004-6361/201322068

Astropy Collaboration, Price-Whelan, A. M., Sipőcz, B. M., et al. 2018, The Astronomical Journal, 156, 123, doi: 10.3847/1538-3881/aabc4f

Astropy Collaboration, Price-Whelan, A. M., Lim, P. L., et al. 2022, apj, 935, 167, doi: 10.3847/1538-4357/ac7c74

August, P. C., Bean, J. L., Zhang, M., et al. 2023, arXiv e-prints, arXiv:2305.07753, doi: 10.48550/arXiv.2305.07753

Auvergne, M., Bodin, P., Boisnard, L., et al. 2009, Astronomy and Astrophysics, 506, 411, doi: 10.1051/0004-6361/200810860

Bailer-Jones, C. A. L., Rybizki, J., Fouesneau, M., Mantelet, G., & Andrae, R. 2018, The Astronomical Journal, 156, 58, doi: 10.3847/1538-3881/aacb21

Bakos, G., Noyes, R., Kovács, G., et al. 2004, Publications of the Astronomical Society of the Pacific, 116, 266

Bakos, G. Á. 2018, in Handbook of Exoplanets, ed. H. J. Deeg & J. A. Belmonte, 111, doi: 10.1007/978-3-319-55333-7_111

Bakos, G. Á., Csubry, Z., Penev, K., et al. 2013, Publications of the Astronomical Society of the Pacific, 125, 154, doi: 10.1086/669529

Baraffe, I., Chabrier, G., Allard, F., & Hauschildt, P. H. 1998, Astronomy and Astrophysics, 337, 403, doi: 10.48550/arXiv.astro-ph/9805009

Barclay, T., Pepper, J., & Quintana, E. V. 2018, The Astrophysical Journal Supplement Series, 239, 2

Barclay, T., Rowe, J. F., Lissauer, J. J., et al. 2013, Nature, 494, 452

Barman, T. S., Hauschildt, P. H., & Allard, F. 2001, The Astrophysical Journal, 556, 885

Barros, S. C. C., Demangeon, O. D. S., Armstrong, D. J., et al. 2023, Astronomy & Astrophysics, 673, A4, doi: 10.1051/0004-6361/202245741

Batalha, N. E., Lewis, T., Fortney, J. J., et al. 2019, The Astrophysical Journall, 885, L25, doi: 10.3847/2041-8213/ab4909

Batygin, K. 2012, Nature, 491, 418

Batygin, K., Bodenheimer, P. H., & Laughlin, G. P. 2016, The Astrophysical Journal, 829, 114

Bean, J. L., Kempton, E. M.-R., & Homeier, D. 2010, Nature, 468, 669

Bean, J. L., Xue, Q., August, P. C., et al. 2023, Nature, 618, 43

Becker, J. C., Vanderburg, A., Adams, F. C., Rappaport, S. A., & Schwengeler, H. M. 2015, The Astrophysical Journal Letters, 812, L18

Beichman, C., Benneke, B., Knutson, H., et al. 2014, Publications of the Astronomical Society of the Pacific, 126, 1134, doi: 10.1086/679566

Beleznay, M., & Kunimoto, M. 2022, Monthly Notices of the Royal Astronomical Society, 516, 75

Bell, T. J., Kreidberg, L., Kendrew, S., et al. 2023, arXiv e-prints, arXiv:2301.06350, doi: 10.48550/arXiv.2301.06350

Bellm, E. C., Kulkarni, S. R., Graham, M. J., et al. 2019, Publications of the Astronomical Society of the Pacific, 131, 018002, doi: 10.1088/1538-3873/aaecbe

Berger, T. A., Huber, D., van Saders, J. L., et al. 2020, The Astronomical Journal, 159, 280, doi: 10.3847/1538-3881/159/6/280

Bonfils, X., Almenara, J. M., Jocou, L., et al. 2015, in Society of Photo-Optical Instrumentation Engineers (SPIE) Conference Series, Vol. 9605, Techniques and Instrumentation for Detection of Exoplanets VII, ed. S. Shaklan, 96051L, doi: 10.1117/12.2186999

Borucki, W. J., & Summers, A. L. 1984, Icarus, 58, 121

Borucki, W. J., Koch, D., Basri, G., et al. 2010, Science, 327, 977

Borucki, W. J., Koch, D., Basri, G., et al. 2010, Science, 327, 977, doi: 10.1126/science.1185402

Boss, A. P. 1997, Science, 276, 1836, doi: 10.1126/science.276.5320.1836

Bovy, J., Rix, H.-W., Green, G. M., Schlafly, E. F., & Finkbeiner, D. P. 2016, The Astrophysical Journal, 818, 130, doi: 10.3847/0004-637X/818/2/130

Brasseur, C. E., Phillip, C., Fleming, S. W., Mullally, S. E., & White, R. L. 2019a, Astrocut: Tools for creating cutouts of TESS images. http://ascl.net/1905.007

—. 2019b, Astrocut: Tools for creating cutouts of TESS images, Astrophysics Source Code Library, record ascl:1905.007. http://ascl.net/1905.007

Brown, A., Vallenari, A., Prusti, T., et al. 2018, Astronomy & astrophysics, 616, A1

Brown, A. G., Vallenari, A., Prusti, T., et al. 2021, Astronomy & Astrophysics, 649, A1

Brown, T. M. 2003, The Astrophysical Journal Letters, 593, L125, doi: 10.1086/378310

Brown, T. M., Charbonneau, D., Gilliland, R. L., Noyes, R. W., & Burrows, A. 2001, The Astrophysical Journal, 552, 699, doi: 10.1086/320580

Brown, T. M., Baliber, N., Bianco, F. B., et al. 2013a, Publications of the Astronomical Society of the Pacific, 125, 1031, doi: 10.1086/673168

—. 2013b, Publications of the Astronomical Society of the Pacific, 125, 1031, doi: 10.1086/673168

Bryson, S. T., Jenkins, J. M., Gilliland, R. L., et al. 2013, Publications of the Astronomical Society of the Pacific, 125, 889, doi: 10.1086/671767

Buchhave, L. A., Bakos, G. Á., Hartman, J. D., et al. 2010, The Astrophysical Journal, 720, 1118, doi: 10.1088/0004-637X/720/2/1118

Buchhave, L. A., Latham, D., Johansen, A., et al. 2012, Nature, 486, 375

Cañas, C. I., Kanodia, S., Bender, C. F., et al. 2022, The Astronomical Journal, 164, 50, doi: 10.3847/1538-3881/ac7804

Cacciapuoti, L., Kostov, V. B., Kuchner, M., et al. 2022, Monthly Notices of the Royal Astronomical Society, 513, 102, doi: 10.1093/mnras/stac652

Cameron, A. C. 2012, Nature, 492, 48

Cañas, C. I., Wang, S., Mahadevan, S., et al. 2019, The Astrophysical Journal Letters, 870, L17

Chang, S.-H., Gu, P.-G., & Bodenheimer, P. 2009, The Astrophysical Journal, 708, 1692

Changeat, Q., Edwards, B., Al-Refaie, A. F., et al. 2022, The Astrophysical Journal, Supplement, 260, 3, doi: 10.3847/1538-4365/ac5cc2

Charbonneau, D., Brown, T. M., Dunham, E. W., et al. 2004, in American Institute of Physics Conference Series, Vol. 713, The Search for Other Worlds, ed. S. S. Holt & D. Deming, 151–160, doi: 10.1063/1.1774515

Charbonneau, D., Brown, T. M., Latham, D. W., & Mayor, M. 1999a, The Astrophysical Journal Letters, 529, L45

Charbonneau, D., Brown, T. M., Noyes, R. W., & Gilliland, R. L. 2002a, The Astrophysical Journal, 568, 377, doi: 10.1086/338770

—. 2002b, The Astrophysical Journal, 568, 377, doi: 10.1086/338770

Charbonneau, D., Noyes, R. W., Korzennik, S. G., et al. 1999b, The Astrophysical Journal, 522, L145

Charbonneau, D., Allen, L. E., Megeath, S. T., et al. 2005, The Astrophysical Journal, 626, 523, doi: 10.1086/429991

Chatterjee, S., Ford, E. B., Matsumura, S., & Rasio, F. A. 2008, The Astrophysical Journal, 686, 580

Chaturvedi, P., Bluhm, P., Nagel, E., et al. 2022, Astronomy & Astrophysics, 666, A155, doi: 10.1051/0004-6361/202244056

Chen, J., & Kipping, D. 2016, The Astrophysical Journal, 834, 17

Chen, J., & Kipping, D. 2017, The Astrophysical Journal, 834, 17, doi: 10.3847/1538-4357/834/1/17

Ciardi, D. R., Beichman, C. A., Horch, E. P., & Howell, S. B. 2015, The Astrophysical Journal, 805, 16, doi: 10.1088/0004-637X/805/1/16

Collier Cameron, A., Horne, K., Penny, A., & James, D. 1999, Nature, 402, 751, doi: 10.1038/45451

Collier Cameron, A., Pollacco, D., Hellier, C., et al. 2009, in Transiting Planets, ed. F. Pont, D. Sasselov, & M. J. Holman, Vol. 253, 29–35, doi: 10.1017/S1743921308026203

Collins, K. 2019, in American Astronomical Society Meeting Abstracts, Vol. 233, American Astronomical Society Meeting Abstracts #233, 140.05

Collins, K. A., Kielkopf, J. F., Stassun, K. G., & Hessman, F. V. 2017, The Astronomical Journal, 153, 77, doi: 10.3847/1538-3881/153/2/77

Collins, K. A., Collins, K. I., Pepper, J., et al. 2018, The Astronomical Journal, 156, 234, doi: 10.3847/1538-3881/aae582

Colón, K. D., & Ford, E. B. 2011, Publications of the Astronomical Society of the Pacific, 123, 1391, doi: 10.1086/663352

Coughlin, J. L., Thompson, S. E., Bryson, S. T., et al. 2014a, The Astronomical Journal, 147, 119, doi: 10.1088/0004-6256/147/5/119

—. 2014b, The Astronomical Journal, 147, 119, doi: 10.1088/0004-6256/147/5/119

Crossfield, I. J., Hansen, B. M., Harrington, J., et al. 2010, The Astrophysical Journal, 723, 1436

Crossfield, I. J. M., Waalkes, W., Newton, E. R., et al. 2019, The Astrophysical Journal Letters, 883, L16, doi: 10.3847/2041-8213/ab3d30

Cutri, R. M., Wright, E. L., Conrow, T., et al. 2013, Explanatory Supplement to the AllWISE Data Release Products, Tech. rep.

Dawson, R. I., & Johnson, J. A. 2012, The Astrophysical Journal, 756, 122

—. 2018, Annual Review of Astronomy and Astrophysics, 56, 175

Dawson, R. I., Murray-Clay, R. A., & Johnson, J. A. 2014, The Astrophysical Journal, 798, 66

de Leon, J. P., Livingston, J., Endl, M., et al. 2021, Monthly Notices of the Royal Astronomical Society, 508, 195, doi: 10.1093/mnras/stab2305

Deeg, H. J., & Alonso, R. 2018, in Handbook of Exoplanets, ed. H. J. Deeg & J. A. Belmonte, 117, doi: 10.1007/978-3-319-55333-7_117

Deming, D., Seager, S., Richardson, L. J., & Harrington, J. 2005, Nature, 434, 740, doi: 10.1038/nature03507

Deming, D., Seager, S., Winn, J., et al. 2009, Publications of the Astronomical Society of the Pacific, 121, 952, doi: 10.1086/605913

Demory, B. O., Pozuelos, F. J., Gómez Maqueo Chew, Y., et al. 2020, Astronomy and Astrophysics, 642, A49, doi: 10.1051/0004-6361/202038616

Desidera, S., Damasso, M., Gratton, R., et al. 2022, arXiv e-prints, arXiv:2210.07933, doi: 10.48550/arXiv.2210.07933

Dieterich, S. B., Henry, T. J., Jao, W.-C., et al. 2014, The Astronomical Journal, 147, 94, doi: 10.1088/0004-6256/147/5/94

Djupvik, A. A., & Andersen, J. 2010, Astrophysics and Space Science Proceedings, 14, 211, doi: 10.1007/978-3-642-11250-8_21

Drake, A. J., Beshore, E., Catelan, M., et al. 2010, arXiv e-prints, arXiv:1009.3048, doi: 10.48550/arXiv.1009.3048

Dressing, C., Giacalone, S., Savel, A., et al. in prep.

Duffell, P. C., & Chiang, E. 2015, The Astrophysical Journal, 812, 94, doi: 10.1088/0004-637X/812/2/94

Durisen, R. H., Boss, A. P., Mayer, L., et al. 2007, in Protostars and Planets V, ed. B. Reipurth, D. Jewitt, & K. Keil, 607, doi: 10.48550/arXiv.astro-ph/0603179

Eaton, J. A. 1993, The Astrophysical Journal, 404, 305, doi: 10.1086/172280

Edwards, B., Changeat, Q., Mori, M., et al. 2020, The Astronomical Journal, 161, 44

Endl, M., Caldwell, D. A., Barclay, T., et al. 2014, The Astrophysical Journal, 795, 151

Evans, T. M., & Sackett, P. D. 2010, The Astrophysical Journal, 712, 38, doi: 10.1088/0004-637X/712/1/38

ExoFOP. 2019, Exoplanet Follow-up Observing Program - TESS, IPAC

Fabrycky, D., & Tremaine, S. 2007, The Astrophysical Journal, 669, 1298, doi: 10.1086/521702

Faedi, F., West, R. G., Burleigh, M. R., Goad, M. R., & Hebb, L. 2011, Monthly Notices of the Royal Astronomical Society, 410, 899, doi: 10.1111/j.1365-2966.2010.17488.x

Feinstein, A. D., Montet, B. T., Foreman-Mackey, D., et al. 2019, arXiv preprint arXiv:1903.09152

Fűrész, G. 2008, PhD thesis, University of Szeged, Hungary

Fogg, M. J., & Nelson, R. P. 2007, Astronomy & Astrophysics, 461, 1195

Ford, E. B., & Rasio, F. A. 2006, The Astrophysical Journal, 638, L45

Foreman-Mackey, D. 2018, Research Notes of the American Astronomical Society, 2, 31, doi: 10.3847/2515-5172/aaaf6c

Foreman-Mackey, D., Agol, E., Ambikasaran, S., & Angus, R. 2017, The Astronomical Journal, 154, 220

Foreman-Mackey, D., Czekala, I., Luger, R., et al. 2019, dfm/exoplanet v0.2.3, doi: 10.5281/zenodo.1998447

Foreman-Mackey, D., Hogg, D. W., Lang, D., & Goodman, J. 2013, Publications of the Astronomical Society of the Pacific, 125, 306, doi: 10.1086/670067

Fortney, J. J., Dawson, R. I., & Komacek, T. D. 2021, Journal of Geophysical Research: Planets, 126, e2020JE006629

Fortney, J. J., Mordasini, C., Nettelmann, N., et al. 2013, The Astrophysical Journal, 775, 80, doi: 10.1088/0004-637X/775/1/80

Fu, G., Espinoza, N., Sing, D. K., et al. 2022, The Astrophysical Journal Letters, 940, L35

Fukui, A., Narita, N., Tristram, P. J., et al. 2011, Publications of the Astronomical Society of Japan, 63, 287, doi: 10.1093/pasj/63.1.287

Furlan, E., Ciardi, D. R., Everett, M. E., et al. 2017, The Astronomical Journal, 153, 71, doi: 10.3847/1538-3881/153/2/71

Gaia Collaboration, Brown, A. G. A., Vallenari, A., et al. 2018, Astronomy & Astrophysics, 616, A1, doi: 10.1051/0004-6361/201833051

Gan, T., Wang, S. X., Wang, S., et al. 2022, The Astronomical Journal, 165, 17

Gao, P., Thorngren, D. P., Lee, E. K., et al. 2020, Nature Astronomy, 4, 951

Garcia, L. J., Timmermans, M., Pozuelos, F. J., et al. 2022, Monthly Notices of the Royal Astronomical Society, 509, 4817, doi: 10.1093/mnras/stab3113

Gardner, J. P., Mather, J. C., Clampin, M., et al. 2006, Space Science Reviews, 123, 485, doi: 10.1007/s11214-006-8315-7

Gardner, J. P., Mather, J. C., Abbott, R., et al. 2023, arXiv e-prints, arXiv:2304.04869, doi: 10.48550/arXiv.2304.04869

Garhart, E., Deming, D., Mandell, A., et al. 2020, The Astronomical Journal, 159, 137

Gaudi, B. S., Seager, S., & Mallen-Ornelas, G. 2005, The Astrophysical Journal, 623, 472, doi: 10.1086/428478

Giacalone, S., & Dressing, C. D. 2020a, triceratops: Candidate exoplanet rating tool. http://ascl.net/2002.004

—. 2020b, triceratops: Candidate exoplanet rating tool. http://ascl.net/2002.004

Giacalone, S., Dressing, C. D., Jensen, E. L. N., et al. 2021a, The Astronomical Journal, 161, 24, doi: 10.3847/1538-3881/abc6af

—. 2021b, The Astronomical Journal, 161, 24, doi: 10.3847/1538-3881/abc6af

Gilbert, E. A., Barclay, T., Schlieder, J. E., et al. 2020, The Astronomical Journal, 160, 116

Gilbert, E. A., Barclay, T., Schlieder, J. E., et al. 2020a, The Astronomical Journal, 160, 116, doi: 10.3847/1538-3881/aba4b2

—. 2020b, The Astronomical Journal, 160, 116, doi: 10.3847/1538-3881/aba4b2

Ginsburg, A., Sipőcz, B. M., Brasseur, C. E., et al. 2019, The Astronomical Journal, 157, 98, doi: 10.3847/1538-3881/aafc33

Girardi, L., Groenewegen, M., Hatziminaoglou, E., & Da Costa, L. 2005, Astronomy & Astrophysics, 436, 895

Girardi, L., Barbieri, M., Groenewegen, M. A., et al. 2012, in Red Giants as Probes of the Structure and Evolution of the Milky Way, Springer, 165–170

Goldreich, P., Lithwick, Y., & Sari, R. 2004, Annu. Rev. Astron. Astrophys., 42, 549

Goldreich, P., & Tremaine, S. 1980, The Astrophysical Journal, 241, 425, doi: 10.1086/158356

Greene, T. P., Bell, T. J., Ducrot, E., et al. 2023, Nature, 618, 39, doi: 10.1038/s41586-023-05951-7

Greene, T. P., Line, M. R., Montero, C., et al. 2016, The Astrophysical Journal, 817, 17, doi: 10.3847/0004-637X/817/1/17

Guerrero, N. M., Seager, S., Huang, C. X., et al. 2021, The Astrophysical Journal Supplement Series, 254, 39

Haghighipour, N., Vogt, S. S., Butler, R. P., et al. 2010, The Astrophysical Journal, 715, 271, doi: 10.1088/0004-637X/715/1/271

Hara, N. C., & Ford, E. B. 2023, Annual Review of Statistics and Its Application, 10, 623

Haswell, C. A. 2010, Transiting Exoplanets

Hawthorn, F., Bayliss, D., Wilson, T. G., et al. 2023, Monthly Notices of the Royal Astronomical Society, 520, 3649, doi: 10.1093/mnras/stad306

Hébrard, G., Díaz, R., Correia, A., et al. 2020, Astronomy & Astrophysics, 640, A32

Hedges, C., Saunders, N., Barentsen, G., et al. 2019, The Astrophysical Journal Letters, 880, L5, doi: 10.3847/2041-8213/ab2a74

Heller, R. 2019, Astronomy & Astrophysics, 628, A42

Heller, R., Hippke, M., & Rodenbeck, K. 2019, Astronomy & Astrophysics, 627, A66

Hellier, C., Anderson, D. R., Collier Cameron, A., et al. 2017, Monthly Notices of the Royal Astronomical Society, 465, 3693, doi: 10.1093/mnras/stw3005

Henden, A. A., Templeton, M., Terrell, D., et al. 2016, VizieR Online Data Catalog, 2336

Henry, G. W., Marcy, G. W., Butler, R. P., & Vogt, S. S. 1999, The Astrophysical Journal Letters, 529, L41

Hippke, M., & Heller, R. 2019, Astronomy & Astrophysics, 623, A39, doi: 10.1051/0004-6361/201834672

Hippke, M., & Heller, R. 2019, arXiv preprint arXiv:1901.02015

Hobson, M. J., Jordán, A., Bryant, E. M., et al. 2023, The Astrophysical Journall, 946, L4, doi: 10.3847/2041-8213/acbd9a

Hoffman, M. D., Gelman, A., et al. 2014, J. Mach. Learn. Res., 15, 1593

Hord, B. J., Colón, K. D., Kostov, V., et al. 2021, The Astronomical Journal, 162, 263

Hord, B. J., Colón, K. D., Kostov, V., et al. 2021, The Astronomical Journal, 162, 263, doi: 10.3847/1538-3881/ac2602

Hord, B. J., Colón, K. D., Berger, T. A., et al. 2022, The Astronomical Journal, 164, 13, doi: 10.3847/1538-3881/ac6f57

Howard, A. W., Marcy, G. W., Bryson, S. T., et al. 2012, The Astrophysical Journal Supplement Series, 201, 15, doi: 10.1088/0067-0049/201/2/15

Howell, S. B., Everett, M. E., Sherry, W., Horch, E., & Ciardi, D. R. 2011, The Astronomical Journal, 142, 19

Howell, S. B., & Furlan, E. 2022, Frontiers in Astronomy and Space Sciences, 9, 871163, doi: 10.3389/fspas.2022.871163

Howell, S. B., Sobeck, C., Haas, M., et al. 2014, Publications of the Astronomical Society of the Pacific, 126, 398

Howell, S. B., Sobeck, C., Haas, M., et al. 2014, Publications of the Astronomical Society of the Pacific, 126, 398, doi: 10.1086/676406

Huang, C., Wu, Y., & Triaud, A. H. 2016, The Astrophysical Journal, 825, 98

Huang, C. X., Quinn, S. N., Vanderburg, A., et al. 2020a, The Astrophysical Journal Letters, 892, L7

Huang, C. X., Vanderburg, A., Pál, A., et al. 2020b, Research Notes of the AAS, 4, 204

—. 2020c, Research Notes of the AAS, 4, 206

Hubbard, W., Fortney, J., Lunine, J., et al. 2001, The Astrophysical Journal, 560, 413

Huber, D., Zinn, J., Bojsen-Hansen, M., et al. 2017, The Astrophysical Journal, 844, 102, doi: 10.3847/1538-4357/aa75ca

Huber, D., White, T. R., Metcalfe, T. S., et al. 2022, The Astronomical Journal, 163, 79, doi: 10.3847/1538-3881/ac3000

Hunter, J. D. 2007, Computing in science & engineering, 9, 90

Ida, S., & Lin, D. N. C. 2008, The Astrophysical Journal, 673, 487, doi: 10.1086/523754

Ida, S., Lin, D. N. C., & Nagasawa, M. 2013, The Astrophysical Journal, 775, 42, doi: 10.1088/0004-637X/775/1/42

Irwin, J., Irwin, M., Aigrain, S., et al. 2007, Monthly Notices of the Royal Astronomical Society, 375, 1449, doi: 10.1111/j.1365-2966.2006.11408.x

Ivshina, E. S., & Winn, J. N. 2022, arXiv preprint arXiv:2202.03401

Jackson, B., Greenberg, R., & Barnes, R. 2008, The Astrophysical Journal, 678, 1396, doi: 10.1086/529187

Jehin, E., Gillon, M., Queloz, D., et al. 2011, The Messenger, 145, 2

Jenkins, J. M. 2002, The Astrophysical Journal, 575, 493, doi: 10.1086/341136

Jenkins, J. M. 2002, The Astrophysical Journal, 575, 493

Jenkins, J. M., Doyle, L. R., & Cullers, D. 1996, Icarus, 119, 244

Jenkins, J. M., Tenenbaum, P., Seader, S., et al. 2017, ksci, 9

—. 2020, Kepler Data Processing Handbook (KSCI-19081-003): Transiting Planet Search

Jenkins, J. M., Chandrasekaran, H., McCauliff, S. D., et al. 2010, in Society of Photo-Optical Instrumentation Engineers (SPIE) Conference Series, Vol. 7740, Software and Cyberinfrastructure for Astronomy, ed. N. M. Radziwill & A. Bridger, 77400D, doi: 10.1117/12.856764

Jenkins, J. M., Twicken, J. D., McCauliff, S., et al. 2016, in Proceedings of the Society of Photo-Optical Instrumentation Engineers, Vol. 9913, Software and Cyberinfrastructure for Astronomy IV, 99133E, doi: 10.1117/12.2233418

Jenkins, J. M., Twicken, J. D., McCauliff, S., et al. 2016, in Software and Cyberinfrastructure for Astronomy IV, Vol. 9913, International Society for Optics and Photonics, 99133E

Jenkins, J. M., Twicken, J. D., McCauliff, S., et al. 2016, in Proceedings of the Society of Photo-Optical Instrumentation Engineers, Vol. 9913, Software and Cyberinfrastructure for Astronomy IV, 99133E, doi: 10.1117/12.2233418

Jensen, E. 2013, Tapir: A web interface for transit/eclipse observability, Astrophysics Source Code Library. http://ascl.net/1306.007

Johnson, J. A., Bowler, B. P., Howard, A. W., et al. 2010, The Astrophysical Journal Letters, 721, L153

Jurić, M., & Tremaine, S. 2008, The Astrophysical Journal, 686, 603, doi: 10.1086/590047

JWST Transiting Exoplanet Community Early Release Science Team, Ahrer, E.-M., Alderson, L., et al. 2023, Nature, 614, 649, doi: 10.1038/s41586-022-05269-w

Kempton, E. M. R., Bean, J. L., Louie, D. R., et al. 2018, Publications of the Astronomical Society of the Pacific, 130, 114401, doi: 10.1088/1538-3873/aadf6f

Kempton, E. M. R., Zhang, M., Bean, J. L., et al. 2023, arXiv e-prints, arXiv:2305.06240, doi: 10.48550/arXiv.2305.06240

Kendrew, S., Scheithauer, S., Bouchet, P., et al. 2015, Publications of the Astronomical Society of the Pacific, 127, 623

Kendrew, S., Scheithauer, S., Bouchet, P., et al. 2016, in Society of Photo-Optical Instrumentation Engineers (SPIE) Conference Series, Vol. 9904, Space Telescopes and Instrumentation 2016: Optical, Infrared, and Millimeter Wave, ed. H. A. MacEwen, G. G. Fazio, M. Lystrup, N. Batalha, N. Siegler, & E. C. Tong, 990443, doi: 10.1117/12.2232887

Kipping, D. M. 2013a, Monthly Notices of the Royal Astronomical Society, 435, 2152

—. 2013b, Monthly Notices of the Royal Astronomical Society: Letters, 434, L51

Kluyver, T., Ragan-Kelley, B., Pérez, F., et al. 2016, Jupyter Notebooks-a publishing format for reproducible computational workflows., Vol. 2016

Knutson, H. A., Charbonneau, D., Allen, L. E., Burrows, A., & Megeath, S. T. 2008, The Astrophysical Journal, 673, 526, doi: 10.1086/523894

Knutson, H. A., Charbonneau, D., Allen, L. E., et al. 2007, Nature, 447, 183

Knutson, H. A., Fulton, B. J., Montet, B. T., et al. 2014, The Astrophysical Journal, 785, 126

Kostov, V. B., Mullally, S. E., Quintana, E. V., et al. 2019a, The Astronomical Journal, 157, 124

Kostov, V. B., Schlieder, J. E., Barclay, T., et al. 2019b, The Astronomical Journal, 158, 32, doi: 10.3847/1538-3881/ab2459

Kovács, G., Zucker, S., & Mazeh, T. 2002, Astronomy & Astrophysics, 391, 369

Kozai, Y. 1962, The Astronomical Journal, 67, 591, doi: 10.1086/108790

Kramer, M. 2018, in Handbook of Exoplanets, ed. H. J. Deeg & J. A. Belmonte, 5, doi: 10.1007/978-3-319-55333-7_5

Kreidberg, L. 2015, Publications of the Astronomical Society of the Pacific, 127, 1161

Kreidberg, L. 2018, in Handbook of Exoplanets, ed. H. J. Deeg & J. A. Belmonte, 100, doi: 10.1007/978-3-319-55333-7_100

Kreidberg, L., Bean, J. L., Désert, J.-M., et al. 2014, Nature, 505, 69, doi: 10.1038/nature12888

Krishnamurthy, A., Villasenor, J., Seager, S., Ricker, G., & Vanderspek, R. 2019, Acta Astronautica, 160, 46, doi: 10.1016/j.actaastro.2019.04.016

Kruse, E., Agol, E., Luger, R., & Foreman-Mackey, D. 2019, The Astrophysical Journal Supplement Series, 244, 11

Kurucz, R. L. 1992, in The Stellar Populations of Galaxies, ed. B. Barbuy & A. Renzini, Vol. 149, 225

Lai, D. 2015, in IAU General Assembly, Vol. 29, 2255633

Lecar, M., & Sasselov, D. D. 2003, The Astrophysical Journal, 596, L99

Lee, E. J., & Chiang, E. 2017, The Astrophysical Journal, 842, 40

Lee, E. J., Chiang, E., & Ormel, C. W. 2014, The Astrophysical Journal, 797, 95

Lee, M. H., & Peale, S. J. 2002, The Astrophysical Journal, 567, 596

Léger, A., Rouan, D., Schneider, J., et al. 2009, Astronomy and Astrophysics, 506, 287, doi: 10.1051/0004-6361/200911933

Li, J., Tenenbaum, P., Twicken, J. D., et al. 2019a, Publications of the Astronomical Society of the Pacific, 131, 024506, doi: 10.1088/1538-3873/aaf44d

—. 2019b, Publications of the Astronomical Society of the Pacific, 131, 024506, doi: 10.1088/1538-3873/aaf44d

Lidov, M. L. 1962, Planetary Space Science, 9, 719, doi: 10.1016/0032-0633(62)90129-0

Lightkurve Collaboration, Cardoso, J. V. d. M., Hedges, C., et al. 2018a, Lightkurve: Kepler and TESS time series analysis in Python, Astrophysics Source Code Library. http://ascl.net/1812.013

—. 2018b, Lightkurve: Kepler and TESS time series analysis in Python, Astrophysics Source Code Library. http://ascl.net/1812.013

Lillo-Box, J., Gandolfi, D., Armstrong, D. J., et al. 2023, Astronomy & Astrophysics, 669, A109, doi: 10.1051/0004-6361/202243879

Lin, D. N., Bodenheimer, P., & Richardson, D. C. 1996, Nature, 380, 606

Lin, D. N. C., & Papaloizou, J. 1986, The Astrophysical Journal, 309, 846, doi: 10.1086/164653

Line, M. R., Wolf, A. S., Zhang, X., et al. 2013, The Astrophysical Journal, 775, 137, doi: 10.1088/0004-637X/775/2/137

Line, M. R., Stevenson, K. B., Bean, J., et al. 2016, The Astronomical Journal, 152, 203

Lipunov, V., Kornilov, V., Gorbovskoy, E., et al. 2012, in Astronomical Society of India Conference Series, Vol. 7, Astronomical Society of India Conference Series, 275

Lissauer, J. J., Ragozzine, D., Fabrycky, D. C., et al. 2011, The Astrophysical Journal Supplement Series, 197, 8

Lissauer, J. J., Marcy, G. W., Rowe, J. F., et al. 2012a, The Astrophysical Journal, 750, 112, doi: 10.1088/0004-637X/750/2/112

—. 2012b, The Astrophysical Journal, 750, 112, doi: 10.1088/0004-637X/750/2/112

Lissauer, J. J., Marcy, G. W., Bryson, S. T., et al. 2014, The Astrophysical Journal, 784, 44, doi: 10.1088/0004-637X/784/1/44

Livingston, J., & et al. in prep.

Louie, D. R., Deming, D., Albert, L., et al. 2018, Publications of the Astronomical Society of the Pacific, 130, 044401

Lovis, C., & Fischer, D. A. 2011, Radial Velocity Techniques for Exoplanets; Seager, S., Ed.; University of Arizona Press: Tucson, AZ, USA

Luger, R., Agol, E., Foreman-Mackey, D., et al. 2019, The astronomical journal, 157, 64

Luger, R., Agol, E., Foreman-Mackey, D., et al. 2019, aj, 157, 64, doi: 10.3847/1538-3881/aae8e5

Lustig-Yaeger, J., Fu, G., May, E. M., et al. 2023, arXiv e-prints, arXiv:2301.04191, doi: 10.48550/arXiv.2301.04191

Maciejewski, G. 2020, arXiv e-prints, arXiv:2010.11977. https://arxiv.org/abs/2010.11977

Madhusudhan, N. 2019, Annual Review of Astronomy and Astrophysics, 57, 617, doi: 10.1146/annurev-astro-081817-051846

Malhotra, R. 1993, Nature, 365, 819

Mamajek, E. E., & Hillenbrand, L. A. 2008, The Astrophysical Journal, 687, 1264

Mandushev, G., Torres, G., Latham, D. W., et al. 2005, The Astrophysical Journal, 621, 1061, doi: 10.1086/427727

Mansfield, M., Line, M. R., Bean, J. L., et al. 2021, Nature Astronomy, 5, 1224, doi: 10.1038/s41550-021-01455-4

Mayor, M., & Queloz, D. 1995, Nature, 378, 355

Mazeh, T. 2008, in EAS Publications Series, Vol. 29, EAS Publications Series, ed. M. J. Goupil & J. P. Zahn, 1–65, doi: 10.1051/eas:0829001

McCully, C., Daily, M., Brandt, G. M., et al. 2022, in Society of Photo-Optical Instrumentation Engineers (SPIE) Conference Series, Vol. 12189, Society of Photo-Optical Instrumentation Engineers (SPIE) Conference Series, 1218914, doi: 10.1117/12.2630667

McCully, C., Volgenau, N. H., Harbeck, D.-R., et al. 2018, in Society of Photo-Optical Instrumentation Engineers (SPIE) Conference Series, Vol. 10707, Proceedings of the Society of Photo-Optical Instrumentation Engineers, 107070K, doi: 10.1117/12.2314340

McKinney, W. 2010, in Proceedings of the 9th Python in Science Conference, ed. S. van der Walt & J. Millman, 51 – 56

Miles, B. E., Biller, B. A., Patapis, P., et al. 2023, The Astrophysical Journal Letters, 946, L6, doi: 10.3847/2041-8213/acb04a

Miller, N., & Fortney, J. J. 2011, The Astrophysical Journal Letters, 736, L29

Mistry, P., & et al. in prep.

Mizuno, H. 1980, Progress of Theoretical Physics, 64, 544

Mollière, P., Molyarova, T., Bitsch, B., et al. 2022, The Astrophysical Journal, 934, 74, doi: 10.3847/1538-4357/ac6a56

Morton, T. D. 2012a, The Astrophysical Journal, 761, 6, doi: 10.1088/0004-637X/761/1/6

—. 2012b, The Astrophysical Journal, 761, 6, doi: 10.1088/0004-637X/761/1/6

—. 2015a, VESPA: False positive probabilities calculator, Astrophysics Source Code Library. http://ascl.net/1503.011

—. 2015b, VESPA: False positive probabilities calculator, Astrophysics Source Code Library. http://ascl.net/1503.011

Morton, T. D., Giacalone, S., & Bryson, S. 2023, Research Notes of the AAS, 7, 107

Moutou, C., Deleuil, M., Guillot, T., et al. 2013, Icarus, 226, 1625, doi: 10.1016/j.icarus.2013.03.022

Muñoz, D. J., Lai, D., & Liu, B. 2016, Monthly Notices of the Royal Astronomical Society, 460, 1086

Murgas, F., Nowak, G., Masseron, T., et al. 2022, Astronomy & Astrophysics, 668, A158, doi: 10.1051/0004-6361/202244459

Mustill, A. J., Davies, M. B., & Johansen, A. 2015, The Astrophysical Journal, 808, 14

Naoz, S. 2016, Annual Review of Astronomy and Astrophysics, 54, 441, doi: 10.1146/annurev-astro-081915-023315

Naoz, S., Farr, W. M., Lithwick, Y., Rasio, F. A., & Teyssandier, J. 2011, Nature, 473, 187, doi: 10.1038/nature10076

Naponiello, L., & et al. accepted, Nature

Narita, N., Fukui, A., Kusakabe, N., et al. 2015, Journal of Astronomical Telescopes, Instruments, and Systems, 1, 045001, doi: 10.1117/1.JATIS.1.4.045001

Narita, N., Fukui, A., Kusakabe, N., et al. 2019, J. Astron. Telesc. Instruments, Syst., 5, 015001, doi: 10.1117/1.JATIS.5.1.015001

Narita, N., Fukui, A., Yamamuro, T., et al. 2020, in Society of Photo-Optical Instrumentation Engineers (SPIE) Conference Series, Vol. 11447, Society of Photo-Optical Instrumentation Engineers (SPIE) Conference Series, 114475K, doi: 10.1117/12.2559947

Nelson, B. E., Ford, E. B., & Rasio, F. A. 2017, The Astronomical Journal, 154, 106, doi: 10.3847/1538-3881/aa82b3

Niţu, I. C., Keith, M. J., Stappers, B. W., Lyne, A. G., & Mickaliger, M. B. 2022, Monthly Notices of the Royal Astronomical Society, 512, 2446, doi: 10.1093/mnras/stac593

O'Donovan, F. T., Charbonneau, D., Torres, G., et al. 2006, The Astrophysical Journal, 644, 1237, doi: 10.1086/503740

O'Donovan, F. T., Charbonneau, D., Alonso, R., et al. 2007, The Astrophysical Journal, 662, 658, doi: 10.1086/513684

Ogihara, M., Inutsuka, S.-i., & Kobayashi, H. 2013, The Astrophysical Journal Letters, 778, L9

Ogihara, M., Kobayashi, H., & Inutsuka, S.-i. 2014, The Astrophysical Journal, 787, 172

Oliphant, T. E. 2007, Computing in Science Engineering, 9, 10, doi: 10.1109/MCSE.2007.58

Osborn, H., Tuson, A., Gandolfi, D., et al. in prep.

Paardekooper, S. J., & Mellema, G. 2006, Astronomy and Astrophysics, 453, 1129, doi: 10.1051/0004-6361:20054449

Palle, E., Orell-Miquel, J., Brady, M., et al. 2023, arXiv e-prints, arXiv:2301.06873, doi: 10.48550/arXiv.2301.06873

Panahi, A., Mazeh, T., Zucker, S., et al. 2022, Astronomy and Astrophysics, 667, A14, doi: 10.1051/0004-6361/202244207

Parmentier, V., Line, M. R., Bean, J. L., et al. 2018, Astronomy and Astrophysics, 617, A110, doi: 10.1051/0004-6361/201833059

Parviainen, H., Tingley, B., Deeg, H. J., et al. 2019, Astronomy and Astrophysics, 630, A89, doi: 10.1051/0004-6361/201935709

Parviainen, H., Palle, E., Zapatero-Osorio, M. R., et al. 2020, Astronomy and Astrophysics, 633, A28, doi: 10.1051/0004-6361/201935958

Pepper, J., Pogge, R. W., DePoy, D., et al. 2007, Publications of the Astronomical Society of the Pacific, 119, 923

Perri, F., & Cameron, A. G. 1974, Icarus, 22, 416

Petrovich, C. 2015, The Astrophysical Journal, 808, 120

Petrovich, C., Tremaine, S., & Rafikov, R. 2014, The Astrophysical Journal, 786, 101

Pfalzner, S., Davies, M. B., Gounelle, M., et al. 2015, Physica Scripta, 90, 068001

Phillips, J. A., & Thorsett, S. E. 1994, Astrophysics and Space Science, 212, 91, doi: 10.1007/BF00984513

Polanski, A. S., & et al. in prep.

Pollacco, D. L., Skillen, I., Cameron, A. C., et al. 2006, Publications of the Astronomical Society of the Pacific, 118, 1407

Pollacco, D. L., Skillen, I., Collier Cameron, A., et al. 2006, Publications of the Astronomical Society of the Pacific, 118, 1407, doi: 10.1086/508556

Pollack, J. B., Hubickyj, O., Bodenheimer, P., et al. 1996, icarus, 124, 62

Pontoppidan, K. M., Pickering, T. E., Laidler, V. G., et al. 2016, in Society of Photo-Optical Instrumentation Engineers (SPIE) Conference Series, Vol. 9910, Observatory Operations: Strategies, Processes, and Systems VI, ed. A. B. Peck, R. L. Seaman, & C. R. Benn, 991016, doi: 10.1117/12.2231768

Prusti, T., De Bruijne, J., Brown, A. G., et al. 2016, Astronomy & astrophysics, 595, A1

Psaridi, A., Bouchy, F., Lendl, M., et al. 2023, Astronomy & Astrophysics, 675, A39, doi: 10.1051/0004-6361/202346406

Quintana, E. V., Gilbert, E. A., Barclay, T., et al. 2023, arXiv e-prints, arXiv:2304.09189, doi: 10.48550/arXiv.2304.09189

Rafikov, R. R. 2005, The Astrophysical Journal Letters, 621, L69

Rafikov, R. R. 2006, The Astrophysical Journal, 648, 666, doi: 10.1086/505695

Rasio, F. A., & Ford, E. B. 1996, Science, 274, 954

Raymond, S. N., Mandell, A. M., & Sigurdsson, S. 2006, Science, 313, 1413

Rein, H., & Liu, S. F. 2012, Astronomy & Astrophysics, 537, A128, doi: 10.1051/0004-6361/201118085

Rein, H., Hernandez, D. M., Tamayo, D., et al. 2019, Monthly Notices of the Royal Astronomical Society, 485, 5490, doi: 10.1093/mnras/stz769

Rescigno, F., & et al. submitted

Rice, M., Wang, S., & Laughlin, G. 2022, The Astrophysical Journal Letters, 926, L17, doi: 10.3847/2041-8213/ac502d

Rice, W., Armitage, P. J., & Hogg, D. 2008, Monthly Notices of the Royal Astronomical Society, 384, 1242

Ricker, G. R. 2015, in AAS/Division for Extreme Solar Systems Abstracts, Vol. 3

Ricker, G. R., Winn, J. N., Vanderspek, R., et al. 2015, Journal of Astronomical Telescopes, Instruments, and Systems, 1, 014003, doi: 10.1117/1.JATIS.1.1.014003

Rickman, E., Ségransan, D., Marmier, M., et al. 2019, Astronomy & Astrophysics, 625, A71

Rieke, G. H., Wright, G., Böker, T., et al. 2015, Publications of the Astronomical Society of the Pacific, 127, 584

Rogers, T. M., Lin, D. N. C., & Lau, H. H. B. 2012, The Astrophysical Journal Letters, 758, L6, doi: 10.1088/2041-8205/758/1/L6

Rosenblatt, F. 1971, Icarus, 14, 71, doi: 10.1016/0019-1035(71)90103-5

Ross, G., Vanderburg, A., de Beurs, Z., et al. submitted

Salvatier, J., Wiecki, T. V., & Fonnesbeck, C. 2016a, PeerJ Computer Science, 2, e55

—. 2016b, PeerJ Computer Science, 2, e55

Schlaufman, K. C., & Winn, J. N. 2016, The Astrophysical Journal, 825, 62

Scott, N. J., Howell, S. B., Gnilka, C. L., et al. 2021, Frontiers in Astronomy and Space Sciences, 8, 138, doi: 10.3389/fspas.2021.716560

Seager, S., & Mallén-Ornelas, G. 2003, The Astrophysical Journal, 585, 1038, doi: 10.1086/346105

Seager, S., & Sasselov, D. D. 1998, The Astrophysical Journal Letters, 502, L157, doi: 10.1086/311498

—. 2000, The Astrophysical Journal, 537, 916, doi: 10.1086/309088

Sebastian, D., Pedersen, P. P., Murray, C. A., et al. 2020, in Society of Photo-Optical Instrumentation Engineers (SPIE) Conference Series, Vol. 11445, Ground-based and Airborne Telescopes VIII, ed. H. K. Marshall, J. Spyromilio, & T. Usuda, 1144521, doi: 10.1117/12.2563563

Shara, M. M., Hurley, J. R., & Mardling, R. A. 2016, The Astrophysical Journal, 816, 59

Showman, A. P., Fortney, J. J., Lian, Y., et al. 2009, The Astrophysical Journal, 699, 564, doi: 10.1088/0004-637X/699/1/564

Silverstein, M. L., Schlieder, J. E., Barclay, T., et al. 2022, The Astronomical Journal, 163, 151

Sing, D. K. 2018, Astrophysics of Exoplanetary Atmospheres: 2nd Advanced School on Exoplanetary Science, 3

Sing, D. K., Fortney, J. J., Nikolov, N., et al. 2016, Nature, 529, 59, doi: 10.1038/nature16068

Siverd, R. J., Brown, T. M., Barnes, S., et al. 2018, in Society of Photo-Optical Instrumentation Engineers (SPIE) Conference Series, Vol. 10702, Ground-based and Airborne Instrumentation for Astronomy VII, ed. C. J. Evans, L. Simard, & H. Takami, 107026C, doi: 10.1117/12.2312800

Skrutskie, M. F., Cutri, R. M., Stiening, R., et al. 2006a, The Astronomical Journal, 131, 1163, doi: 10.1086/498708

—. 2006b, The Astronomical Journal, 131, 1163, doi: 10.1086/498708

Smith, G. R., & Hunten, D. M. 1990, Reviews of Geophysics, 28, 117, doi: 10.1029/RG028i002p00117

Smith, J. C., Stumpe, M. C., Van Cleve, J. E., et al. 2012, Publications of the Astronomical Society of the Pacific, 124, 1000

Stassun, K. G., Collins, K. A., & Gaudi, B. S. 2017, The Astronomical Journal, 153, 136

Stassun, K. G., Corsaro, E., Pepper, J. A., & Gaudi, B. S. 2018, The Astronomical Journal, 155, 22, doi: 10.3847/1538-3881/aa998a

Stassun, K. G., & Torres, G. 2016, The Astronomical Journal, 152, 180

—. 2021, The Astrophysical Journal Letters, 907, L33

Stassun, K. G., Oelkers, R. J., Pepper, J., et al. 2018, The Astronomical Journal, 156, 102

Stassun, K. G., Oelkers, R. J., Paegert, M., et al. 2019a, The Astronomical Journal, 158, 138

—. 2019b, The Astronomical Journal, 158, 138

Steffen, J. H., Ragozzine, D., Fabrycky, D. C., et al. 2012, Proceedings of the National Academy of Sciences, 109, 7982

Stevenson, D. J. 1982, Planetary and Space Science, 30, 755

Stevenson, K. B. 2016, The Astrophysical Journal Letters, 817, L16, doi: 10.3847/2041-8205/817/2/L16

Stevenson, K. B., Harrington, J., Nymeyer, S., et al. 2010, Nature, 464, 1161, doi: 10.1038/nature09013

Stevenson, K. B., Désert, J.-M., Line, M. R., et al. 2014, Science, 346, 838

Stevenson, K. B., Lewis, N. K., Bean, J. L., et al. 2016, Publications of the Astronomical Society of the Pacific, 128, 094401, doi: 10.1088/1538-3873/128/967/094401

Stumpe, M. C., Smith, J. C., Catanzarite, J. H., et al. 2014, Publications of the Astronomical Society of the Pacific, 126, 100

Stumpe, M. C., Smith, J. C., Van Cleve, J. E., et al. 2012, Publications of the Astronomical Society of the Pacific, 124, 985

Sullivan, P. W., Winn, J. N., Berta-Thompson, Z. K., et al. 2015, The Astrophysical Journal, 809, 77

Tanaka, H., Takeuchi, T., & Ward, W. R. 2002, The Astrophysical Journal, 565, 1257, doi: 10.1086/324713

Telting, J. H., Avila, G., Buchhave, L., et al. 2014, Astronomische Nachrichten, 335, 41, doi: 10.1002/asna.201312007

Teyssandier, J., Naoz, S., Lizarraga, I., & Rasio, F. A. 2013, The Astrophysical Journal, 779, 166

Theano Development Team. 2016, arXiv e-prints, abs/1605.02688. http://arxiv.org/abs/1605.02688

Thies, I., Kroupa, P., Goodwin, S. P., Stamatellos, D., & Whitworth, A. P. 2011, Monthly Notices of the Royal Astronomical Society, 417, 1817

Thomas, N., & Paczkowski, M. 2021, Journal of the American Association of Variable Star Observers, 49, 12, doi: 10.48550/arXiv.2012.10720

Thorngren, D. P., & Fortney, J. J. 2018, The Astronomical Journal, 155, 214

Thorsett, S. E., & Phillips, J. A. 1992, The Astrophysical Journal Letters, 387, L69, doi: 10.1086/186307

Timmermans, M., & et al. in prep.

Tokovinin, A. 2018, Publications of the Astronomical Society of the Pacific, 130, 035002

Toomre, A. 1964, The Astrophysical Journal, 139, 1217, doi: 10.1086/147861

Torres, G., Andersen, J., & Giménez, A. 2010, The Astronomy and Astrophysics Review, 18, 67

Torres, G., Fressin, F., Batalha, N. M., et al. 2011, The Astrophysical Journal, 727, 24, doi: 10.1088/0004-637X/727/1/24

Trilling, D., Benz, W., Guillot, T., et al. 1998, The Astrophysical Journal, 500, 428

Trilling, D. E., Lunine, J. I., & Benz, W. 2002, Astronomy & Astrophysics, 394, 241

Tsai, S.-M., Lee, E. K. H., Powell, D., et al. 2023, Nature, 617, 483, doi: 10.1038/s41586-023-05902-2

Twicken, J. D., Catanzarite, J. H., Clarke, B. D., et al. 2018a, Publications of the Astronomical Society of the Pacific, 130, 064502, doi: 10.1088/1538-3873/aab694

—. 2018b, Publications of the Astronomical Society of the Pacific, 130, 064502, doi: 10.1088/1538-3873/aab694

Udalski, A., Zebrun, K., Szymanski, M., et al. 2002a, Acta Astronomica, 52, 115, doi: 10.48550/arXiv.astro-ph/0207133

Udalski, A., Paczynski, B., Zebrun, K., et al. 2002b, Acta Astronomica, 52, 1, doi: 10.48550/arXiv.astro-ph/0202320

Valsecchi, F., Rasio, F. A., & Steffen, J. H. 2014, The Astrophysical Journal Letters, 793, L3, doi: 10.1088/2041-8205/793/1/L3

Van Der Walt, S., Colbert, S. C., & Varoquaux, G. 2011, Computing in science & engineering, 13, 22

Vanderspek, R., Doty, J., Fausnaugh, M., & Villasenor, J. 2018, TESS Instrument Handbook, Cambridge, MA: MIT) https://archive. stsci. edu/files/live/sites/mast/files ...

Vidal-Madjar, A., Désert, J. M., Lecavelier des Etangs, A., et al. 2004, The Astrophysical Journal Letters, 604, L69, doi: 10.1086/383347

Wang, J., Fischer, D. A., Horch, E. P., & Huang, X. 2015, The Astrophysical Journal, 799, 229

Wang, S., Winn, J. N., Addison, B. C., et al. 2021, The Astronomical Journal, 162, 50, doi: 10.3847/1538-3881/ac0626

Ward, W. R. 1997, Icarus, 126, 261

Weidenschilling, S. J., & Marzari, F. 1996, Nature, 384, 619, doi: 10.1038/384619a0

Welbanks, L., Madhusudhan, N., Allard, N. F., et al. 2019, The Astrophysical Journal Letters, 887, L20, doi: 10.3847/2041-8213/ab5a89

Winn, J. N. 2010, arXiv e-prints, arXiv:1001.2010, doi: 10.48550/arXiv.1001.2010

Winn, J. N., Fabrycky, D., Albrecht, S., & Johnson, J. A. 2010, The Astrophysical Journal Letters, 718, L145

Winn, J. N., & Fabrycky, D. C. 2015, Annual Review of Astronomy and Astrophysics, 53, 409

Wolszczan, A., & Frail, D. A. 1992a, Nature, 355, 145

—. 1992b, Nature, 355, 145

Wordsworth, R., & Kreidberg, L. 2022, Annual Review of Astronomy and Astrophysics, 60, 159, doi: 10.1146/annurev-astro-052920-125632

Wright, E. L., Eisenhardt, P. R., Mainzer, A. K., et al. 2010, The Astronomical Journal, 140, 1868

Wright, J. T. 2018, in Handbook of Exoplanets, ed. H. J. Deeg & J. A. Belmonte, 4, doi: 10.1007/978-3-319-55333-7_4

Wright, J. T., Marcy, G. W., Howard, A. W., et al. 2012, The Astrophysical Journal, 753, 160, doi: 10.1088/0004-637X/753/2/160

Wu, Y., & Lithwick, Y. 2011, The Astrophysical Journal, 735, 109

Wu, Y., & Murray, N. 2003, The Astrophysical Journal, 589, 605

Yee, S. W., Winn, J. N., & Hartman, J. D. 2021, The Astronomical Journal, 162, 240

Yee, S. W., Winn, J. N., Hartman, J. D., et al. 2023, The Astrophysical Journal Supplement Series, 265, 1

Zhu, W., Dai, F., & Masuda, K. 2018, arXiv preprint arXiv:1809.00007

Zhu, W., & Dong, S. 2021, Annual Review of Astronomy and Astrophysics, 59

Ziegler, C., Tokovinin, A., Briceño, C., et al. 2020, The Astronomical Journal, 159, 19, doi: 10.3847/1538-3881/ab55e9